SIMULATION AND MODELING OF COMPRESSIBLE AND INCOMPRESSIBLE TURBULENT CHANNEL FLOWS OVER ROUGH WALLS

By

Mostafa Aghaei Jouybari

A DISSERTATION

Submitted to
Michigan State University
in partial fulfillment of the requirements
for the degree of

Mechanical Engineering – Doctor of Philosophy

2020

ABSTRACT

SIMULATION AND MODELING OF COMPRESSIBLE AND INCOMPRESSIBLE TURBULENT CHANNEL FLOWS OVER ROUGH WALLS

By

Mostafa Aghaei Jouybari

The effects of surface roughness on wall-bounded turbulent flows are important for fundamental turbulence research, and turbulence modeling and control, in both compressible and incompressible regimes. This dissertation studies these effects through statistical and structural analysis of turbulence, and provides practical insights for modeling of turbulence in the presence of roughness for incompressible flows. It also proposes an immersed boundary method to simulate compressible flows over rough walls with complex geometries, and studies the roughness effects on supersonic flows over wavy walls.

Turbulence statistics in open channel flows over a smooth wall and three types of wall roughness: sand-grain, cube roughness and a realistic, multi-scale turbine-blade roughness, are examined using direct numerical simulations. Transport of the mean momentum, normal components of the Reynolds stress tensor, and normal components of the dispersive stress tensor are analyzed. The results show higher turbulence isotropy for the rough walls compared to the smooth wall. Wake production, the mechanism through which energy is transported from the wake field to the turbulence field (and vice versa), is strongly influenced by the kind of rough wall. For synthetic rough walls, the wake production has relatively large positive values, while it is negative with a smaller magnitude, for the turbine-blade surface. These results indicate a strong dependence of turbulence processes in the near wall regions on the roughness topography.

Turbulent coherent motions in flows over rough walls are also analyzed. Two-point velocity correlations, length scales, inclination angles, and velocity spectra are studied. Results from linear stochastic estimation suggest that, near the wall, the quasi-streamwise vortices observed in smooth-wall flow are present in the large-scale recessed regions of multi-scale roughness, whereas they are replaced by a pair of ‘head-up, head-down’ horseshoe structures in the sandgrain and cube

roughnesses, similar to those observed in the previous studies. The configuration of conditional eddies near the wall suggests that the kinematic behavior of vortices differs for each kind of rough surfaces. Vortices over multiscale roughness are conjectured to obey a growth mechanism similar to those over smooth walls, while around the cube roughness the head-down horse-shoe vortices undergo a solid-body rotation on top of the element on account of the strong shear layer. This shortens the longitudinal extent of the near-wall structures and promotes turbulence production.

Deep Neural Networks (DNN) and Gaussian Process Regression (GPR) are used to propose a high-fidelity prediction of the Nikuradse equivalent sandgrain height, (k_s), which is frequently used in turbulence modeling of flows over rough walls. To provide a good database, 45 widely different surface geometries are generated and simulated at frictional Reynolds number of 1000, which are also accompanied by 15 fully rough experimental data. The designed DNN and GPR models predict k_s with $err_{rms} < 10\%$ and $err_{max} < 30\%$ which is much more accurate than the models suggested in previous studies.

Finally, a new immersed boundary method is proposed to simulate flow over complex geometries in sub- and supersonic regimes. The method uses a level-set field to impose appropriate boundary conditions at the interface of the fluid and solid cells. Different turbulence statistics are then analyzed and compared in supersonic flows over two 2-dimensional and two 3-dimensional surfaces, and the results reveal a strong dependence of the turbulence field on the roughness topographies and the associated shock patterns.

This thesis is dedicated to my parents.

ACKNOWLEDGEMENTS

My sincere gratitude goes to my supervisors, Professor Giles J. Brereton and Professor Junlin Yuan, for their invaluable guidance and advice throughout my PhD program. I truly appreciate their help, kindness and patience.

I thank the members of my PhD committee, Prof. Farhad A. Jaberi and Prof. Michael S. Murillo, for their thoughtful and constructive comments on different parts of the thesis.

I also would like to thank my parents and my sisters for the sacrifices and dedications they have made for me; although I know there is no thank great enough to compensate for their endless love and supports.

TABLE OF CONTENTS

LIST OF TABLES

Table 5.2: Post processing data. $u_{\tau,s} = \sqrt{\tau_{w,s}/\rho_r}$ and $u_{\tau,r} = \sqrt{\tau_{w,r}/\rho_r}$, where $\tau_{w,s} = -\mu_w \frac{d<\overline{u}>}{dy}\big|_{y=2\delta}$ and $\tau_{w,r} = -\int_0^{k_c} \left\langle \overline{F}_{1,ibm} \right\rangle_T dy$. Here $F_{i,ibm} = \rho \frac{\Delta u_i}{\Delta t}$ is the corresponding body force due to IBM (Δu_i is the velocity difference of u_i after and before the IBM correction step). $\left\langle \cdot \right\rangle_T$ is a simple planar averaging operator that includes all the solid and fluid cells. $\mathrm{Re}_\tau = \rho_r u_{\tau,avg} \delta/\mu_w$, $C_f = 2(u_{\tau,avg}/U_r)^2$ and $u^2_{\tau,avg} = \left(u^2_{\tau,s} + u^2_{\tau,r}\right)/2$. 99

LIST OF FIGURES

KEY TO SYMBOLS AND ABBREVIATIONS

DNS	Direct Numerical Simulation
VOF	Volume of fluid
NS	Navier-Stokes
RANS	Reynolds averaged NS equations
DANS	Double averaged NS equations
FANS	Space-filtered ensemble-averaged NS equations
IBM	Immersed boundary method
TKE	Turbulence kinetic energy
WKE	Dispersive (wake) kinetic energy
RMS	Root mean square
ML	Machine Learning
DNN	Deep Neural Network
GPR	Gaussian Process Regression
x, x_1	Streamwise direction
y, x_2	Wall normal direction
z, x_3	Spanwise direction
t	Time
u, u_1	Velocity component in the x direction
v, u_2	Velocity component in the y direction
w, u_3	Velocity component in the z direction
p	Pressure
ρ	Density
P	p/ρ
T (chapter 5)	Temperature
E (chapter 5)	Total energy
f_1 (chapter 5)	Body force in the x direction
F_i (chapter 2)	IBM body force
μ	Dynamic viscosity
ν	Kinematic viscosity

τ_w	Exerted drag force on a wall
C_f	Drag coefficient
u_τ	Frictional velocity
δ	Channel half height
δ_ν	Viscous length scale
Re	Reynolds number
Re_τ	Frictional Reynolds number
Re_b	Bulk Reynolds number
M	Mach number
Pr	Prandtl number
ϵ	TKE dissipation rate
k_s	Roughness equivalent sand grain height
k	TKE
k	Roughness height distribution
d	Displacement height
$R_{u_\alpha u_\beta}$	Two-point velocity correlations
E_{ij}	One-dimensional premultiplied velocity spectra
κ	von Karman constant
κ (chapter 5)	Heat conductivity coefficient
ϕ (chapter 5)	VOF field
ψ (chapter 5)	Level-set field
ω_i	Vorticity components
λ_{ci}	The imaginary part of the complex eigenvalue of the velocity gradient tensor
ΔU^+	Roughness function
$.^+$	Normalization in wall units
$\left\langle \cdot \right\rangle$	Intrinsic area averaging (filtering) operator
$\left\langle \cdot \right\rangle_s$	Superficial area averaging (filtering) operator
$\overline{\cdot}$	Time averaging operator
$\widetilde{\cdot}$ (chapters 2,3,4)	Dispersive fluctuation
$\widetilde{\cdot}$ (chapter 5)	Favre averaging operator
$.'$	Reynolds (time) fluctuation
$.''$ (chapter 5)	Favre fluctuation

CHAPTER 1

INTRODUCTION

Wall bounded turbulent flows are essential to turbulence research due to their frequent occurrences in natural flows and industrial applications. Examples include environmental flows, meteorological and canopy flows, flows around ships, oil tankers and power generating turbines, flows around airfoils and inside jet engines, and internal flows, such as turbulent flows within ducts, channels and pipes.

Wall 'roughness' is an inevitable feature of many of these flows. Canopy and urban flows are inherently associated with roughness due to presence of vegetation or buildings. The wetted areas of ships, propellers and wind/hydro turbine blades can become rough due to surface erosion, cavitation, growth of algae and dust/abrasive air impingement. Figure 1.1 shows the onset of roughness on the leading edge of a wind turbine blade due to surface erosion. For internal flows such as channel and pipe flows, the surface material, age and its finishing are the main causes of roughness [8]. In the petroleum industry, the interaction of pipes metallic surface with corrosive fluids such as oil increases the surface roughness [9]. River flows over granular/sediment beds

Figure 1.1: The onset of roughness on the leading edge of a wind turbine blade due to surface erosion [1].

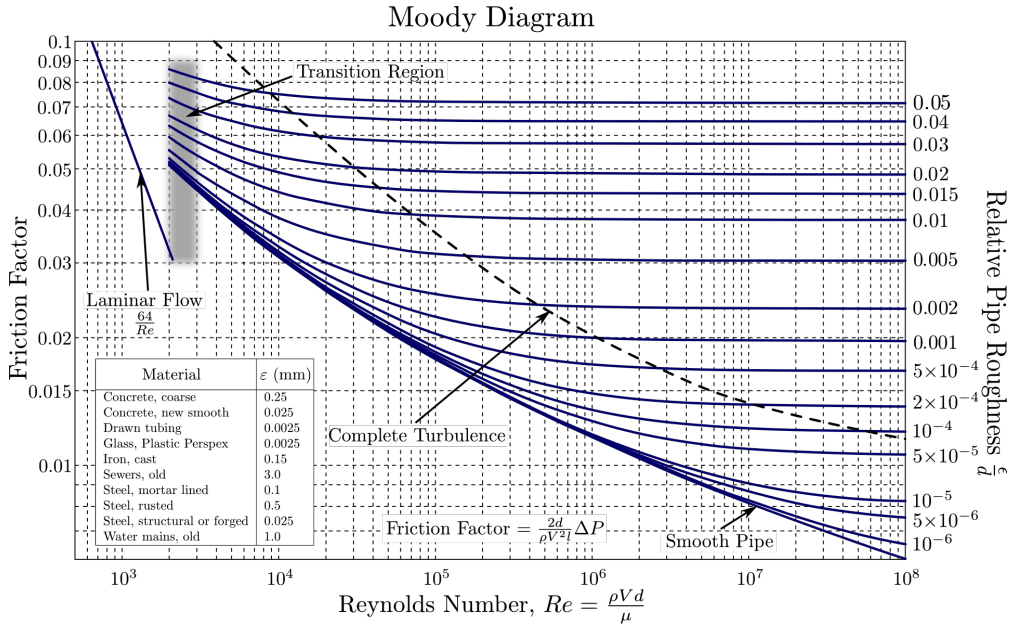

Figure 1.2: Moody diagram [2]. Copyright 1944 ASME.

[10], and plaque build up within arteries [11] are examples of roughness on natural and biomedical flows, respectively.

1.1 Literature review

Roughness effects on wall bounded turbulent flows can be examined from different perspectives, the most important of which are summarized below.

Roughness increases the hydrodynamic drag [12]. The Moody diagram, in figure 1.2, characterizes the hydraulic friction factor in turbulent pipe flows as a function of flow Reynolds number (Re $= Vd/\nu$, where V is the bulk velocity, d is the pipe diameter, $\nu = \mu/\rho$ is the kinematic viscosity, μ is the fluid dynamic viscosity and ρ is the fluid density), and the relative roughness length scale ϵ/d (where ϵ is the roughness length scale). As the figure shows, for sufficiently high Re, the friction factor depends only on the roughness length scale. The extent of which roughness can influence the boundary layer is characterized by the roughness Reynolds number, $k_s^+ = k_s u_\tau/\nu$ (where k_s is the roughness equivalent sandgrain height and u_τ is the frictional velocity). According to the review provided by Jiménez [13], for $k_s^+ \lesssim 4$ the wall can be considered hydraulically smooth. For

this range of k_s^+, viscous effects are dominant and dissipate any roughness effects, therefore, the drag coefficient will depend only on Re. On the other hand, for $k_s^+ \gtrsim 80$ the surface roughness will destroy the viscous sublayer, replacing it with a roughness sublayer. As a result, the wake behind roughness elements and the associated pressure distribution around each element will control the flow behaviour, and the drag coefficient will depend only on k_s^+ (ϵ/d in the Moody diagram). The flow is called fully-rough in this regime. For $4 \lesssim k_s^+ \lesssim 80$ the flow is transitionally rough and the drag coefficient will depend on both Re and k_s^+.

Roughness modifies near wall turbulence structures [14]. These structures are responsible for different physical processes such as mixing and transport of momentum in boundary layers [15]. There are many studies of the effects of roughness on near wall coherent motions [16, 17, 18, 19]. Roughness enhances scalar and momentum transport by modifying these structures [20, 21], and makes the turbulence more isotropic by breaking down the large scale structures to the smaller ones. Understanding the influence of roughness on coherent motions is of particular interest for structure-based turbulence modeling approaches [22, 23], transport of air pollution in urban areas [24], and heat transfer in canopy and rough wall boundary layers [25, 26, 27].

Roughness alters the turbulence response in non-equilibrium flows [28]. Spatially and temporally accelerating flows occur in natural flows and engineering applications. Examples include flow over airfoils and in the atmospheric boundary layer. For smooth wall boundary layer flows, it is well-known that the favorable pressure gradient (as is the case in sink flows) damps turbulence through a mechanism called 'relaminarization' or 'quasi-laminarization' [29, 30]. Roughness, on the other hand, not only destroys this mechanism, but also intensifies the turbulence field through wake production behind the roughness elements, resulting to a 'rougher' surface in favorable-pressure-gradient flows [31, 28].

In the super- and hyper sonic flows, surface roughness can be enhanced by erosion and ablation processes, due to the high amount of heat load in these regimes. The roughness (mostly in a distributed form) interacts with the boundary layer, causes acoustic disturbances and early transition to turbulence, and enhances the heat transfer rate [32, 33]. Most of these effects have been analyzed

experimentally to date, due to difficulties associated with the stability of numerical solvers and with the generation of body-fitted grids in the presence of complex surface roughness.

1.2 Research outline

Understanding the effects of roughness on wall-bounded turbulent flows will expand our knowledge of the physics of these flows, and will help us to improve prediction of their behavior and control them efficiently. This dissertation analyzes these effects, and the following summarizes the most important of them.

Chapter 2 is concerned with turbulence statistics in turbulent flows over rough walls. It includes a comprehensive study on differential and integral forms of the mean momentum equation, and budgets of Reynolds and dispersive stresses. Turbulence statistics are compared for open channel flows over three very different rough walls (as explained briefly below and thoroughly in section 2.2.2) and a smooth wall. The effects of roughness on different terms in the standard k-ϵ model and the elliptic relaxation model of Durbin (k-ϵ-v^2-f, [34]) are also analyzed to provide a good approach for modeling of turbulence in the presence of roughness.

In chapter 3, turbulence structures in fully-developed channel flows over rough walls are analyzed. The main objectives are first to explore how roughness modifies turbulent coherent motions in flows over rough walls, and second, to compare the behavior of these motions in flow over a realistic rough surface with those in flows over synthetic roughnesses. These surfaces are same as those used in chapter 2. The realistic surface is characterized by multiple scales/wavelengths of roughness while the synthetic rough surfaces, made of distributed elements of similar shapes, are described by a single or narrow set of dominant wavelengths. Flows in both the roughness sublayer and the outer layer are examined and two-point velocity correlations, length scales, inclination angles, velocity spectra, vorticities, and helicities are analysed. Linear stochastic estimation is employed to explore the average behavior of the instantaneous vortical motions and their dependence on the roughness topography.

In chapter 4, the roughness equivalent sandgrain height is modeled using Machine Learning

techniques. Nikuradse [35] introduced k_s, to evaluate the roughness function ΔU^+, which represents the hydrodynamic drag in boundary layer flows. His roughness function is $\Delta U^+ = \frac{1}{\kappa} \ln k_s^+ - 3.5$ (where $\kappa = 0.41$ is von Karman's constant and + is normalization in wall units using u_τ and $\delta_\nu = \nu/u_\tau$). The approach uses only a length scale to describe the hydraulic drag associated with the roughness. But, what is this length scale? In her paper, 'moving beyond Moody?', Flack [36] makes it clear that this length scale is not known a priori and non of the geometrical length scales, such as average or root-mean-square (RMS) of roughness height, can describe it uniquely. In fact, it is well-established that k_s depends on many geometrical parameters, such as effective slope [37, 5] and skewness of roughness height distribution [38]. This chapter tries to answer a long standing question about roughness — what is the equivalent sandgrain height, given a roughness topography? To answer this, Machine Learning methods of Deep Learning and Gaussian Process Regression were employed using 45 data points. The data set consists of 30 points from direct numerical simulations and 15 points from experiments, all of which are considered to be fully rough.

In chapter 5, an immersed boundary (IB) method is proposed to enable simulation of supersonic flows over rough walls with complex geometries. To this end, a simulation over a smooth wall (at Mach number of 1.5 and bulk Reynolds number of 3000) is performed first, and its results are validated with the study of Coleman et al. [7]. Second, the IB method is defined and is validated by comparing different mean and turbulence statistics of a supersonic flow over a wavy wall, which, for validation purposes, has been simulated twice: with the IB method and without it (with a conventional body-fitted approach suitable for simple geometries). In the third step, flows over four roughness topographies, two 2-dimensional and two 3-dimensional surfaces, are simulated at a Mach number of 1.5 and a bulk Reynolds number of 3000 using the IB method, and the effects of wall roughness on the mean and turbulence fields, embedded shock patterns, and the Reynolds stress budgets are compared and analyzed.

CHAPTER 2

ROUGHNESS TOPOGRAPHICAL EFFECTS ON MEAN MOMENTUM AND STRESS BUDGETS IN DEVELOPED TURBULENT CHANNEL FLOWS

2.1 Introduction

Turbulence statistics and their connection to the roughness topography are important for understanding physics of turbulence over rough walls, and will pave the way to extend existing turbulence models to capture roughness effects, or to introduce new models capable of predicting turbulence behavior in flows over both smooth and rough walls.

In the presence of roughness, the governing Navier-Stokes (NS) equations are temporally and spatially averaged (in a process called double-averaging) to represent the turbulent flow field statistically. The resulted equations are called double-averaged Navier-Stokes (DANS) equations. The process of obtaining DANS equations are fully explained in the studies of [39, 40, 41], and our new method of deriving these equations is provided in appendix A. There are two main challenges associated with the roughness spatial heterogeneity in derivation of DANS equations. First, one needs to use triple decomposition to separate mean and fluctuation fields. By doing so, along with turbulence field (fluctuations associated with the ensemble-average operator), one identifies the wake field (fluctuations associated with the spatial-average operator) emerges, which is related to the wake region behind the roughness elements. Interactions of the wake field with the both mean and turbulence fields are important for momentum transfer [14] into/out of the roughness sublayer. Second, the spatial-average operator and derivative operator do not 'commute' because of the spatial heterogeneity of the roughness [39, 42]. The use of Leibniz's integral rule in addressing this issue, introduces new form terms in DANS equations, which are the main sources of drag production in flows over roughness, and it is necessary to include their effects in the modeling of turbulence. The details of derivation of DANS equations, triple decomposition and form terms are explained in section 2.2 and appendix A.

2.1.1 Literature review

Several studies focused on the effects of roughness on different turbulence statistics. Raupach and Shaw [39] analyzed budgets of the Reynolds and dispersive stresses to explain the physics of turbulent flows over vegetation canopies. Using empirical data, they showed that wake production (the term that connects turbulence field to the wake field) is of the order of the shear production within the canopies. Mignot et al. [43] analyzed turbulence statistics in channel flows over gravel-beds. They showed that macro-scale roughness elements contribute significantly to turbulence kinetic energy (TKE) production (up to 30%) despite their infrequent occurrence (about 11%). Yuan and Piomelli [44] compared turbulence budgets for sandgrain-type roughnesses in transitionally and fully rough conditions. They showed that the wake field dynamically affects the wall-normal turbulence fluctuation $\overline{v'v'}$ for fully rough surfaces, while its effects are smaller on the transitionally rough surfaces. Busse et al. [45] analyzed the effect of 'surface anisotropy ratio' on the mean and the Reynolds stresses. They have shown that roughness function, ΔU^+, is strongly dependent on this ratio, and spanwise-anisotropic surfaces have much higher ΔU^+ (about 200% increase) compared to the streamwise-anisotropic surfaces. The influence of the wake production in the roughness sublayer for urban flow was analyzed by Giometto et al. [46], where it is shown that the wake production contributes up to 50% to the TKE, and the effect of pressure transport is significant in near wall regions.

Several studies tried to incorporate the effects of roughness in different turbulence models. Suga et al. [47] introduced an analytical wall function to simulate turbulent flows over rough walls and the associated heat transfer. In their wall function, the effects of roughness are accounted for using the Nikuradse equivalent sandgrain height [k_s, 48]. Their numerical results show good agreements with experimental data for both equilibrium and non-equilibrium flows. Lee [49] offered a boundary treatment for the shear-stress-transport k-ω (SST-$k\omega$) model to impart the roughness effects. In this work, the effect of roughness is incorporated using k_s and the treatment is applied to the boundary conditions of TKE and vorticity.

The locally isotropic models, such as the standard k-ϵ model, fail to predict flow behavior

accurately even for smooth walls, due to turbulence inhomogeneity in wall bounded flows. To remedy this issue, several approaches are employed to bring the non-locality effects into turbulence modeling [22, 50] in general, and wall-bounded turbulence modeling [34] in particular. Methods based on elliptic relaxation [34] have shown promising contribution in modeling wall bounded flows, where the non-locality effects are modeled by solving an extra elliptic equation. The equations and different length/time scales in the original elliptic relaxation method of Durbin [34] solves four equations for k (TKE), ϵ (TKE dissipation rate), v^2 (wall-normal Reynolds stress) and f (the elliptic relaxation function). The coefficients of the original model are tuned for the smooth walls. George et al. [51] used experimental rough wall data and found that, for rough wall flows, the maxima of f occurs near the roughness crest, and the peak value decreases as roughness height increases. Using these results, they modified different terms in the f equation and the length and time scales to impart the roughness effects into the modeling.

2.1.2 Objectives

This chapter includes a comprehensive study on differential and integral form of the mean momentum equations, transport of the Reynolds and dispersive stresses and transport of TKE and dispersive (wake) kinetic energy (WKE). The results compare different turbulence statistics for open channel flows over three widely different rough walls (as explained in section 2.2.2) with those of a smooth wall. Roughness sublayer is the crucial region, where roughness effects are more intense, and momentum is transported to/from the inner layer. This region is the focus of the present study, although the turbulence behavior in the outer layer is also analyzed.

The effects of roughness on different terms in the standard k-ϵ model and the elliptic relaxation model of Durbin (k-ϵ-v^2-f) are also examined for a better modeling of turbulence in the presence of roughness.

2.2 Methodology

2.2.1 Governing equations

The NS equations for a constant-property Newtonian fluid, were solved via direct numerical simulation (DNS). These equations are written in indicial notation as

$$\frac{\partial u_i}{\partial x_i} = 0, \tag{2.1a}$$

$$\frac{\partial u_i}{\partial t} + \frac{\partial u_i u_j}{\partial x_j} = -\frac{\partial P}{\partial x_i} + \nu \frac{\partial^2 u_i}{\partial x_j \partial x_j} + F_i, \tag{2.1b}$$

where $i, j = 1, 2, 3$, x_1, x_2 and x_3 (or x, y, z) are the streamwise, wall-normal and spanwise coordinates, with corresponding velocity components of u_1, u_2 and u_3 (or u, v, w) and P is defined as p/ρ, where p is the pressure and ρ is the fluid density; ν is the kinematic viscosity. An immersed boundary (IB) method [52] was used to enforce the fine-grained roughness boundary conditions on a non-conformal Cartesian grid. The corresponding body forces F_i are added to the the right hand side of the momentum equations to impose a no-slip boundary condition at the fluid-roughness interface. To solve the equations, second-order central differencing was used for spatial discretizations and second-order Adams-Bashforth semi-implicit time advancement was employed. The numerical solver was parallelized using the message passing interface (MPI) method [53].

A double-averaging decomposition [39] was used to resolve turbulence and dispersive components of flow variables in the presence of roughness. In this decomposition, any instantaneous flow variable θ may be decomposed into three components, as

$$\theta(\boldsymbol{x}, t) = \left\langle \overline{\theta} \right\rangle (y) + \theta'(\boldsymbol{x}, t) + \widetilde{\theta}(\boldsymbol{x}) \tag{2.2}$$

where the time-averaging operator is $\overline{\theta}$ and the intrinsic spatial-averaging operator is $\left\langle \theta \right\rangle = \frac{1}{A_f} \int_{x,z} \theta dA$ (A_f is the area occupied by the fluid). The Reynolds and dispersive fluctuating components are then $\theta' = \theta - \overline{\theta}$ and $\widetilde{\theta} = \overline{\theta} - \left\langle \overline{\theta} \right\rangle$ respectively. $\langle \overline{\theta} \rangle$ is called the double-averaged component. We also introduce the superficial spatial-averaging operator as $\left\langle \theta \right\rangle_s = \frac{1}{A_t} \int_{x,z} \theta dA$ (A_t is the total planar area), which has implications in some of the results presented here. One simply notices $\left\langle \theta \right\rangle_s = \frac{A_f}{A_t} \left\langle \theta \right\rangle$.

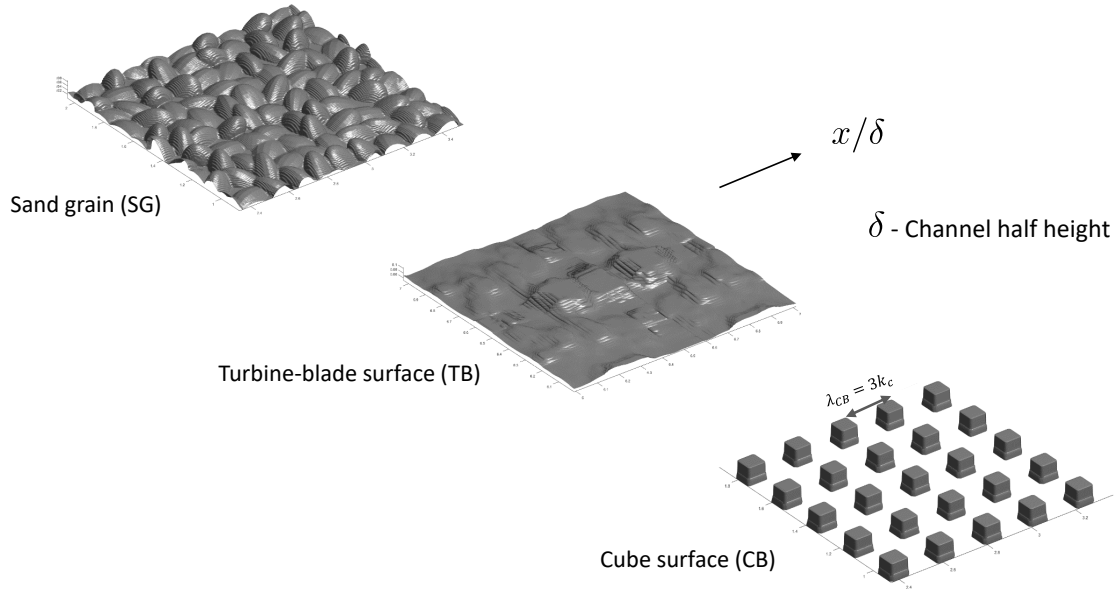

Figure 2.1: Simulated rough surfaces. The figures show a portion of $\delta \times \delta$ in the x-z plane.

The wall shear stress (including both viscous and pressure drag contributions on a rough wall) was determined by integrating the time-averaged F_1 as

$$\tau_w = -\frac{\rho}{L_x L_z} \int_{\mathcal{V}} \overline{F_1}(x, y, z) dx dy dz, \tag{2.3}$$

where $\mathcal{V}$ represents the simulation domain volume below the roughness crest and L_{x_i} is the domain length in the x_i direction. Readers are referred to [52, 44] for details of the implementation and validation of the IB method and the τ_w calculation.

2.2.2 Surface roughness

The three types of wall roughness considered in this study are shown in figure 2.1. For all rough cases, the y origin is set at the lowest trough of the surface. The sand-grain roughness (SG) [54] comprises densely packed, randomly oriented ellipsoidal elements of the same shape, with semi-axis lengths of $(\lambda_1, \lambda_2, \lambda_3) = (1.0, 0.7, 0.5)k_c$, where k_c is the roughness crest height. The turbine blade roughness (TB) is the surface S4 of Yuan and Piomelli [5], mirrored once with respect to both the x and z directions to accommodate periodic boundary conditions. It features surface

Surface	k_c/δ	Ra/δ	k_{rms}/Ra	s_k	k_u	ES_x	ES_z
SG	0.09	0.014	1.05	0.48	2.97	0.43	0.44
TB	0.12	0.014	1.17	0.20	3.49	0.10	0.08
CB	0.07	0.014	0.36	2.45	7.01	-	-

Table 2.1: Geometric parameters of rough surfaces. $\mathrm{Ra} = \left\langle \left| k - \left\langle k \right\rangle \right| \right\rangle$ is the first-order moment of height fluctuations; k_{rms}, root-mean-square of height; s_k, skewness; k_u, kurtosis; ES_{x_i}, effective slope in the x_i direction.

lengthscales in x and z which exceed the channel half-height δ. The cube roughness (CB) was generated by homogeneous duplication of a cube element in the x and z directions with steps of $\lambda_{CB} = 3k_c$ to yield a k-type roughness [55].

Characteristic geometric parameters of these three rough surfaces are displayed in table 2.1. Each surface has the same first-order moment of height fluctuation $\mathrm{Ra} = 0.014\delta$, a crest height of roughly 0.1δ, and a positively skewed height distribution ($s_k > 0$). The effective surface slopes ES_{x_i} [56] are defined as

$$\mathrm{ES}_{x_i} = \frac{1}{L_x L_z} \int_{L_x, L_z} \left| \frac{\partial k(x,z)}{\partial x_i} \right| dz dx, \tag{2.4}$$

where $k(x,z)$ is the local height of the surface, and differs appreciably for these three surfaces. The value of ES_{x_i} for TB roughness is half of that for SG roughness. The ES values for the CB roughness are not compared due to their being locally infinite.

The probability density functions (PDFs) of the local surface gradients $\partial k/\partial x_i$, for SG and TB roughness, are given in Yuan and Aghaei Jouybari [57], where it is shown that gradients steeper than 14° in inclination to the horizontal plane occur more frequently in SG roughness than in TB roughness. The CB roughness has the steepest local surface gradients. Streamwise and spanwise power spectra of these surface height variations are shown in figure 2.2. They feature spikes at $\kappa_r = 2\pi/\lambda_{CB}$ for CB roughness, distinct peaks at $\kappa_r = 2\pi/\lambda_1$ for SG roughness, and an extended region with a slope of roughly -2 for TB roughness. We therefore characterize the CB, SG and TB topographies as spiky, narrow bandwidth and fractal [58] surfaces respectively, in terms of their spectral features, other than physical ones.

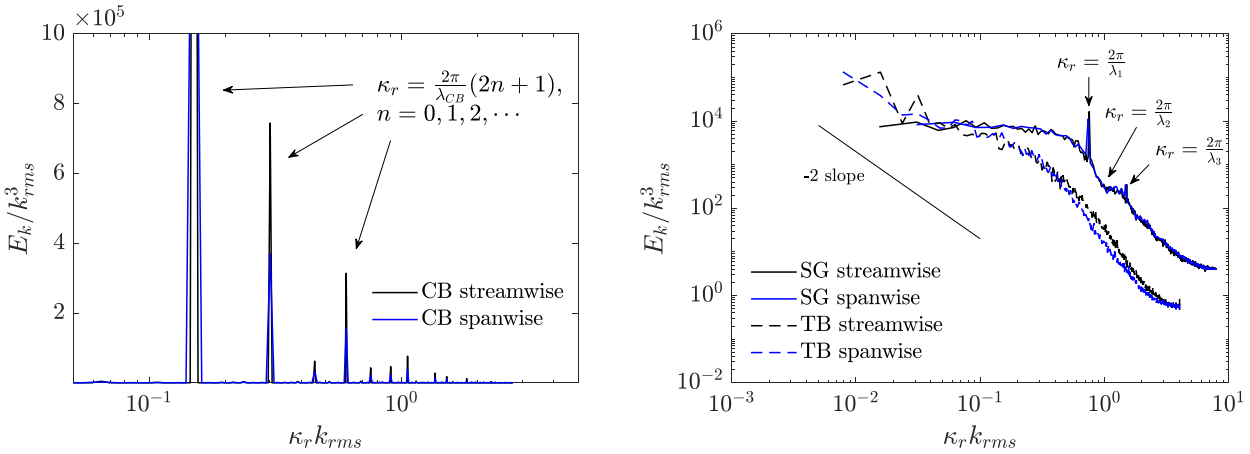

Figure 2.2: Surface height power spectra for CB (*left*), SG and TB (*right*) roughnesses.

	Re_b	k_s^+	y_R/δ	d/δ	$(L_x, L_z)/\delta$	(n_i, n_j, n_k)	$(\Delta x^+, \Delta y^+_{min}, \Delta z^+)$	$C_d \times 10^3$
SM	20000				(6, 3)	(512, 256, 512)	(11.7, 0.3, 5.8)	2.5
SG	11200	78	0.12	0.044	(6, 3)	(1024, 236, 512)	(6.0, 0.7, 6.0)	8.0
TB	14400	24	0.14	0.058	(13, 13)	(1024, 259, 1024)	(13.0, 0.8, 13.0)	4.8
CB	10900	96	0.10	0.039	(6, 3)	(1024, 373, 512)	(6.0, 0.8, 6.0)	8.4

Table 2.2: Simulation parameters. Superscript + indicates normalization in wall units, $\delta_\nu = \nu/u_\tau$, friction velocity $u_\tau = \sqrt{\tau_w/\rho}$, $L_y = \delta$, zero-plane displacement height is d, drag coefficient $C_d = (u_\tau/U_b)^2$, $\mathrm{Re}_b = U_b\delta/\nu$ and the bulk velocity is U_b. $\mathrm{Re}_\tau = u_\tau\delta/\nu = 1000$ in all simulations.

2.2.3 Simulation parameters

The parameters used in these simulations are shown in table 2.2. All simulations were carried out at frictional Reynolds number ($\mathrm{Re}_\tau = u_\tau\delta/\nu$) of $\mathrm{Re}_\tau = 1000$ using n_i, n_j and n_k grid points in streamwise (x), wall-normal (y) and spanwise (z) directions, with corresponding domain sizes of L_x, L_y and L_z. The choice of the same value of Re_τ for all simulations provided a good basis for comparison between rough- and smooth-wall flows at a moderate Reynolds number. All rough cases are in the fully-rough regime according to their respective roughness Reynolds number k_s^+ (to be quantified later, + denotes normalization in wall units using u_τ and $\delta_\nu = \nu/u_\tau$), and based on the findings of Yuan and Piomelli [5] for SG and TB roughness, and the k-type roughness study of Bandyopadhyay [59, fully rough when $k_s^+ > 50$] for CB roughness. This indicates that the

near-wall mean-flow patterns are fully developed, not modified by a further increase of k_s^+. As such, the difference in turbulent structures identified in this study is considered predominantly a result of the difference in roughness geometry, other than the difference in k_s^+. The grid points were distributed uniformly in the streamwise and spanwise directions. In the wall-normal direction, they were spaced uniformly for $y < k_c$ but stretched for $y > k_c$ with larger grid sizes farther from the wall. For all simulations, the grid sizes $(\Delta x, \Delta y, \Delta z)/\eta$, where η is the Kolmogorov length scale (see figure 3.4b), were less than 11 in the x and z directions and much smaller in the wall-normal direction. Based on the observation of Moser and Moin [60], scales smaller than 15η contributed predominantly to turbulence dissipation. Therefore the grid resolutions used in the current study are small enough to resolve the dissipative scales. In these half-channel simulations, periodic boundary conditions were imposed in the x and z directions, and symmetry and no-slip boundary conditions were applied at the top and bottom boundaries respectively. After the initial transient of the simulation was completed, data were collected for statistical analysis over a simulation time of 10-50 large-eddy turnover times ($T \approx \delta/u_\tau$).

2.2.4 Statistics of mean flow and turbulence

The roughness sublayer height y_R is defined as the entire near-wall layer with non-negligible form-induced velocities. y_R is quantified as the location where $\left\langle \widetilde{u}^2 \right\rangle^{0.5}$ first meets $0.06\langle \overline{u} \rangle$, similar to the method proposed by Pokrajac et al. [61]. $y_R \leq 0.15\delta$ for all present simulations.

Mean streamwise velocity profiles, normalized in wall units, are shown in figure 2.3. Each profile has a distinct logarithmic region over the range $30 < (y-d)^+ < 200$, indicating conformity with the law of the wall. It follows that an equivalent sand-grain height k_s can be inferred from the data of figure 2.3 and Nikuradse's correlation (equation 2.5) [48] in the logarithmic region:

$$\left\langle \overline{u} \right\rangle^+ = \frac{1}{\kappa} \ln\left(\frac{y-d}{k_s}\right) + 8.5, \tag{2.5}$$

where d is the displacement height defined as the location where the mean drag appears [62], and $\kappa = 0.41$ is the von Karman constant. In table 2.2, the inferred values of k_s^+ are given as

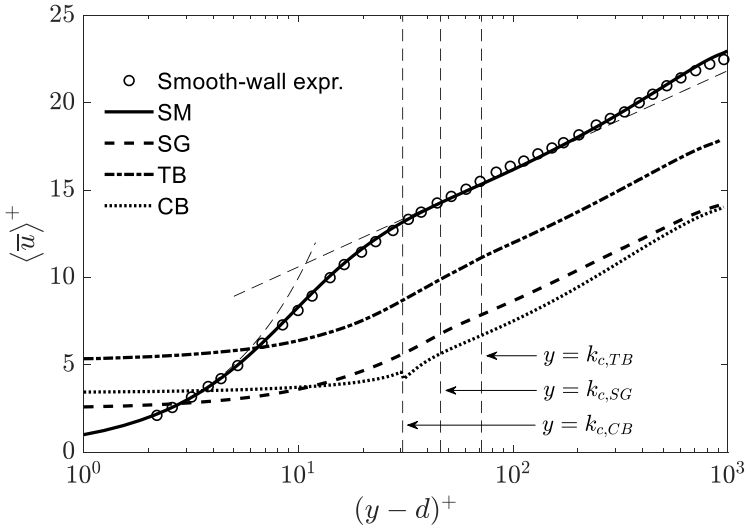

Figure 2.3: Mean streamwise velocity profiles in wall units. Smooth-wall experimental data are from Schultz and Flack [3].

24, 78 and 96 for TB, SG and CB roughness respectively, rendering all rough cases fully rough. The comparison of the drag coefficient C_d given in table 2.2 appears to follow that of k_s^+, with $C_{d,TB} < C_{d,SG} < C_{d,CB}$. This trend may be explained as a result of the very different effective slope values [56], $ES_{TB} < ES_{SG} < ES_{CB}$. It will be shown in the following sections that the effects of roughness on various turbulence structural parameters also follow such relation, with flow characteristics in the TB case generally intermediate between those in the smooth and SG cases, while the effect of CB roughness tend to be more significant than SG and TB roughnesses.

Figure 2.4 shows profiles of the normal and shear components of the Reynolds stress tensor in wall units. Overall, the outer layer similarity is satisfied. In the roughness sublayer, the roughness predictably changes the Reynolds stresses, resulting in a lower anisotropy for rough walls compared to the smooth one. Consequently, the effect of surface topography is greater on the streamwise normal stress than on the other three.

The slight outer-layer mismatch between smooth-wall values of $\langle \overline{u'v'} \rangle^+$ and the values on the rough walls as shown in figure 2.4 (d) is due to non-zero dispersive shear stress, $\langle \widetilde{u}\,\widetilde{v} \rangle^+$ in the outer layer. These non-zero values of $\widetilde{u}$ and $\widetilde{v}$ result from very-large-scale motions with low or high momentum, elongated in the streamwise directions. These motions are thought to

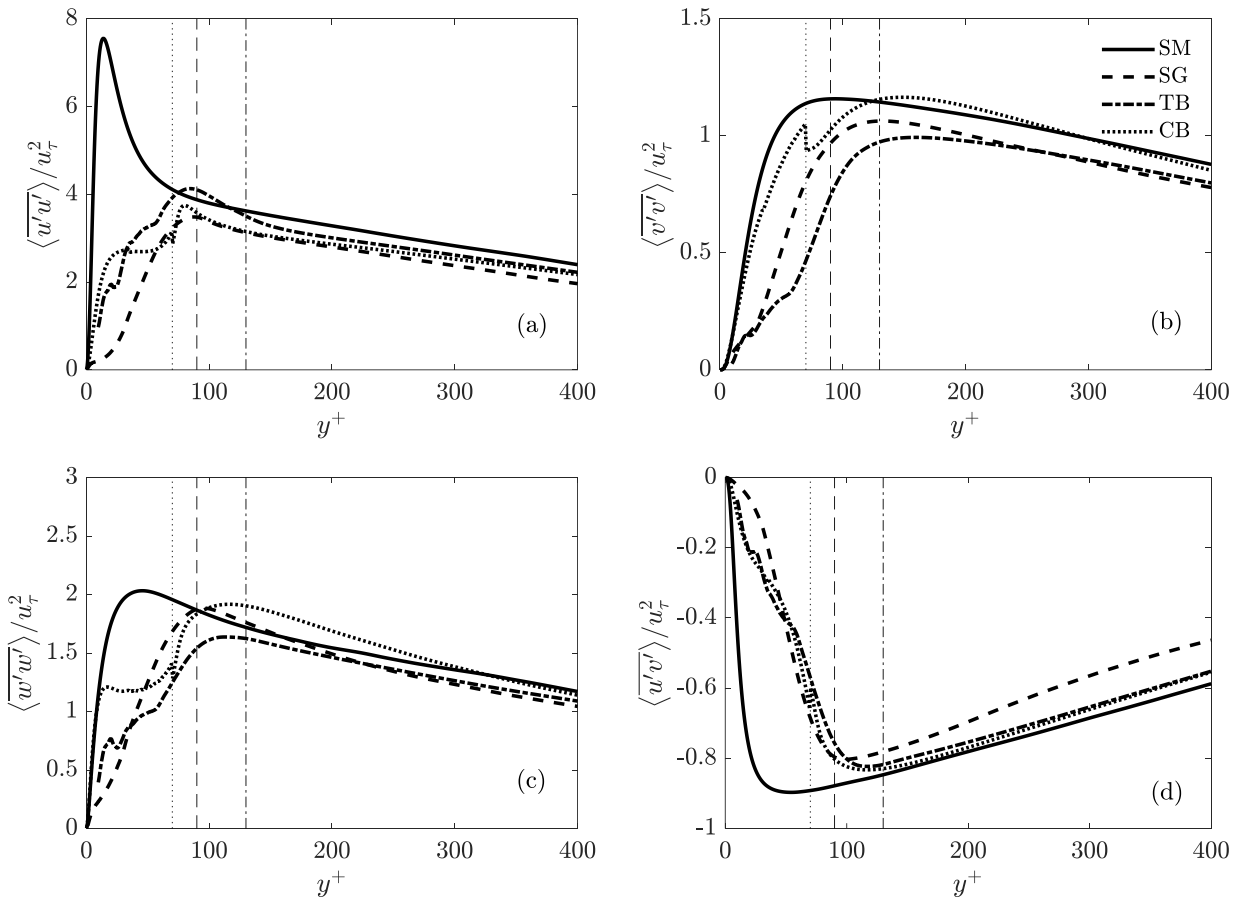

Figure 2.4: Profiles of normal (a,b,d) and shear (d) Reynolds stress tensor components in wall units.

originate from the spanwise heterogeneity of rough surfaces with spanwise wavelengths λ_z which are comparable to δ, same as the surface-induced mean secondary flows first observed for turbine-blade roughness [63, 64] and later systematically studied by Vanderwel and Ganapathisubramani [65] and Yang and Anderson [66], among others, on organized distributed roughness. Consistent with these studies, for the present SG and TB surfaces it is found that the spanwise locations of high surface drag (averaged in x) coincide with the locations of the high-momentum pathways (not shown), even for the SG roughness which is not characterized by a predominant spanwise wavelength of $o(\delta)$. However, the present simulation setup using streamwise periodic channels inevitably leads to 'spanwise locking' [67] of coherent motions with lengths longer than the streamwise domain size (6δ, much shorter than the very-large-scale motions). Consequently, these observed pathways are

influenced, if not significantly modified, by the simulation setup and thus not discussed in depth herein.

2.3 Results

2.3.1 Mean momentum balance

The streamwise DANS equation (see appendix A) reduces to

$$-\frac{d\langle\overline{P}\rangle_s}{dx} - \frac{\partial\langle\overline{u'v'}\rangle_s}{\partial y} - \frac{\partial\langle\widetilde{uv}\rangle_s}{\partial y} + \nu\frac{\partial^2\langle\overline{u}\rangle_s}{\partial y^2} + f_v + f_p = 0, \tag{2.6}$$

where,

$$\begin{aligned} f_v &= -\frac{\nu}{A_t}\oint_{B_{int}} \frac{\partial\overline{u}}{\partial x_j}\boldsymbol{v}_j \cdot \hat{\boldsymbol{n}}\, dl \\ f_p &= \frac{1}{A_t}\oint_{B_{int}} \overline{P}\,\boldsymbol{v}_1 \cdot \hat{\boldsymbol{n}}\, dl. \end{aligned} \tag{2.7}$$

f_p and f_v are the form viscous and pressure drag terms, fully explained in appendix A. Figure 2.5 shows the contribution between different terms in equation 2.6. In the figure, σ shows the residual of the balance, which is approximately zero for all cases. Equation 2.6 and figure 2.5 are important for modeling purposes, especially as far as the peak location of each term and the profiles sharpness/bluntness are concerned. One notices the viscous sublayer in SM is replaced by the roughness sublayer in rough cases and consequently the viscous sink term in SM is substituted by the form drag terms, $f_v + f_p$. The Reynolds stress term is the source term in all cases. Profiles of the Reynolds stress are smoothed out in rough cases compared to the SM, as a result of flow isotropy in the presence of roughness. The peak location is around $y^+ = 15$ for SM and lies in the buffer layer. However, this location scales better with k_c in the rough cases and is about $k_c/2$ for SG and TB, and the very k_c for CB.

In stationary turbulent channel flows, the mean integral of the u-momentum equation reduces to

$$\frac{\tau_{tot}}{\tau_w} = 1 - \frac{y}{\delta}, \tag{2.8}$$

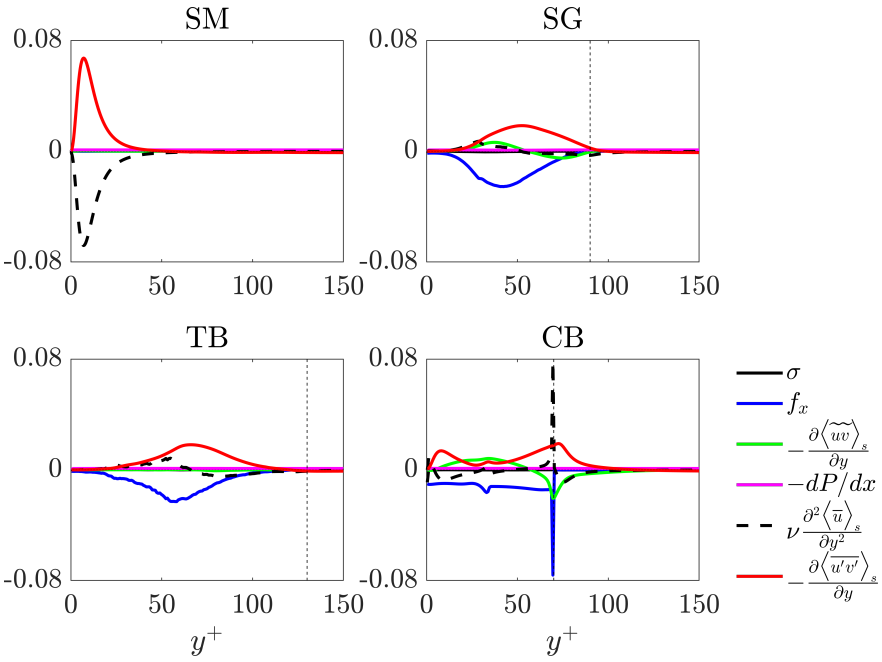

Figure 2.5: Mean momentum equation. The dashed vertical lines are the crest locations.

where

$$\tau_{tot} \equiv \nu\frac{\partial\langle\overline{u}\rangle_s}{\partial y} - \langle\overline{u'v'}\rangle_s - \langle\widetilde{uv}\rangle_s + \underbrace{\int_\delta^y (f_v + f_p)dy}_{\tau_f}. \tag{2.9}$$

This equation shows the balance of different shear stresses. For SM the viscous shear is dominant near the wall ($y^+ < 15$), while far from the wall, the only contributing factor is the Reynolds stress term. For rough walls the form drag term is the dominant term near the wall. The surface porosity is zero at ($y = 0$) for SG and TB case, therefore the form drag equals to 1 at ($y = 0$) for these cases. However, CB has a non-zero porosity (it is partially rough and partially smooth) at ($y = 0$). Therefore, the form drag is less than 1 at the wall for CB. The small viscous drag, resulting from the shear over the smooth parts, compensates the balance of the mean momentum integral equation for CB. The dispersive stress is non-negligible in the roughness sublayer, although it is not the most prominent term at all.

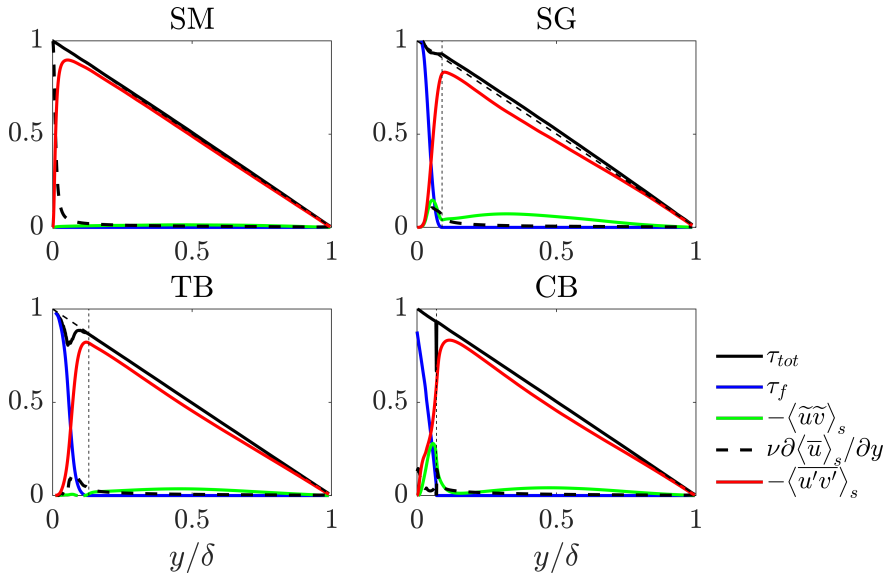

Figure 2.6: Mean momentum integral equation. The dashed vertical lines are the crest locations.

2.3.2 Transport of the normal Reynolds stresses

Transport equations of normal components of the Reynolds stress tensor are derived in the study of [57] as

$$
\begin{aligned}
0 = & \underbrace{-2\langle\overline{u'_\alpha v'}\rangle_s \frac{\partial\langle\overline{u_\alpha}\rangle}{\partial y}}_{P_s} \underbrace{-2\left\langle\widetilde{u'_\alpha u'_j}\frac{\partial\widetilde{u}_\alpha}{\partial x_j}\right\rangle_s}_{P_w} \underbrace{-2\langle\overline{u'_\alpha u'_j}\rangle\left\langle\frac{\partial\widetilde{u}_\alpha}{\partial x_j}\right\rangle_s}_{P_m} \\
& \underbrace{-\left\langle\frac{\partial}{\partial x_j}\widetilde{u'_\alpha u'_\alpha}\widetilde{u}_j\right\rangle_s}_{T_w} \underbrace{-\left\langle\frac{\partial}{\partial x_j}\overline{u'_\alpha u'_\alpha u'_j}\right\rangle_s}_{T_t} \underbrace{+\nu\left\langle\frac{\partial^2\overline{u'_\alpha u'_\alpha}}{\partial x_j\partial x_j}\right\rangle_s}_{T_\nu} \\
& \underbrace{-2\left\langle\overline{u'_\alpha\frac{\partial P'}{\partial x_\alpha}}\right\rangle_s}_{\Pi} \underbrace{-2\nu\left\langle\overline{\frac{\partial u'_\alpha}{\partial x_j}\frac{\partial u'_\alpha}{\partial x_j}}\right\rangle_s}_{\epsilon},
\end{aligned}
\tag{2.10}
$$

where the production terms due to mean shear, wake, and mean wake-shear are P_s, P_w and P_m, respectively. The wake, turbulence and viscous transport terms are denoted as T_w, T_t and T_ν, the pressure work as Π and dissipation as ϵ.

Figure 2.7 depicts different terms in equation 2.10 normalized in wall units. The Reynolds stress budgets for smooth wall have been extensively analyzed in [68]. For this case, in the streamwise

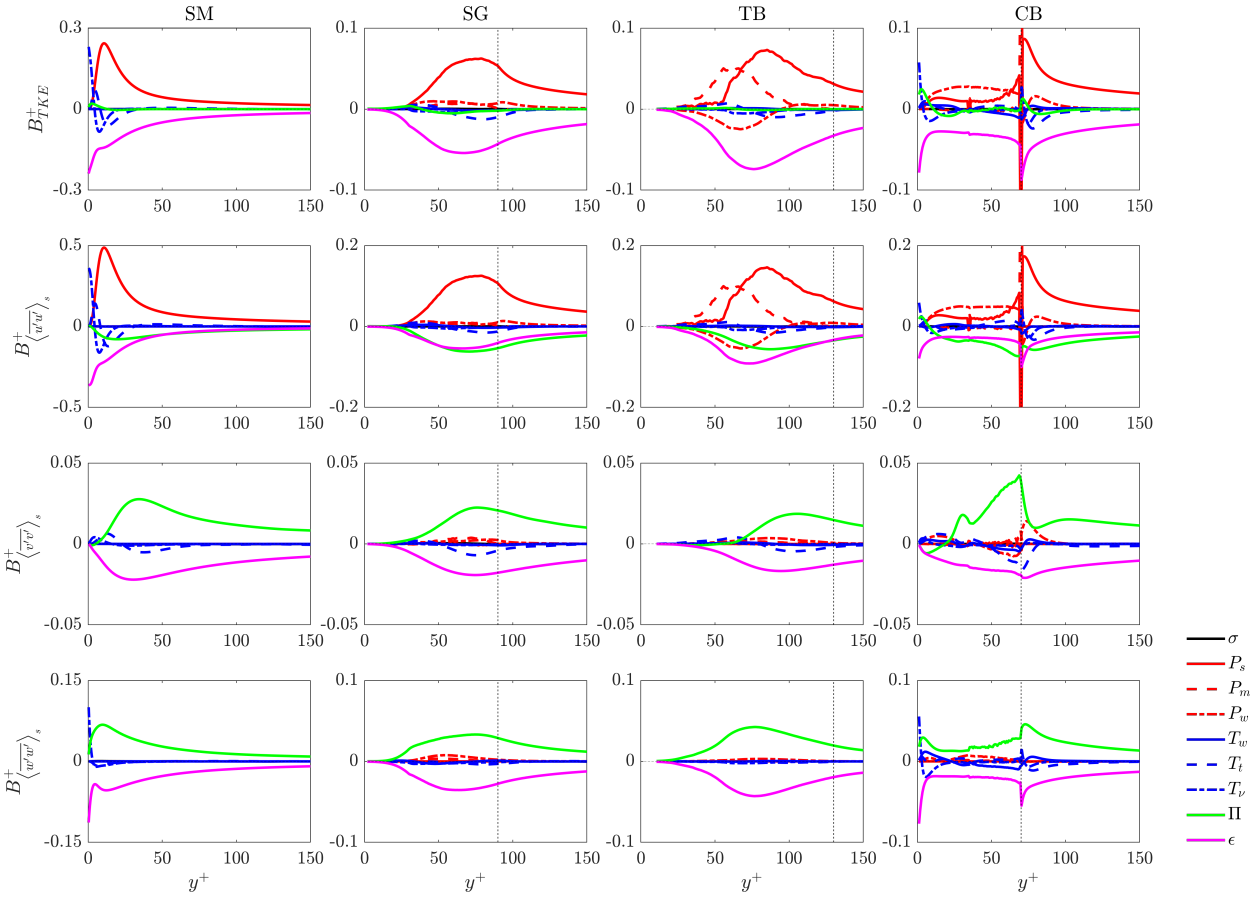

Figure 2.7: Balance of different terms in Reynolds stresses transport equation. The dashed vertical lines are the crest locations.

direction, the shear production is the main source of turbulence production and the energy is redistributed to the wall-normal and spanwise directions through the pressure work, which is the main source of energy in those directions. The same trends apply for the rough walls, except that the roughness-related terms, the wake production P_w and the mean wake-shear P_m, have a substantial influence on the transport balance. The values of P_w in the plot of $B^+_{\overline{<u'u'>_s}}$ are positive for SG and CB, while negative for TB. To understand the physical reason of this trend, the contours of P_w, before applying spatial-averaging operator, are shown in figure 2.8(a,c) for SG and TB and figure 2.9 for CB. In all these figures, the positive values of P_w occur in the wake behind the roughness elements, while the negative values occur in the regions that flow is pseudo-laminarized. One of these regions is immediately upstream of each roughness elements for CB, SG and TB. Another region, noticeable in SG and TB, is in the locations far from the upstream elements (enclosed by

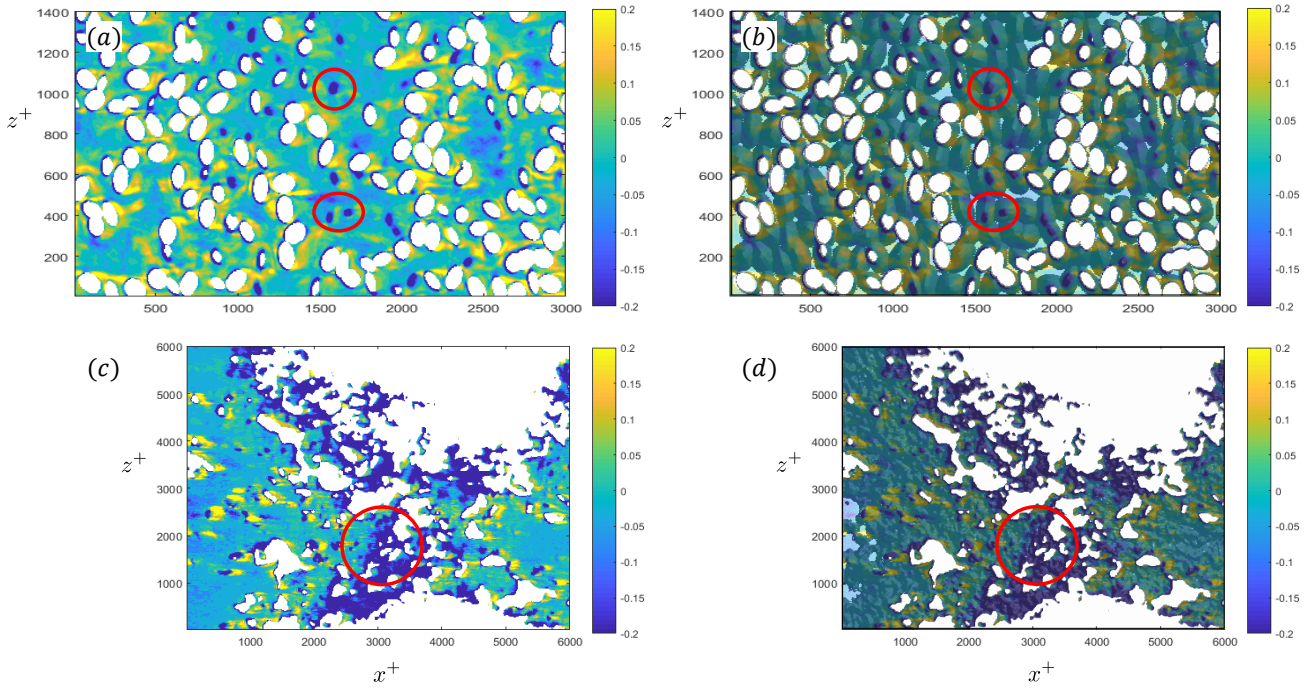

Figure 2.8: Contours of $P^+_{w,uu}$ at $y = d$ for SG (a,b) and TB (c,d). Regular (a,c) and superposed with underlying roughness shape (b,d).

red curves in the figures). To establish a link between roughness and these regions, the underlying roughness topographies for SG and TB have been superposed (with a transparent color) to the contours of P_w in figures 2.8(b, d). As the figures show, those negative regions correspond to the crest location of the underneath roughness elements. Therefore, one can infer that positive values of P_w are mostly due to the large-scale roughness elements, and negative values of P_w are mostly due to the underlying small scale elements.

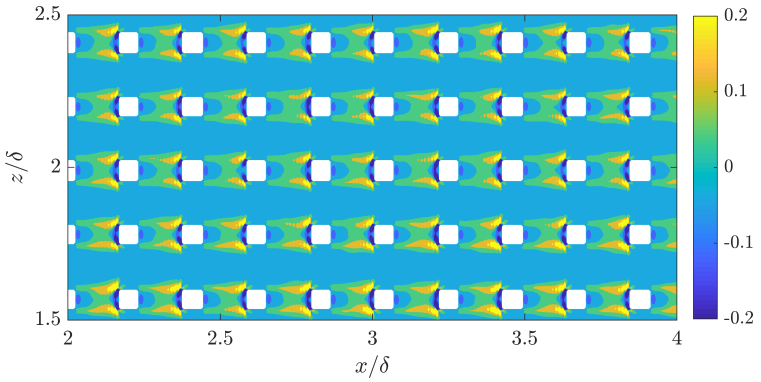

Figure 2.9: Contours of $P^+_{w,tke}$ at $y = d$ for CB.

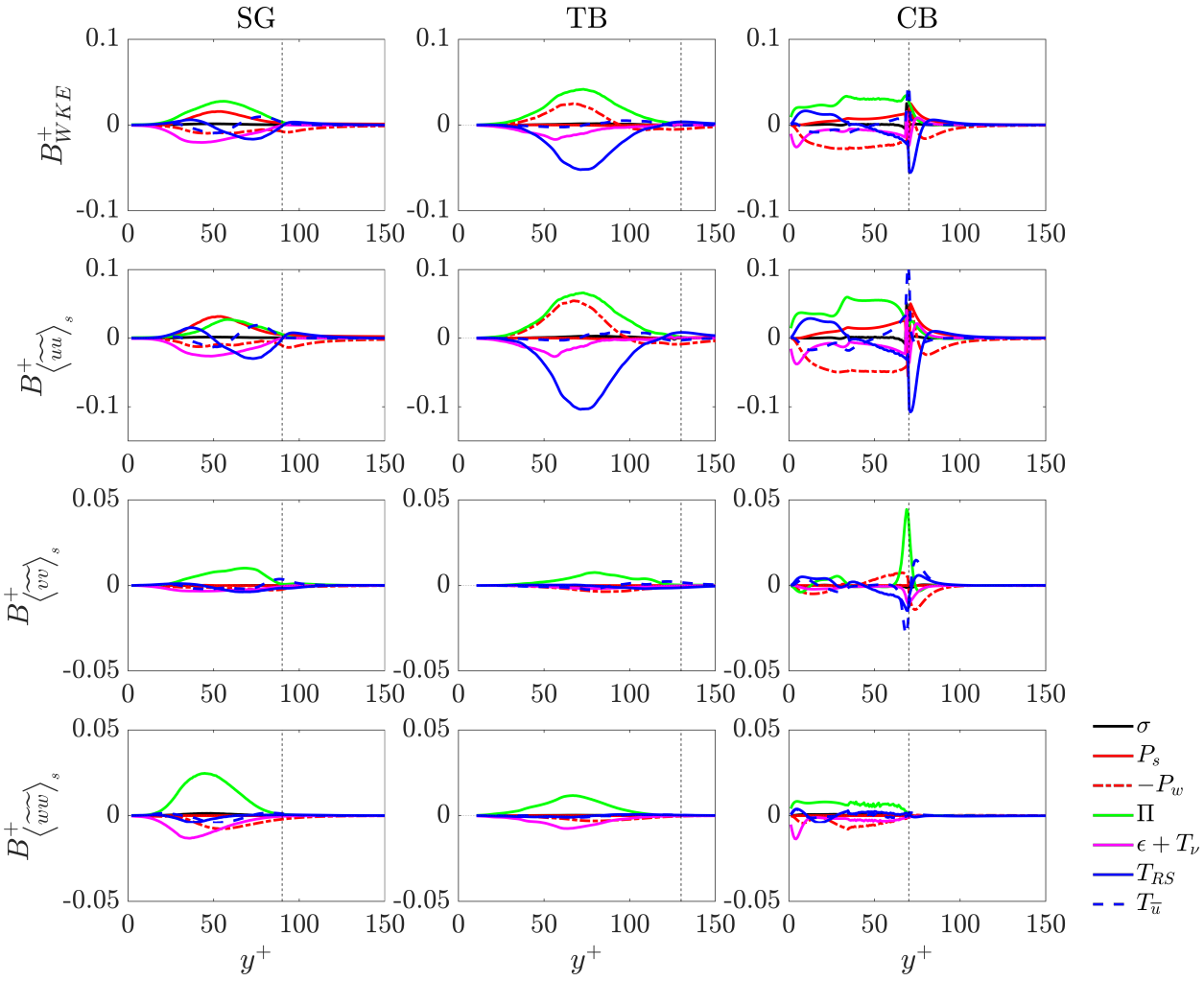

Figure 2.10: Balance of budgets in dispersive stresses transport equation. The dashed vertical lines are the crest locations.

2.3.3 Transport of the normal dispersive stresses

Following [39, 44] the budget of dispersive stresses in normal directions can be written as

$$
\begin{aligned}
0 = & \underbrace{-2\left\langle \widetilde{u}_\alpha \widetilde{u}_j \right\rangle_s \frac{\partial \left\langle \overline{u}_\alpha \right\rangle}{\partial x_j}}_{P_S} + \underbrace{2\left\langle \widetilde{u'_\alpha u'_j} \frac{\partial \widetilde{u}_\alpha}{\partial x_j} \right\rangle_s}_{-P_W} \underbrace{-2\left\langle \frac{\partial}{\partial x_j} \widetilde{u'_\alpha u'_j} \widetilde{u}_\alpha \right\rangle_s}_{T_{RS}} \\
& \underbrace{-\left(\left\langle \overline{u} \right\rangle_j \left\langle \frac{\partial \widetilde{u}_\alpha^2}{\partial x_j} \right\rangle_s + \left\langle \frac{\partial}{\partial x_j} \widetilde{u}_\alpha \widetilde{u}_\alpha \widetilde{u}_j \right\rangle_s \right)}_{T_{\overline{u}}} + \underbrace{\nu \left\langle \frac{\partial^2 \widetilde{u}_\alpha \widetilde{u}_\alpha}{\partial x_j \partial x_j} \right\rangle_s}_{T_\nu} \\
& \underbrace{-2\left\langle \widetilde{u}_\alpha \frac{\partial \widetilde{P}}{\partial x_\alpha} \right\rangle_s}_{\Pi} \underbrace{-2\nu \left\langle \frac{\partial \widetilde{u}_\alpha}{\partial x_j} \frac{\partial \widetilde{u}_\alpha}{\partial x_j} \right\rangle_s}_{\epsilon},
\end{aligned}
\tag{2.11}
$$

where P_s is the shear production, T_{RS} is the transport due to the Reynolds stress, $T_{\overline{u}}$ is the summation of the convective term (almost zero) and the triple wake transport, T_ν is the viscous transport, Π is the work done by the pressure, and ϵ is the dissipation term.

Figure 2.10 shows the contribution of different terms for rough walls. For all cases, the main source term is the pressure work Π and the main sink term is T_{RS}. In the streamwise direction, the magnitude of shear production is large for SG and CB, while it is negligible for TB. The contributing factor in P_s, in streamwise direction, is due to shear dispersive stress $\widetilde{uv}$. Figure 2.11 depicts joint PDF of $\widetilde{u}$ and $\widetilde{v}$ for the rough cases. The $\widetilde{u}$-$\widetilde{v}$ distribution is mostly concentrated near the origin, while for SG and CB it happens mostly in the second and forth quadrants ($\widetilde{uv} < 0$). As a consequence it is expected to have a considerable shear production, $P_s \approx -2\left\langle \widetilde{uv} \right\rangle_s \partial \left\langle \overline{u} \right\rangle / \partial y$, for SG and CB and negligible shear production for TB.

2.3.4 Different parameters in eddy viscosity models

In the simplified Reynolds-averaged-Navier-Stokes (RANS) equations for stationary turbulent channel flows, the shear Reynolds stress is modeled as equation 2.12 in eddy viscosity models,

$$
-\overline{u'v'} = \nu_t \frac{\partial \left\langle \overline{u} \right\rangle}{\partial y},
\tag{2.12}
$$

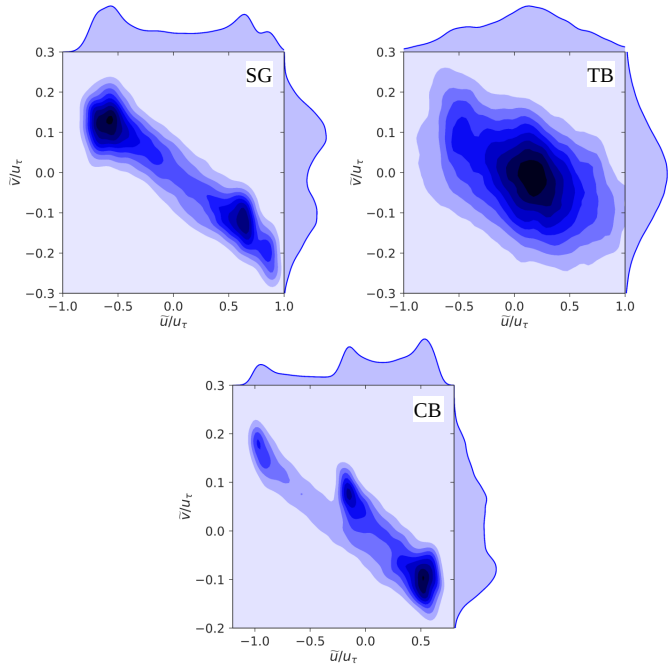

Figure 2.11: Joint PDFs of $(\widetilde{u}, \widetilde{v})$ at $y = d$.

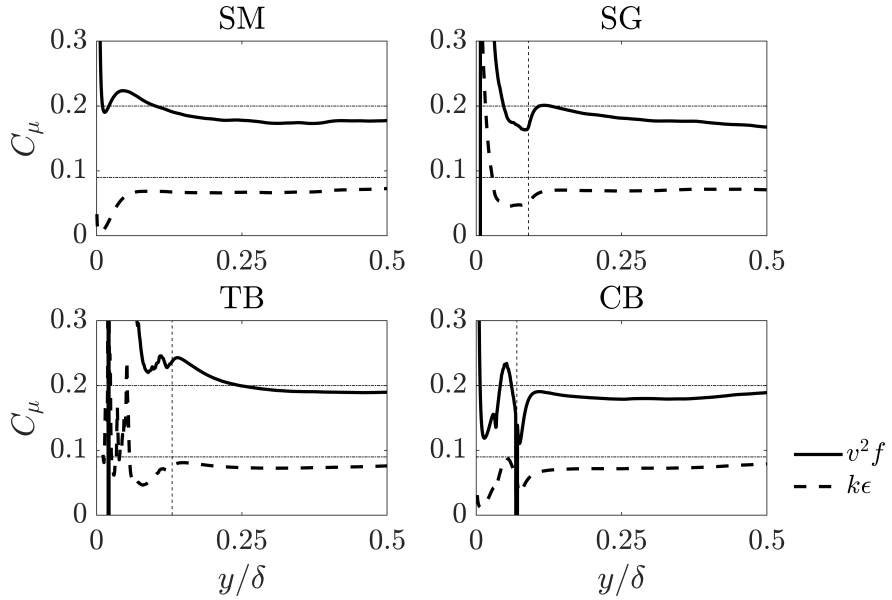

Figure 2.12: Comparison of actual C_μ versus the specified C_μ in k-ϵ and v^2-f models.

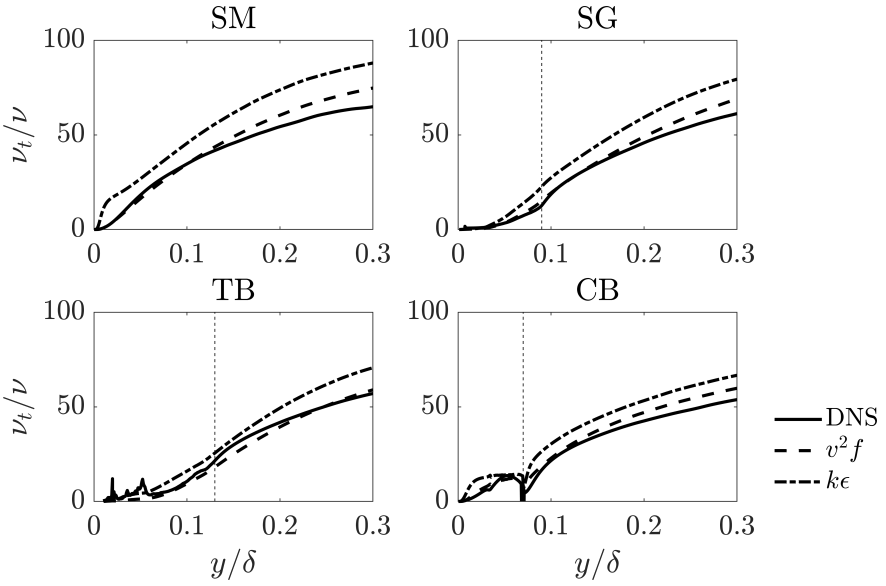

Figure 2.13: Comparison of actual ν_t, versus the modeled ν_t of k-ϵ and v^2-f models.

where ν_t is the dynamic eddy viscosity. Therefore, the closure problem reduces to the modeling of ν_t in an accurate way. Two eddy viscosity models are analyzed here— the classical k-ϵ model, and the elliptic relaxation (k-ϵ-v^2-f, or simply v^2-f) model of Durbin [34].

The dynamic eddy viscosity is modeled as equations (2.13a) and (2.13b) for k-ϵ model and k-ϵ-v^2-f model, respectively.

$$\nu_t = C_{\mu,k-\epsilon}\frac{k^2}{\epsilon}, \tag{2.13a}$$

$$\nu_t = C_{\mu,v^2-f}\frac{k}{\epsilon}v^2, \tag{2.13b}$$

where $C_{\mu,k-\epsilon} = 0.09$ and $C_{\mu,v^2-f} = 0.20$.

Figure 2.12 compares the model coefficient C_μ obtained from DNS data with these pre-specified values. As the figure indicates, the pre-specified values are accurate for most parts of the channel, except for the near the wall regions. This is an important issue, because regions close to the wall are the main source of shear that causes significant turbulence inhomogeneity for wall bounded flows. For smooth walls, it is well-established in the literature that isotropic eddy viscosity models, such as the conventional k-ϵ, are incapable of predicting turbulence behavior for wall-bounded flows because they ignore the non-local effects associated with wall blocking. Many efforts have been

conducted to remedy this problem, either by modifying the standard k-ϵ model, or by devising new models capable of capturing the flow anisotropy.

Figure 2.13 compares the actual dynamic eddy viscosity, obtained from DNS data using $\nu_t = -\overline{u'v'}/(\partial\langle\overline{u}\rangle/\partial y)$, with that of k-ϵ and v^2-f models as specified in equation 2.13. As the figure shows, the k-ϵ model over-predicts the value of ν_t. This was expected given that it assumes an isotropic turbulence.

One can easily rectify these issues by tuning the models coefficients as functions of roughness geometrical properties. This is not the focus of this chapter, but it can be easily done by using regular curve-fitting approaches or by using Machine Learning techniques, similar to the prediction of k_s discussed in chapter 4.

2.4 Concluding remarks

In this chapter, turbulence statistics are analyzed and compared between a smooth wall and three rough walls with different topographies. The simulations are performed for fully developed turbulent channel flows at $Re_\tau = 1000$. The rough walls are two synthetic surfaces of sandgrain and cube-roughness and a realistic turbine blade surface. It is shown that the Reynolds stresses are more isotropic in rough walls compared to the smooth wall. Analysis of the Reynolds stress budgets revealed that the wake and the mean-wake shear productions, P_w and P_m (manifested by surface roughness) play important roles in transferring energy between the wake and the mean flow fields with the turbulence field. P_w is strongly positive for synthetic rough walls, while it is negative for the realistic surface. Correlation between temporal-averaged P_w and surface geometry indicated that the main source of P_w is the wake behind large-scale protuberances, while the main sink of P_w is associated with the near-wall laminarization of turbulence due to small scale roughness elements.

Analysis of the dispersive stresses budgets revealed that the main source of the dispersive stresses is the work done by the pressure, which is also expected because of the strong association between wake behind roughness elements and the pressure variation around each element (which is also the main source of hydraulic drag). It is shown that the wake shear production is also positive

for the synthetic walls, while it is negligible for the realistic surface, due to different distributions of $\widetilde{u}$-$\widetilde{v}$. This distribution is skewed towards Q_2 and Q_4 quadrants for the synthetic walls, while it is centered around zero for the realistic surface.

The results show strong dependence of turbulence statistics to the roughness geometry, especially in the roughness sublayer. These are important for turbulence modeling applications, where the Reynolds stresses and their budgets need to be modeled for accurate predictions of turbulence.

CHAPTER 3

TURBULENCE STRUCTURES OVER REALISTIC AND SYNTHETIC WALL ROUGHNESS IN OPEN CHANNEL FLOW AT $\mathbf{Re}_\tau = 1000$

3.1 Introduction

3.1.1 Literature review

The processes that are essential to sustain turbulence in boundary layers take place close to the wall where the mean shear is high. The turbulent structures responsible for these physical processes [15] have been examined extensively, which has led to improved understanding of turbulence in flows over both smooth and rough surfaces. For smooth walls, this field of study is well established, though it continues to develop in new directions. Some seminal studies in the field include, but are not restricted to, analysis of two point correlations [69], linear stochastic estimation [70], instability analysis [71], mechanisms for generation of coherent packets of hairpins [72], evolutionary behavior of coherent motions [73], and turbulent spot identification [74]. Readers are referred to the monogram by Tardu [75] for a comprehensive review of different methods used to analyze these structures in turbulent flows.

Turbulent structures over rough surfaces have been investigated extensively in previous studies, for a variety of different roughness topographies such as cubical elements [16], turbine blade roughness [76], 2-dimensional (2D) bars [17], pyramids [18] and 2-dimensional (3D) sinusoidal surfaces [19]. For a distributed pyramid roughness, Talapatra and Katz [18] found experimental evidence of interacting U-shaped vortices of the scale of the pyramid in the roughness sublayer. Chan et al. [19] showed that for 3D sinusoidally varying surfaces, the energy contained in larger structures was redistributed to those of the wavelength of the surface, in the vicinity of its crests. Krogstad and Antonia [77] performed experiments on boundary layer flows over k-type rough surfaces: the high sensitivity of values of v'_{rms} and $\overline{u'v'}$ to the wall texture led them to postulate that active motions were strongly dependent on the geometry of the rough wall.

Many rough surfaces found in nature are multiscale or fractal-like [78]. Several recent studies on how multiscale roughness textures affect turbulence have focused on the frictional drag and turbulence statistics within the roughness sublayer. It has been found that the drag scales predominantly on wall-normal turbulence fluctuations at the elevation of the roughness crest [79, 80], and that surface roughness at longer wavelengths does not play a significant role in drag production [81]. For turbine-blade surfaces [5], filtered graphite surfaces [82], and other dissimilar random surface roughnesses [80], it has been shown that the anisotropies of the Reynolds and dispersive stress tensors are texture-dependent. In general, Townsend's similarity hypothesis has been observed to apply to these statistics, provided that the ratio of boundary-layer thickness to roughness height was large and that the Reynolds number is sufficiently high.

For many rough surfaces, only statistical inferences of effects of roughness on the flow have been made, and those studies on turbulence structure focused mostly on particular types of roughness topography, with few studies on multiscale roughness. Relatively little is understood about turbulent structures and coherent motions over different types of rough surfaces, and how their modification by synthetic and realistic wall roughnesses might differ.

3.1.2 Objectives

The present study intends to provide a more comprehensive understanding of turbulence structures in fully-developed channel flows over rough walls. The main objectives are first to explore how roughness modifies turbulent coherent motions in flows over rough walls, and second to compare the behavior of these motions in flow over a realistic rough surface and in flow over a 'standard' roughness. The realistic surface is characterized by multiple scales/wavelengths of roughness while a standard roughness, made up of distributed elements of similar shapes, is described by a single or narrow set of dominant wavelengths. To this end, turbulent flow over a flat surface with the roughness of a production hydraulic turbine blade is simulated and compared with flow over a smooth wall and over two other quite different rough surfaces: sand-grain and cube roughness. The surfaces are same as those used in chapter 2. Flows in both the roughness sublayer and the outer

layer are examined and two-point velocity correlations, length scales, inclination angles, velocity spectra, vorticities, and helicities are analysed. Linear stochastic estimation is employed to explore the average behavior of instantaneous vortical motions in those regions and their dependence on roughness topography.

An understanding of how roughness modifies turbulence structures can also provide important insights into modeling and control of turbulence in both equilibrium and non-equilibrium (accelerating/decelerating) flows over rough walls, though it is recognized that, in non-equilibrium turbulent flows, some effects of roughness can propagate throughout the entire boundary layer, in which case equilibrium wall-similarity scalings may not apply.

The methodology of this chapter is similar to that in chapter 2. Please refer to section 2.2 as for definition of different parameters and mathematical symbols.

3.2 Results

In the following, the characteristics of turbulence structure are discussed using two-point velocity correlation, various length scales, energy spectra, vorticity, and both instantaneous and conditionally-averaged vortical motions.

3.2.1 Two-point velocity correlations

The general form of a two-point correlation of turbulence velocities is defined as

$$R_{u_\alpha u_\beta}(y, r_1, r_2, r_3) \equiv \left\langle \overline{u'_\alpha(x, y, z, t) u'_\beta(x + r_1, y + r_2, z + r_3, t)} \right\rangle. \tag{3.1}$$

The normalized two-point correlations (denoted by subscript n) with a separation in x is

$$R_{u_\alpha u_\beta,n}(y, r_1) = R_{u_\alpha u_\beta}(y, r_1, 0, 0) / R_{u_\alpha u_\beta}(y, 0, 0, 0) \ . \tag{3.2}$$

In figure 3.1, the profile of $R_{uu,n}(y, r_1)$ is shown at different distances from the wall. It can be seen that, close to the wall, $R_{uu,n}$ is most affected by local features of roughness, depicted by the black lines. In an unperturbed turbulent flow field, the magnitude of $R_{u_\alpha u_\beta,n}$ decays smoothly from unity at zero separation, as shown in figure 3.1 for flow over a smooth wall. However, the effect

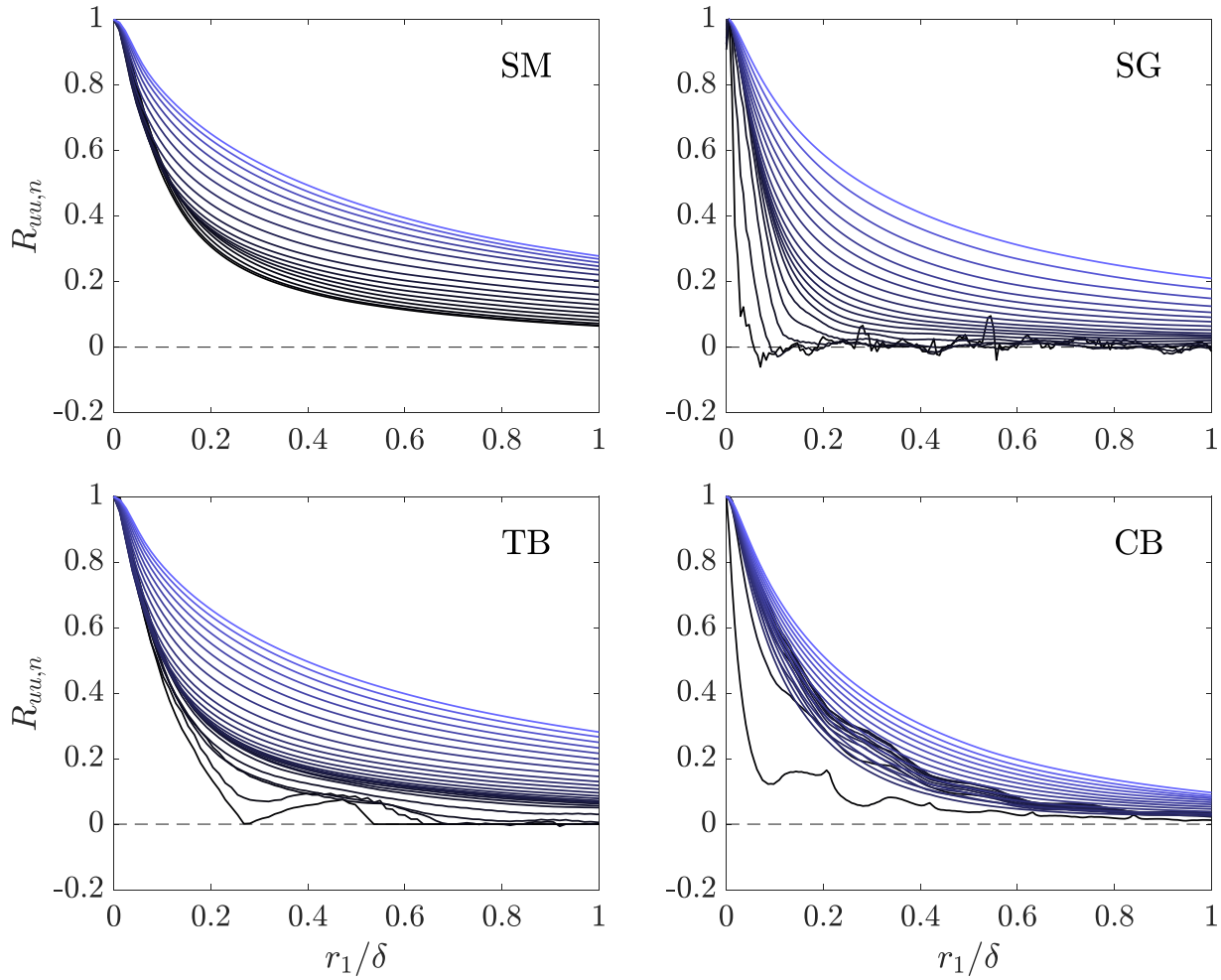

Figure 3.1: Profiles of $R_{uu,n}(y, r_1)$ at y locations from $y \approx 0$ (*black*) to $y/\delta = 0.3$ (*blue*).

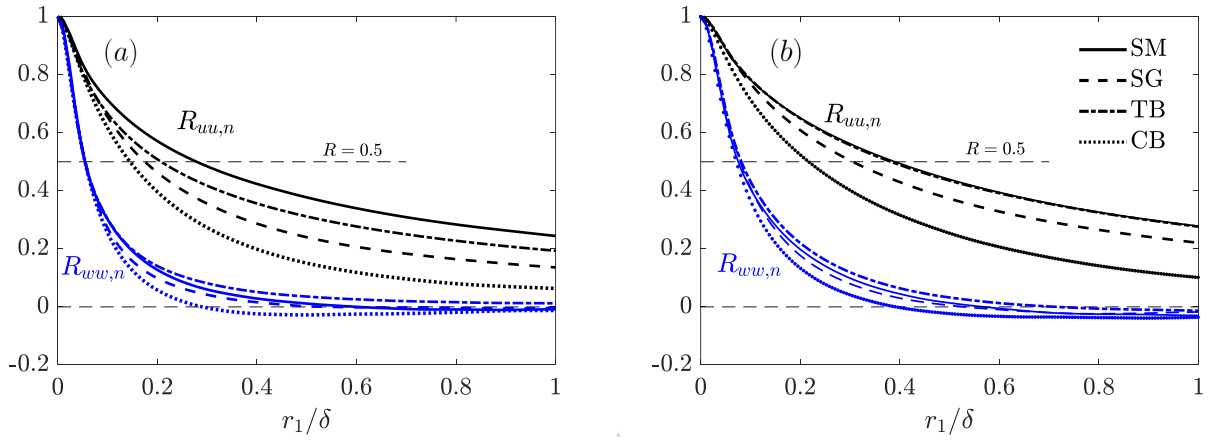

Figure 3.2: Profiles of $R_{uu,n}(r_1)$ (*black*) and $R_{ww,n}(r_1)$ (*blue*), at $y/\delta = 0.15$ (a), at $y/\delta = 0.3$ (b).

of surface roughness can be to either enhance or reduce the value of the correlation at different displacements, due to the periodicity and length scales of roughness.

Near a rough wall, the two-point velocity correlation at a given displacement $\boldsymbol{r}$ can be attributed to: *i*) coherent motions of turbulence of scale $\boldsymbol{r}$; and *ii*) periodic excitation from the surface roughness at wavelength $\boldsymbol{r}$. For example, in the case of CB roughness shown in figure 3.1, near the wall the correlation at displacements shorter than 0.1δ associates predominantly to local streaky motions, while for r_1 of approximately $\lambda_{CB} = 0.21\delta$, the periodic spatial distribution of these streaky motions (smaller than 0.21δ) on account of periodic cube arrangements contribute to the correlation. Pronounced local peaks of R_{uu} with a separation of the wavelength of distributed roughness such as 2D bars was also observed [83]. It will be shown in section 3.2.3 that this effect results in peaks and troughs in velocity spectra measured within the roughness sublayer.

Streamwise and spanwise velocity correlations are plotted in figure 3.2 for two outer-layer locations, $y/\delta = 0.15$ and $y/\delta = 0.3$. In figure 3.2(a), it is shown that $R_{uu,n}$ is still affected by surface roughness at $y/\delta = 0.15$ and in figure 3.2(b), it is shown that $R_{uu,n}$ in flow over the smooth wall and TB roughness collapse at $y/\delta = 0.3$, whereas in flows over walls with SG and CB surfaces they do not—they exhibit a lower degree of correlation over the entire channel. The spanwise velocity correlations $R_{ww,n}$ yield a better overall collapse for the different surfaces than streamwise correlations at both locations. According to the Townsend's outer-layer similarity hypothesis [69], velocity correlations at this location would be expected to collapse when δ/k (where k is the roughness height) is sufficiently large. Jiménez [13] has proposed that Townsend's similarity hypothesis applies when $\delta/k \geq 50$. In the present study, the maximum value of δ/k_c is 14 (for CB roughness), which may explain departures from the hypothesis for the two-point correlation, although it has been shown that wall similarity applies to single-point statistics such as components of the Reynolds stress tensor. It follows that outer-layer structural characteristics of turbulence (such as two-point velocity correlations) appears to be more sensitive to roughness influence than single-point statistics.

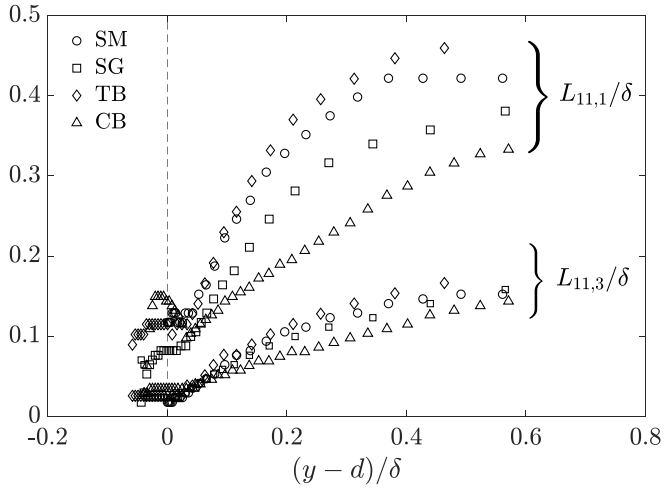

Figure 3.3: Averaged streamwise ($L_{11,1}$) and spanwise ($L_{11,3}$) energy-containing length scales.

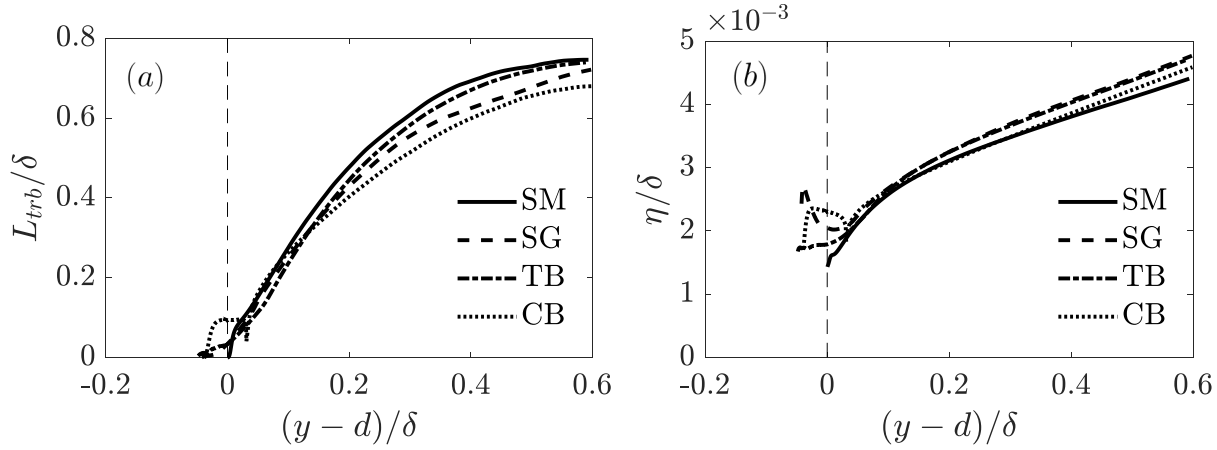

Figure 3.4: Turbulence (a) and Kolmogorov (b) length scales.

3.2.2 Length scales and inclination angles

The size of large-scale energy-containing coherent motions have been previously quantified in various ways: (1) a length scale defined by a cutoff value of $R_{u_i u_j,n}$ [84, 85, 17], (2) integral length scales of $R_{u_i u_j,n}$ [86, 52], (3) the length scales of low-momentum regions of a linear-stochastically-estimated velocity field [87], and (4) the length scales obtained from the spectral coefficients of the correlations [88, 89]. In the present study, two types of length scales are analyzed: (1) the x- and z-extent of the isocontour of $R_{u_i u_j,n} = 0.5$ [85, 17], $L_{ij,k}$ with separation in x_k, as a two-point

structural property, and (2) the turbulence length scale, $L_{trb} \equiv k^{3/2}/\epsilon$, as a single-point statistical property, where k is the turbulence kinetic energy (TKE) and ϵ is the TKE dissipation rate. The choice of $R_{u_i u_j,n}$ cutoff value in $L_{ij,k}$ does not change the overall comparison of $L_{11,1}$, as shown by the shape of $R_{u_i u_j,n}$ profiles in figure 3.2.

These two length scales are plotted in figures 3.3 and 3.4(a), respectively. In both figures, the length scales show linear behavior near the wall ($y^+ < 150$ or $y/\delta < 0.15$), which implies the self-similar growth of the large-scale motions in an average sense. The linear increase of spanwise length scales were also observed by Tomkins and Adrian [87]. Also, it is shown here that L_{11} is smaller above CB and SG surfaces than those above the smooth wall and TB surface. It should be noted that, although L_{trb} (as a direction-free length scale) and $L_{11,3}$ (as a spanwise length scale) appear to conform with the Townsend's outer-layer similarity hypothesis, $L_{11,1}$ and $R_{uu,n}$ (figure 3.2) do not. This suggests that the response of the outer layer flow to wall roughness is directionally sensitive and that the streamwise structure can be influenced strongly by the roughness texture. The experimental study of Krogstad and Antonia [84] on boundary layer flows over smooth and rough walls with $\delta/k \approx 50$ also showed that $L_{11,1}$ (based on a cutoff value of $R_{uu,n} = 0.3$) for rough walls was smaller than $L_{11,1}$ for smooth walls in the outer layer, and $L_{11,3}$ was almost the same in both cases.

The departure from Townsend's similarity in both our results and those of Krogstad and Antonia [84] may be due to limited Reynolds number, as a repeated experiment of turbulent boundary layer flow over a square bar roughness by Krogstad and Efros [90] at a high Reynolds number ($Re_\theta = 32600$ and $\delta/k = 131$) indicated reduced roughness influence on the outer layer.

To compare the size of energy-containing motions mentioned above with the size of the dissipative-scale motions, the Kolmogorov length scale $\eta = (\nu^3/\epsilon)^{1/4}$ is plotted in figure 3.4(b). It can be seen that profiles of η are sensitive to the surface textures only below the roughness crest. For $y > k_c$, all η profiles collapse, indicating that small scale structures become independent of the surface texture even though large-scale structures do not. This observation agrees with the first hypothesis of Kolmogorov [91] that, at scales of the order of η, turbulence obeys a universal

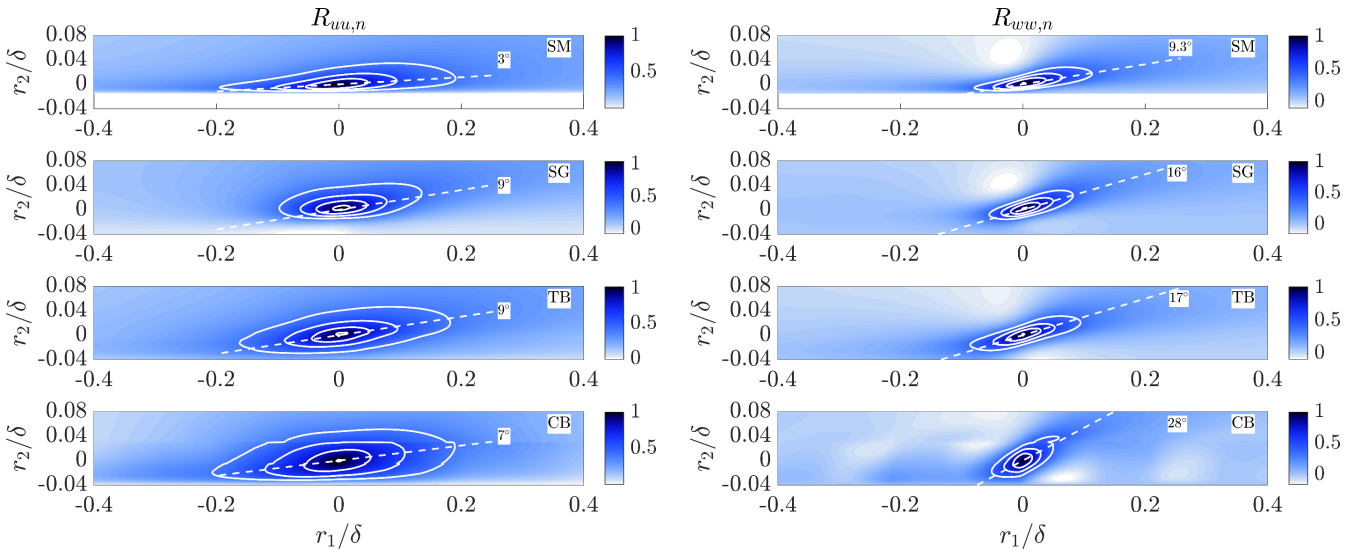

Figure 3.5: Contours of $R_{uu,n}(r_1, r_2)$ (*left*) and $R_{ww,n}(r_1, r_2)$ (*right*) centered at $y = d$ for SG, TB and CB roughness, and at $y^+ = 15$ for the smooth case. The contour level range is [0.4 1.0] with a step size of 0.2.

equilibrium and is locally isotropic.

To quantify the inclination angles of large-scale coherent motions, contours of $R_{uu,n}(y, r_1, r_2)$ and $R_{ww,n}(y, r_1, r_2)$ were plotted in the x-y plane, centered at two types of elevations: (1) a near-wall location in the roughness sublayer ($y = d$) for rough cases and in the buffer layer ($y^+ = 15$) for the smooth case, shown in figure 3.5, and (2) an outer-layer location, at $y/\delta = 0.3$ for all cases, shown in figure 3.6. The characteristic inclination angles were obtained by plotting the best-fitted line (using linear least square method), traversing the farthest points from the origin at contour levels of $\{0.4, 0.6, 0.8\}$. These angles are examined in the context of: *i*) how the angle depends on the particular correlation, for a given surface; and *ii*) how the inclination angle depends on the surface texture.

The figures show that the inclination angles of $R_{uu,n}$ are much smaller than those of $R_{ww,n}$ at both the near-wall and outer-layer elevations. A physical explanation is that w' fluctuations partially originate from ω_x motions, associated with individual vortical motions such as quasi-streamwise vortices, while the u' motions are associated with streaky motions. As a result, the x-extent of u' and w' motions are very different and characterized by different inclination angles.

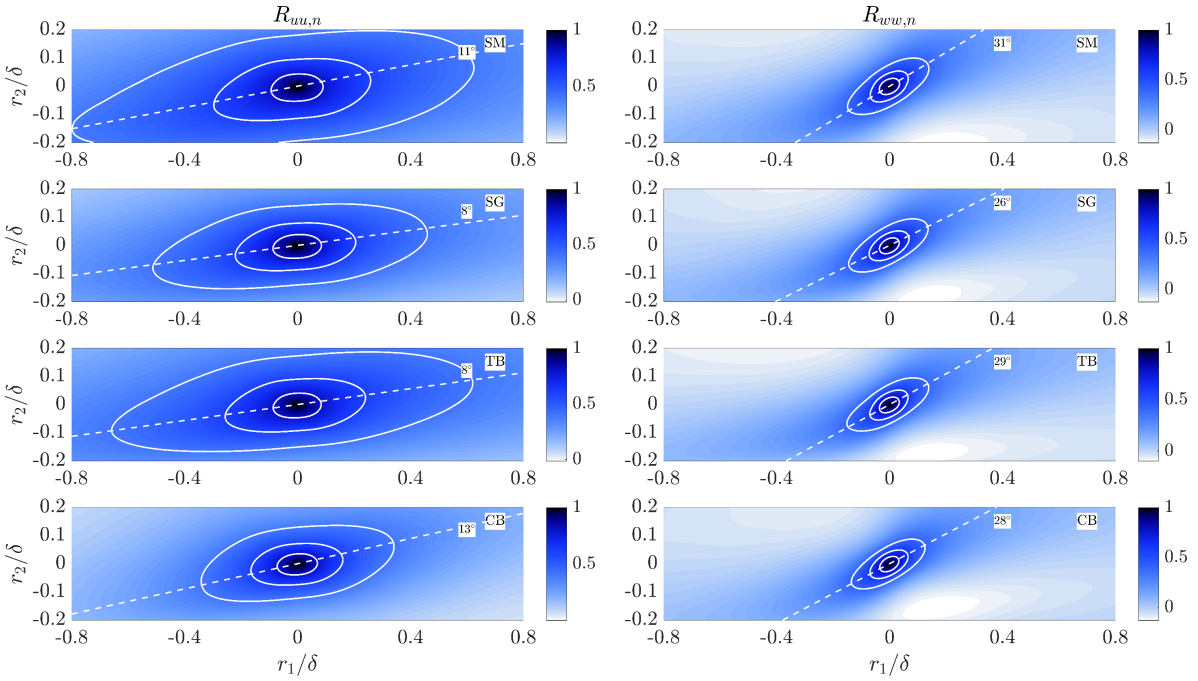

Figure 3.6: Contours of $R_{uu,n}(r_1, r_2)$ (*left*) and $R_{ww,n}(r_1, r_2)$ (*right*) centered at $y/\delta = 0.3$. The contour level range is [0.4 1.0] with a step size of 0.2.

For the near-wall elevations, the angles of inclination depend significantly on the presence of roughness and its texture. These angles are approximately 3° for $R_{uu,n}$ and 9° for $R_{ww,n}$ near the smooth wall and much higher on rough walls, equaling $7° - 9°$ and $16° - 28°$, for $R_{uu,n}$ and $R_{ww,n}$ respectively (figure 3.5). The CB roughness yields an inclination angle of 28° for $R_{ww,n}$. This angle appears to coincide with the angle formed between the cube height and the cube spacing, $\tan^{-1}\{k_c/(\lambda_{CB} - k_c)\} = 26°$; a full explanation of this association cannot yet be provided and may be a topic of future work. Near the wall, Yuan and Piomelli [52] also observed higher inclination angles in the roughness sublayer than in the viscous sublayer, for the SG roughness in sink-flow boundary layers. In the outer layer, all cases show similar inclinations of $8° - 11°$ for $R_{uu,n}$ and 26° - 31° for $R_{ww,n}$ (figure 3.6). The outer-layer values are consistent with those reported by Volino et al. [17], where angles of turbulent structures for boundary layer flows over 3D cubes and 2D bars were also deduced from $R_{uu,n}$ contours. They found that for $0.2 < y/\delta < 0.5$ the inclination angle of $R_{uu,n}$ contour was surface-texture independent and ranged between 10 to 14 degrees. Similar

observations were made by Coceal et al. [16] for channel flow over cubes. These values are largely comparable to the angles found here for very different roughness geometries.

3.2.3 Velocity spectra

One-dimensional velocity spectra are defined as twice the Fourier transform of $R_{u_i u_j}(y, r_1)$, as

$$E_{ij}(y, \kappa_1) \equiv \frac{1}{\pi} \int_{-\infty}^{\infty} R_{u_i u_j}(y, r_1) e^{-i\kappa_1 r_1} dr_1. \tag{3.3}$$

Using (3.3) to calculate E_{ij} is computationally more expensive than the equivalent expression from cross-correlation theory (the Wiener-Khinchin theorem when $i = j$):

$$E_{ij} = 2\mathscr{F}(R_{u_i u_j}) = 2\mathscr{F}^*(u_i') \cdot \mathscr{F}(u_j'), \tag{3.4}$$

where $\mathscr{F}$ is the Fourier transform operator and * indicates the complex conjugate. The right hand side of (3.4) is cheaper to compute as it can be obtained by a Fast Fourier Transform (FFT) algorithm. Equation (3.4) was also used to obtain R_{ij} by taking the inverse Fourier transform of its right hand side [92]. Below the roughness crest, the interpretation of E_{ij} is less clear because fluid domains in the $x - z$ plane may be multiply connected and, as yet, no velocity spectra appear to have been reported where $y < k_c$. The applicability of (3.4) is also questionable because the spatial velocity signals are segmented in this region and their Fourier transform is not guaranteed to exist. Instead, (3.3) is used for power-spectral estimation because $R_{u_i u_j}$ is continuous in this region, notwithstanding its 'conditional' nature discussed in section 3.2.1. In this study, the velocity spectra at all y-locations are obtained using (3.3), with a Hann window function to minimize the Gibbs phenomenon at large wavenumbers [93]. Data within half of the x and z domains are used to calculate the two-point correlations; thus, noises are present in the spectra if no window function is used.

In figure 3.7, the one-dimensional longitudinal velocity spectra E_{11} are plotted at $y/\delta = 0.3$ against wavenumber multiplied by the Kolmogorov scale. It shows a universal behavior consistent

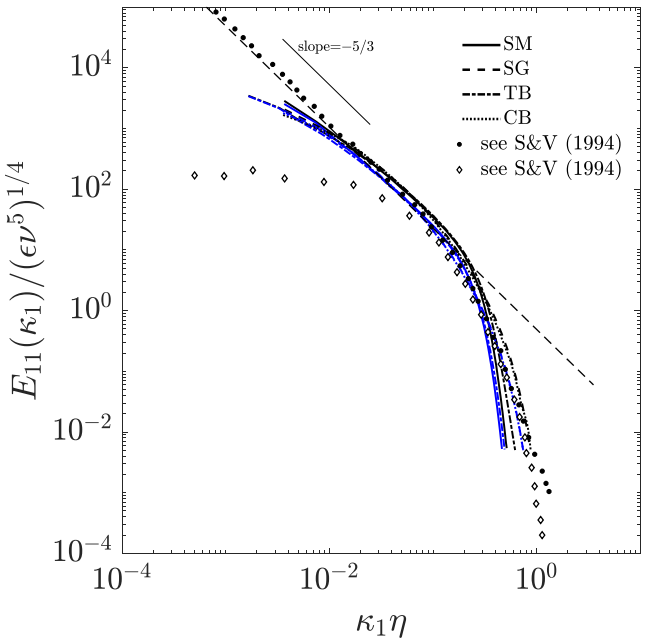

Figure 3.7: One-dimensional longitudinal velocity spectra E_{11} at $y/\delta = 0.3$. Lines in *black* are obtained using (3.3) and lines in *blue* using (3.4). Experimental data are from [4]. Plots in circles and diamonds are for boundary layer flow at $\mathrm{Re}_\lambda = 1500$ and wake flow at $\mathrm{Re}_\lambda = 23$ respectively. The thin dashed line describes $E_{11} = 0.49\kappa_1^{-5/3}\epsilon^{2/3}$.

with an energy cascade from large to small eddies [94]. The energy spectra collapse on a line of slope $-5/3$ and obey universal behavior in the presence of roughness in homogeneous directions, even over the narrow range of wavenumbers obtained in these low (compared to experimental studies) Reynolds number simulations. This observation is consistent with those of Coceal et al. [16] for flow over cubes of uniform size, for which it was noted that pre-multiplied spectra of $\kappa_1 E_{11}$ followed a $-2/3$ decay law. Velocity spectra obtained by Fourier transform (3.4), are also plotted in figure 3.7 for the purposes of comparison. The two methods for calculating energy spectra, using equations (3.3) and (3.4), yield very similar spectra when $y > k_c$ and the velocity signals are continuous.

The premultiplied velocity spectra E_{11}, E_{22}, E_{33}, and E_{12} are plotted in figures 3.8 and 3.9 in the κ_1 and κ_3 directions, respectively. They are compared with the power spectra of surface height fluctuations to explore a possible relation between the length scales of turbulence and those of the

rough surface. Three types of elevations are of particular interest. First, at $y = d$, the rough-case results are compared with those in the smooth case inside the buffer layer at $y^+ = 15$. Secondly, the lower edge of the logarithmic region (around $y = k_c$, see figure 2.3) in the rough cases is compared with $y^+ = 40$ in the smooth case, which is also at the lower edge of the logarithmic region. And thirdly, the outer layer at $y/\delta = 0.3$ is compared among all cases, where the flow is expected to be independent of surface conditions if Townsend's similarity hypothesis applies. In both figures 3.8 and 3.9, it can be seen that at $y = d$ and $y = k_c$ the E_{ij} components are dependent on the kind of surface chosen and, as y increases, they become progressively more independent of the surface condition. For example, at $y/\delta = 0.3$, the location of the energy peaks and the general shapes of E_{ij} are similar for each kind of wall roughness, consistent with Townsend's similarity hypothesis.

As y decreases, the peak of E_{11} moves toward higher wavenumbers in both the κ_1 and κ_3 directions, indicating shrinking of energy-containing scales as the wall is approached. The energy carried by the low-wavenumber u' motions is, in all rough cases at both $y = d$ and $y = k_c$, much less than in the smooth-wall case at the corresponding elevations, because surface roughness breaks down the buffer-layer streaky motions by introducing voritcal structures with high three-dimensionality. In addition, at the near-wall locations, the peak values of E_{ij} components, normalized by u_τ, show higher anisotropies in SM and TB cases, consistent with the Reynolds stress comparison in figure 2.4.

At the near-wall elevation, the connection between the energy spectra and the surface length scales is analyzed for each kind of roughness. For SG roughness, it appears that the peaks of $E_{22}(\kappa_1)$ and $E_s(\kappa_1)$ coincide at the same wavenumber. Similarly, the peak of the $E_{11}(\kappa_3)$ coincides with both that of $E_s(\kappa_3)$, though such wavelength is also where the smooth-wall $E_{11}(\kappa_3)$ peak is located. For TB roughness, the fractal nature of the surface-height distribution does not yield a dominant surface wavenumber; its E_{ij} profiles are similar to those in the smooth case. For CB roughness, the energy spectra are strongly correlated with the surface power spectrum, which has spikes at $\kappa = 2\pi/\lambda_{CB}$ and its multiples. At $y = d$, in figure 3.8 it can be seen that E_{11} and E_{33} have toughs and peaks, respectively, at the same κ_1 values as these spikes. These extrema appear

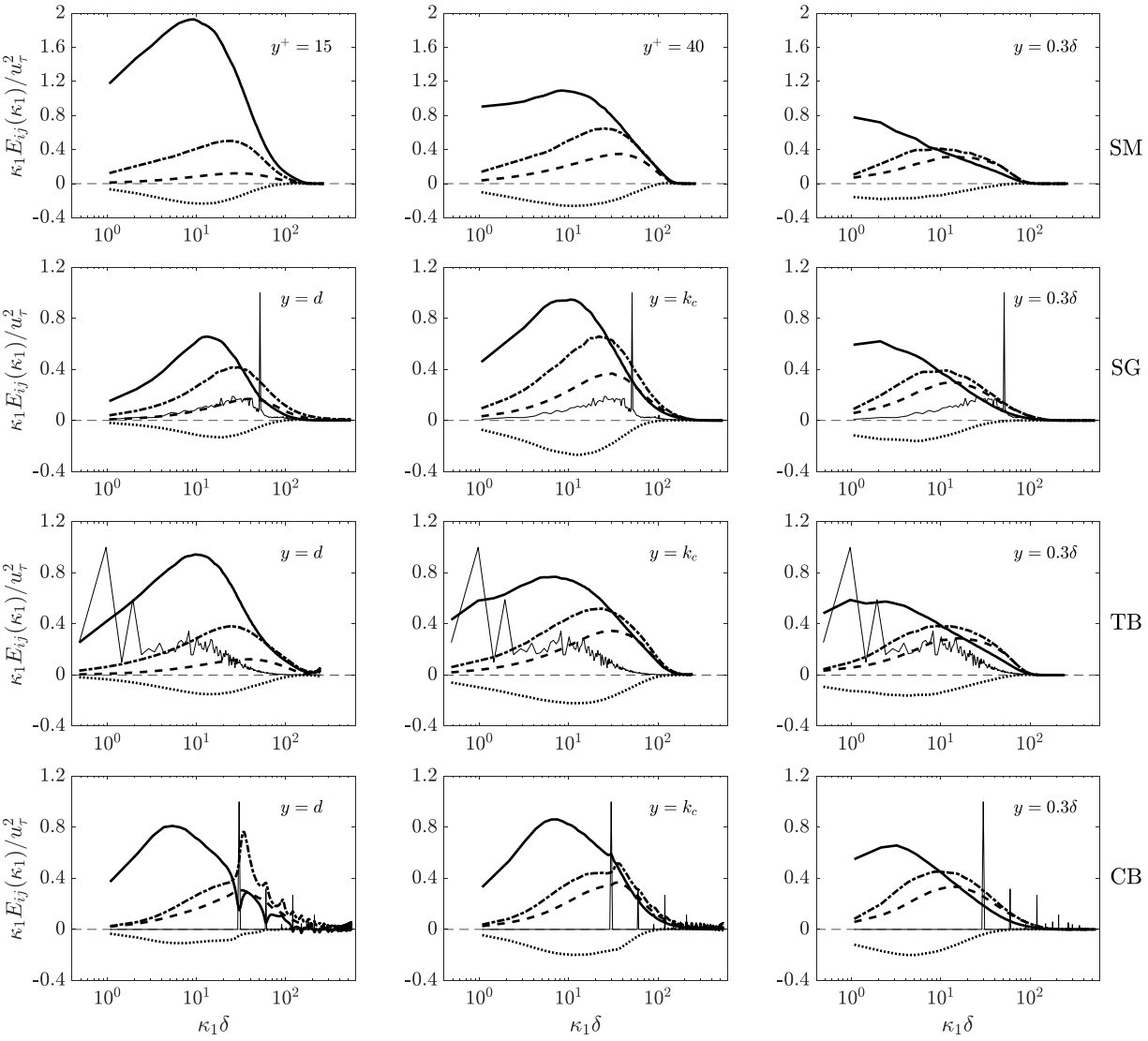

Figure 3.8: One-dimensional longitudinal premultiplied velocity spectra, E_{ij}, and surface-height power spectra, E_s. —— E_{11}; - - - E_{22}; -·- E_{33}; ··· E_{12}; —— (thin) E_s. E_s is normalized to give a maximum value of 1.

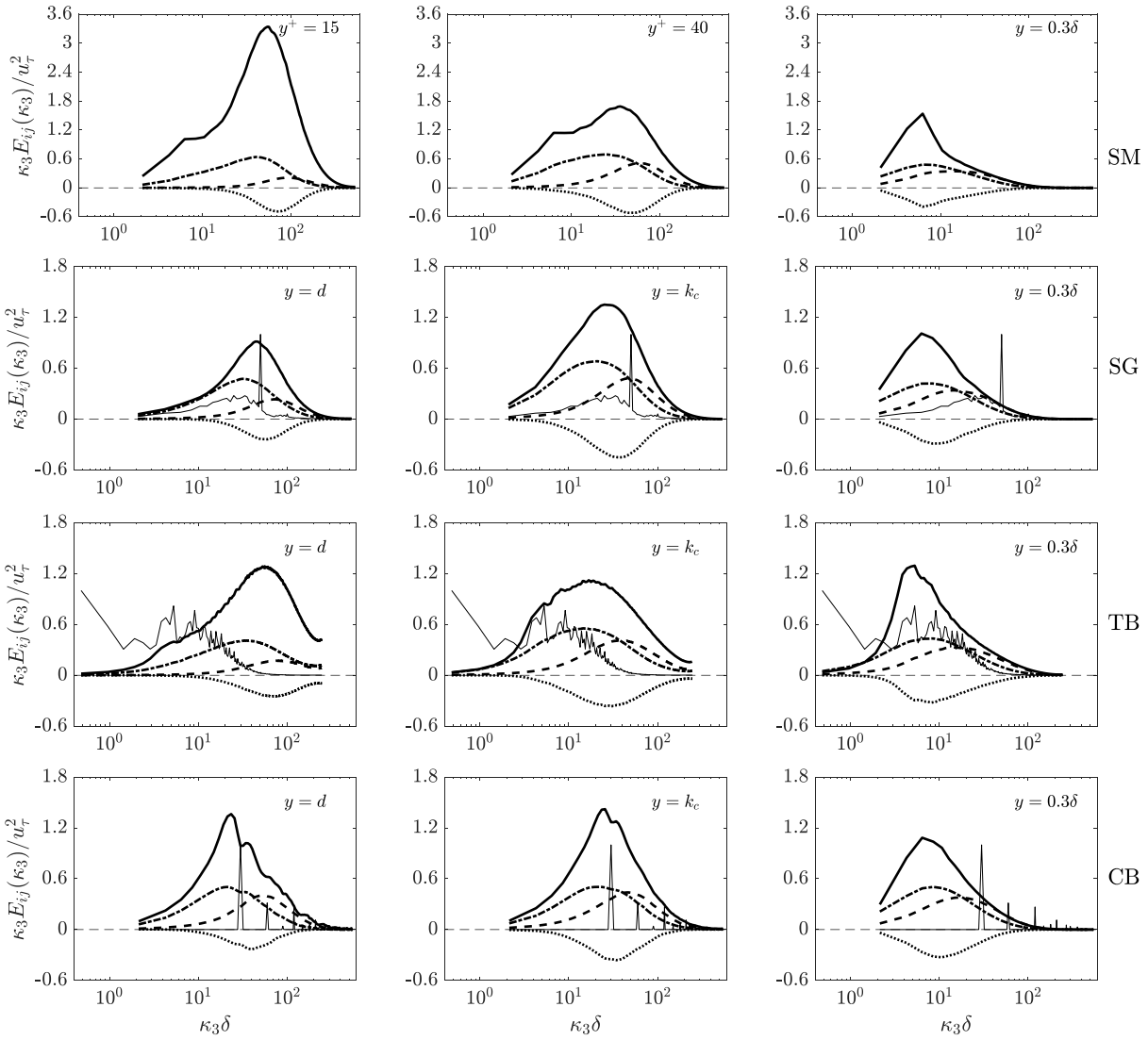

Figure 3.9: One-dimensional transverse premultiplied velocity spectra. —— E_{11}; - - - E_{22}; -·- E_{33}; ··· E_{12}; —— (thin) E_s. E_s is normalized to give a maximum value of 1.

to be a consequence of the surface periodicity described in section 3.2.1.

3.2.4 Vorticity and helicity

The root-mean-square (RMS) values of vorticity fluctuations, normalized in wall units, are plotted in figure 3.10. In the outer layer, irrespective of the surface type, all cases collapse showing the isotropy of the vorticity tensor—a result observed previously for both smooth [95] and rough walls [96]. It is known that, near a smooth wall $\omega'_{3,rms}$ is mostly caused by the intense shear generated

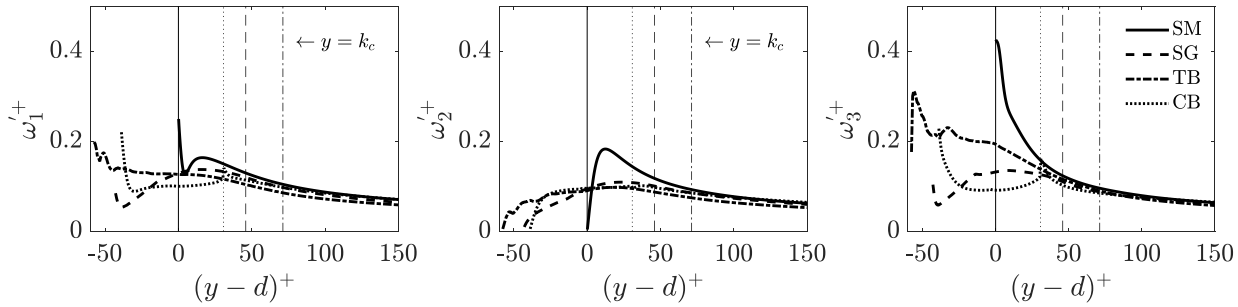

Figure 3.10: Profiles of RMS vorticity in wall units. Thin vertical lines show the corresponding roughness crest elevations.

by u' between the wall and the streaks, $\omega'_{2,rms}$ represents mostly $\partial u'/\partial z$ in the regions between adjacent high and low-speed streaks, and $\omega'_{1,rms}$ displays a local minimum and a local maximum at $y^+ = 5$ and 20 respectively, attributed to the quasi-streamwise vortices. Roughness affects the anisotropy of the vorticity tensor near the wall. The peaks of $\omega'_{2,rms}$ and $\omega'_{3,rms}$ are significantly lower in flow over rough walls compared to smooth ones, implying that roughness modifies the organized motions by breaking down the near-wall streaks and promoting the three-dimensionality of the vortical motions. SG and CB roughnesses have a similar effect on producing significantly more isotropic vorticity fluctuations. In contrast, ω'_i near the TB roughness maintains a high anisotropy similar to the smooth wall. This is because, for TB roughness, low-speed streaks with intense u' are still present below $y = d$ in the recessed roughness region (due to the largest x and z wavelengths of the surface). The behavior of TB roughness is again shown to be intermediate to that of smooth wall and SG roughness.

The joint probability density functions (PDFs) of u'_α and ω'_α, which contribute to the local helicity $u'_\alpha\omega'_\alpha$, are compared in figure 3.11. Data are plotted at $y = d$ for SG, TB and CB roughness and at $y^+ = 15$ for the smooth surface. Three types of turbulent eddies have been defined by Kassinos [97] as: jetal ($u'_\alpha \neq 0$, $\omega'_\alpha \approx 0$); vortical ($u'_\alpha \approx 0$, $\omega'_\alpha \neq 0$); and helical ($u'_\alpha \neq 0$, $\omega'_\alpha \neq 0$). The joint PDF for the flow over the smooth wall is skewed towards jetal motions with $u' < 0$ and $\omega'_1 \approx 0$, which is the characteristic of the low-speed streaks. Roughness, irrespective of its texture, reduces the significance of these motions and makes the joint PDF contours more concentric. In

the case of CB roughness, a slight tendency exists towards positive values of u', which may suggest slightly more pronounced sweeping events at $y \approx d$. The joint PDFs of v' and ω_2' shows that, at $y^+ = 15$ on the smooth wall, the v' motions are predominantly associated with jetal sweeps ($v' < 0$, $\omega_2' \approx 0$), inactive motions originated from above, and helical ejection motions ($v' > 0$, $\omega_2' \neq 0$), representing the counter-rotating pairs of quasi-streamwise vortices. Near rough walls, in contrast, all types of motions are roughly equally possible, indicating highly three-dimensional shape of coherent motions. The joint PDFs of w' and ω_3' show a symmetric behavior for all cases, on account of the symmetry due to the boundary conditions in this direction. Joint PDFs were also obtained in the outer layer at $y/\delta = 0.3$ and were all very similar (not shown), consistent with Townsend's similarity hypothesis.

3.2.5 Instantaneous vortical motions and conditional eddies

Instantaneous coherent motions are visualized using iso-surfaces of swirl strength, quantified by the imaginary part of the complex eigenvalue of the velocity gradient tensor λ_{ci} [72]. The results are shown in figure 3.12 for $y/\delta < 0.25$, in which it can be seen that inclined quasi-streamwise vortices exist in the vicinity of both smooth and rough walls, with higher inclination angles (in the x-y plane) and tilt angles (in the x-z plane), as well as more irregular shape for SG and CB roughnesses. Large number of spanwise-aligned vortex segments are also visible on the rough surfaces. On SG and CB surfaces, two arch-shape vortical structures are highlighted, which may be examples of the solid-body rotation of an originally head-down horse-shoe vortex on account of strong local shear layer, to be discussed in Section 3.2.6.

Linear stochastic estimation (LSE) [70] was used to compare the vortex shape over both the smooth wall [72, 98] and rough ones [18, 99]. The LSE is an average velocity field (the *conditional eddies*), conditioned on given events at specified locations in the flow domain; the procedure is fully described by Adrian [100]. Following Talapatra and Katz [18], we use an event based on the vortex-identification parameter, here $\lambda_{ci} > 0$. The event is a scalar. There are two advantages for this approach— first, the conditional eddy obtained herein is composed of all possible physical

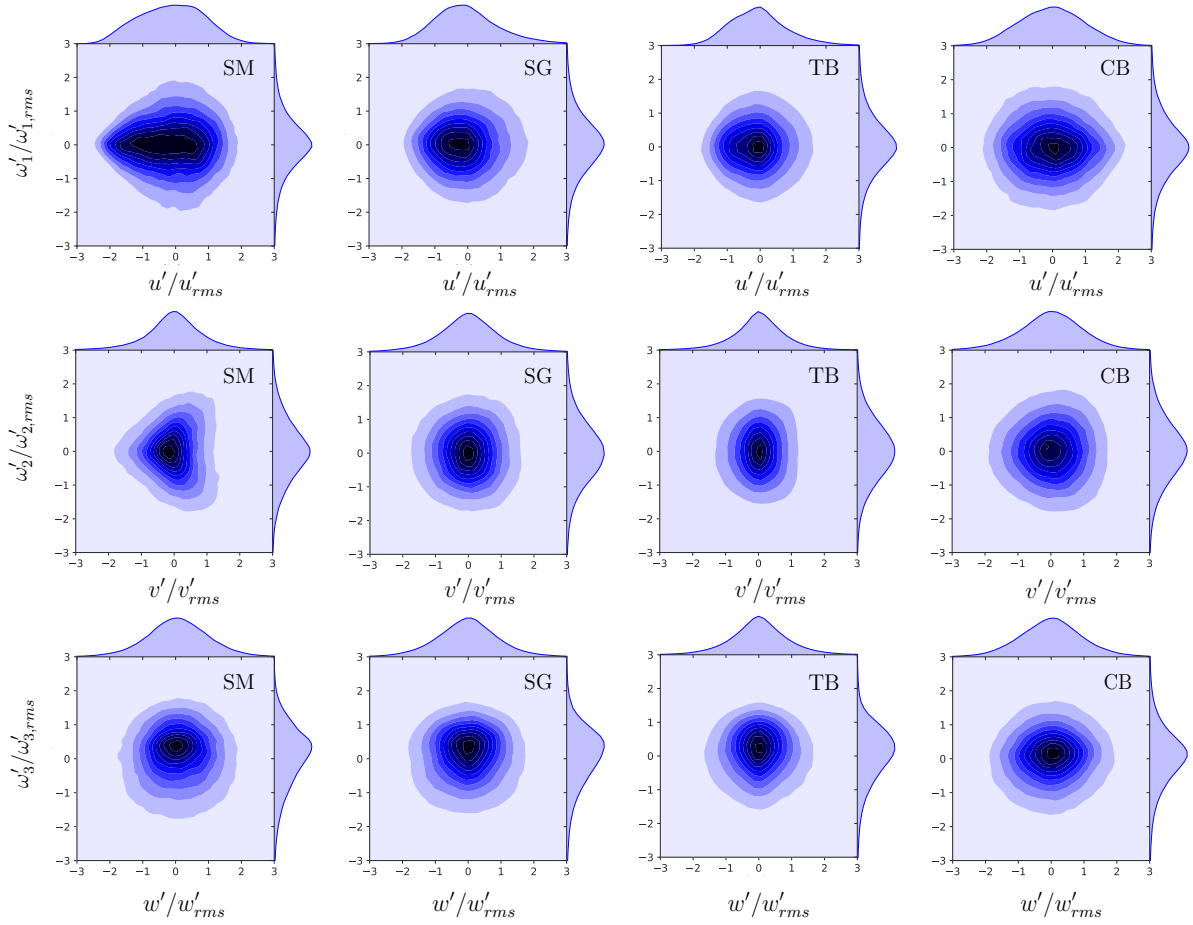

Figure 3.11: Joint PDFs of instantaneous values of u'_α and ω'_α, normalized by their respective RMS values; data are from the wall-parallel plane at $y^+ = 15$ for smooth-wall flow and $y = d$ for SG, TB and CB roughness.

eddies (since, by definition, for an eddy λ_{ci} is greater than zero); an overall picture can be formed on how all types of relevant eddies are modified by the roughness, which is especially helpful for a qualitative comparison of vortex shape around random roughness geometries. Second, compared to a vector event, which is dependent on the direction of the specified event, such as the Q_2 event used by Zhou et al. [72], the $\lambda_{ci} > 0$ event will be independent on the direction. It is also noted that the limitation of such approach is that it does not offer location-specific information on the shape of relevant eddies; however, this is not critical as here we focus on the average eddy shape.

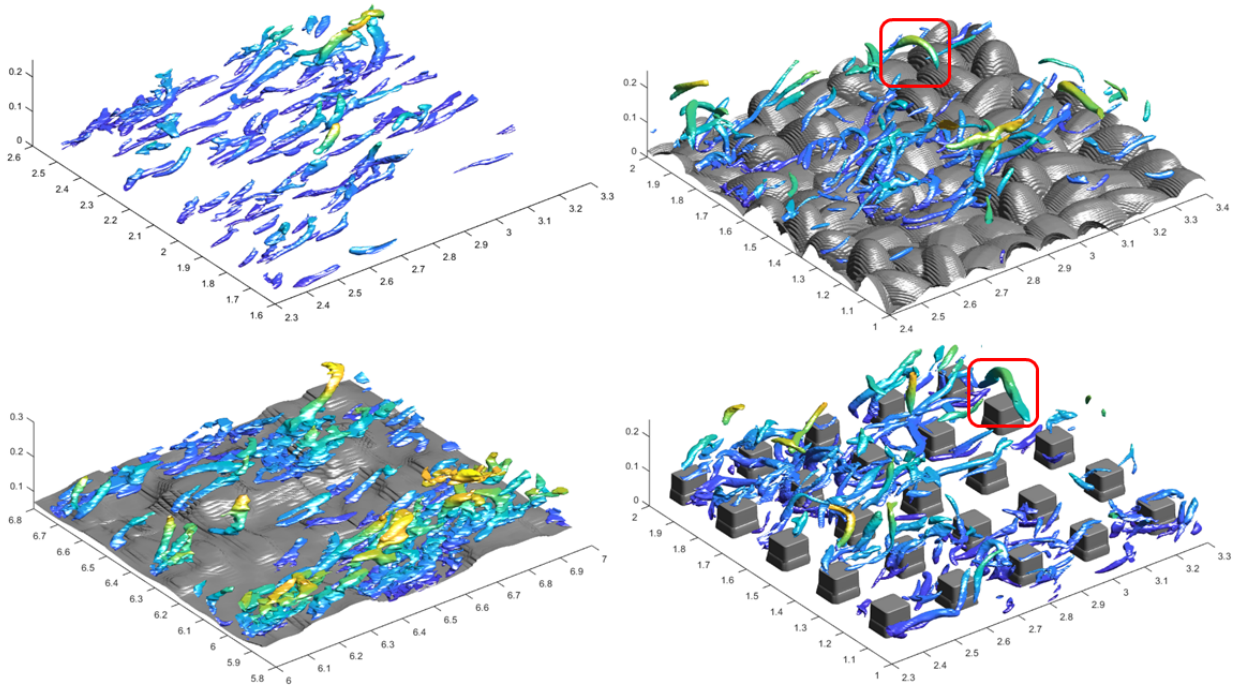

Figure 3.12: Instantaneous vortical motions, visualized by iso-surfaces of $\lambda_{ci} = 0.2\lambda_{ci,max}$, colored according to distance from the wall.

The conditional velocity field at displacement $\boldsymbol{r}$ from the point $\boldsymbol{x}$ is determined as

$$\left\langle \boldsymbol{u'}(\boldsymbol{x}+\boldsymbol{r}) \middle| \lambda'_{ci}(\boldsymbol{x}) > 0 \right\rangle \Big|_{\lambda'_{ci}=\lambda'_{ci,s}} = \frac{\left\langle \boldsymbol{u'}(\boldsymbol{x}+\boldsymbol{r})\lambda'_{ci}(\boldsymbol{x}) \right\rangle}{\left\langle \lambda'_{ci}(\boldsymbol{x})\lambda'_{ci}(\boldsymbol{x}) \right\rangle} \lambda'_{ci,s}, \tag{3.5}$$

with $\lambda_{ci} > 0$ being the event. Here, $\lambda'_{ci,s}$ is equal to one and acts as a dummy variable, since the results shown in the visualizations are normalized. We use the data of all (x, z) locations at a specified event elevation, to calculate equation (3.5). Therefore the shape of conditional eddies will be function of y only. The conditional eddies are visualized as the iso-surface of swirling strength of the obtained conditional velocity field. They are shown in figure 3.13 at various elevations for all cases. A sensitivity analysis was carried out to ensure that the overall comparison of vortex shape is independent of the thresholds used. The near-wall elevations compare $y^+ = 15$ and 40 in the smooth case with $y = d$ and $y = k_c$ in the rough cases. The outer-layer elevation is located at $y/\delta = 0.2$. Note that, in figure 3.13, the rough surfaces are plotted to illustrate the size and elevation of the eddies only and not to show the exact (x, z) locations of such coherent motions.

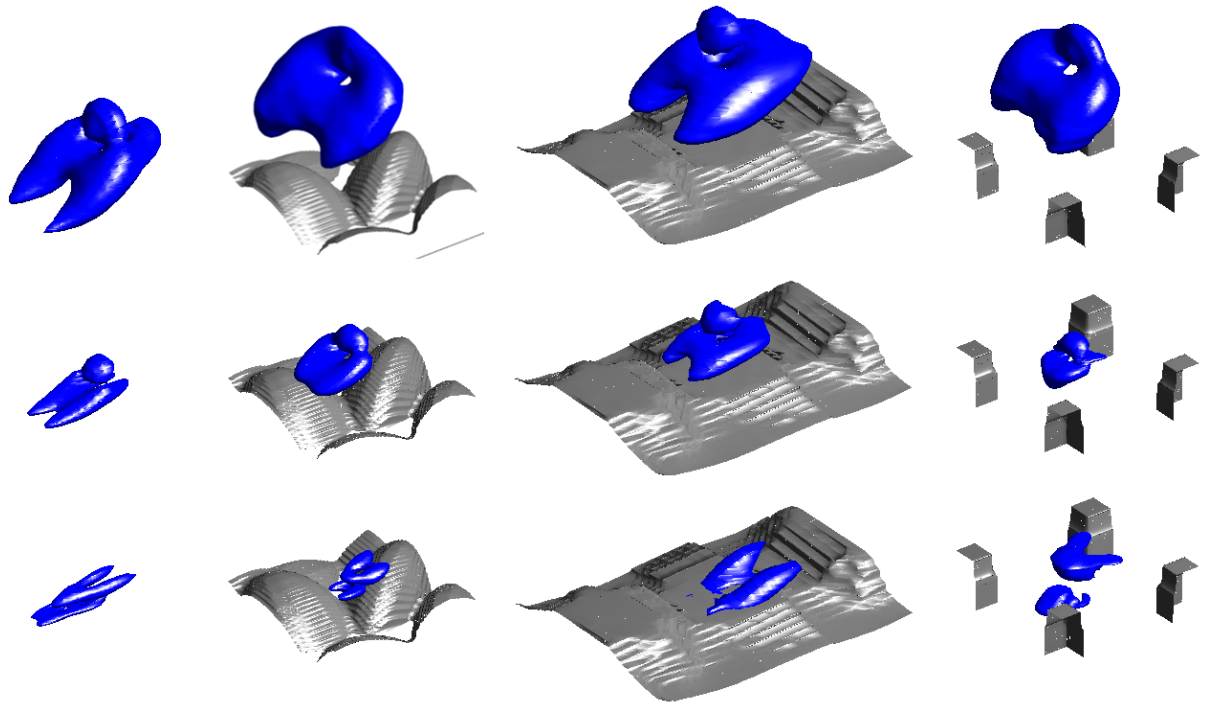

Figure 3.13: Conditional eddies based on an event of $\lambda_c > 0$, at three y locations; from bottom to top, $y^+ = 15$, $y^+ = 40$, $y/\delta = 0.1$ for SM; and $y = d$, $y = k_c$, $y = 0.2\delta$ for SG, TB and CB roughness. Plots are iso-surfaces of $\lambda_{ci} = 0.4$ obtained from the conditional velocity field.

In the buffer layer ($y^+ = 15$) of the smooth case, the conditional eddy comprises pairs of inclined streamwise-aligned vortices, with a bifurcation. This is because the quasi-streamwise vortices are not strictly aligned in x but tilted toward both positive and negative z-directions with equal probabilities [71]. The conditional eddy at $y = d$ for TB roughness is similar to the smooth case because the quasi-streamwise vortices are also present in the troughs of δ-scale undulations of this roughness. At $y = d$, both the SG and CB cases show a pair of vortices with three-dimensional shapes. For SG roughness, it is evident that a head-up and a head-down U-shape vortices are both present. The lower vortex appears to represent the vortex formed due to shear-layer roll-up wrapping around the recirculation region downstream of a roughness element [101]. The upper vortex appears similar to the head-down horse-shoe vortex observed by Talapatra and Katz [18], which is formed as both ends of an incoming spanwise-aligned vortex undergo stretching in x (due to mean-flow channeling on both sides of the cube) and lifting (due to interactions with the adjacent vortices of the same kind).

At $y^+ = 40$, the smooth-wall flow in figure 3.13 has an infant hairpin structure, which is produced by quasi-streamwise structures at this location, and grows self-similarly in the logarithmic region to a mature hairpin structure at $y^+ = 100$. A similar process seems to take place for TB roughness, where quasi-streamwise structures, generated in the undulating parts of the roughness, merge together and produce a structure that conforms with the roughness shape and also grows self-similarly to a mature structure at $y/\delta = 0.2$. The mature structure inherits features of both the hairpin structure (legs and the ring, visible in the mature hairpin of SM at $y^+ = 100$) and the surface topography. The similarity of the near wall conditional eddies of SM and TB implies that coherent structures in flow over TB roughness obey a similar growth mechanism to those in smooth-wall flows, such as the *streak transient growth* mechanism of Schoppa and Hussain [102].

The conditional eddy for CB roughness at $y = k_c$ consists of what appears to be a pair of arches, the horizontal one of which may be explained by the roll-over mechanism in Section 3.2.6. This mechanism is thought to cause significant sweeping (Q4) events and to shorten the vortical motions in the streamwise direction. Their shortened streamwise length scale (confirmed by figure 3.3) in flow over CB roughness is inherited by the structure observed at $y/\delta = 0.2$, where a hairpin-type structure with small legs is visible. The shape of the conditional eddy on SG roughness at $y = k_c$ seems to evolve through a combination of the mechanisms on both TB and CB roughnesses.

In the overlap regions and above ($y \geq 40$ for the smooth case and $y \geq y_R$ for the rough cases), the conditional eddies of all cases display a connection between the pair of parallel vortices, comprising spanwise-aligned portions that resemble the horse-shoe heads. A comparison of the size of the conditional eddies shows that, far from the wall, spanwise spatial extents of the eddies are all very similar, while the streamwise extents are shorter for SG and CB roughnesses compared to TB roughness and the smooth wall due to the shortened legs. Near the wall, shorter x extents of the vortical motions are also observed on SG and CB compared to TB and the smooth wall, possibly resulting from the difference in eddy shape and orientation. The z extents, however, are larger in the cases of TB and CB roughnesses, as these two roughness geometries impart larger spanwise length scales to the flow.

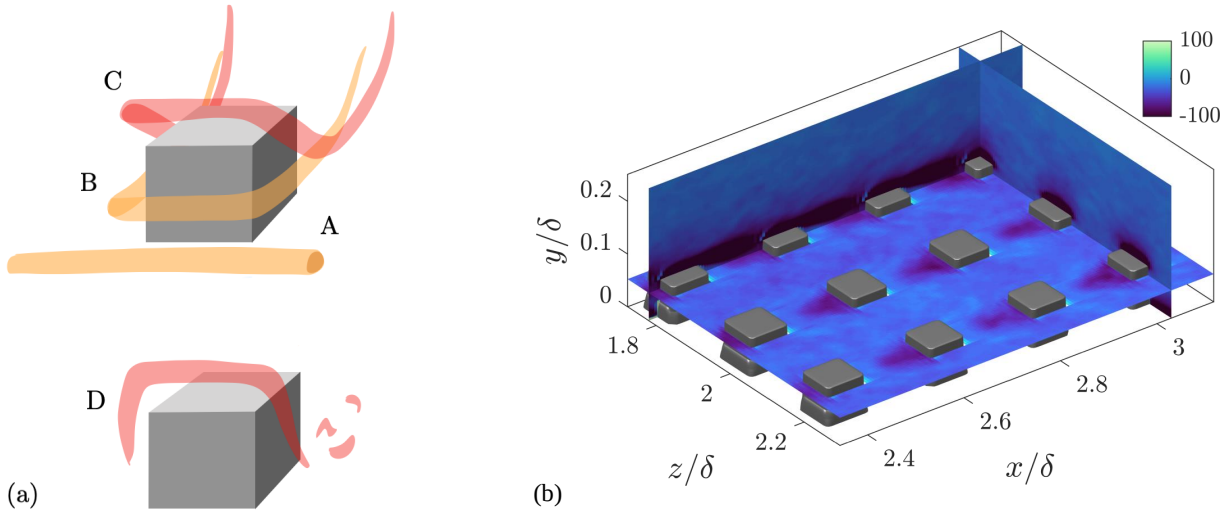

Figure 3.14: (*a*) Sketch of evolution of a spanwise vortex approaching a cube element, and (*b*) Mean spanwise vorticity, $\overline{\omega}_3 = d\overline{v}/dx - d\overline{u}/dy$, normalized by u_τ and δ. The horizontal plane is at $y = 0.75k_c$.

3.2.6 A kinematic process of vortices in local shear layers

In this section, we describe a kinematic rotational mechanism, referred here as a *roll over* mechanism, which may be undergone by a significant number of vortical structures in CB and, to a lesser extent, in SG roughness. This mechanism is thought to contribute to local TKE production and to a shorter x-extent of coherence in these cases, compared to the smooth and TB surfaces. A sketch is shown in figure 3.14 (a). As the head-down horse-shoe vortex wrapping around a cube element (vortex B) develops from an incoming spanwise vortex filament (vortex A)—similar to the process described by Talapatra and Katz [18]—the head of this vortex is lifted (by convection) by the mean-flow ejection immediately upstream of the cube (where $\overline{v} > 0$), while the legs are convected both downstream (due to channeling phenomenon, $\widetilde{u} > 0$ on both sides of the cube) and upward (due to mutual induction between adjacent legs). The resultant vortex takes a shape similar to that of Vortex C. As the head portion of vortex C moves downstream near the top surface of the cube, it is subject to intense time-mean spanwise vorticity ω_z of a negative sign (shown in figure 3.14 b). Consequently, the head portion undergoes clockwise solid-body rotation and rolls over cube elements. Meanwhile, the leg portions of vortex C, as they are inclined upward, undergo

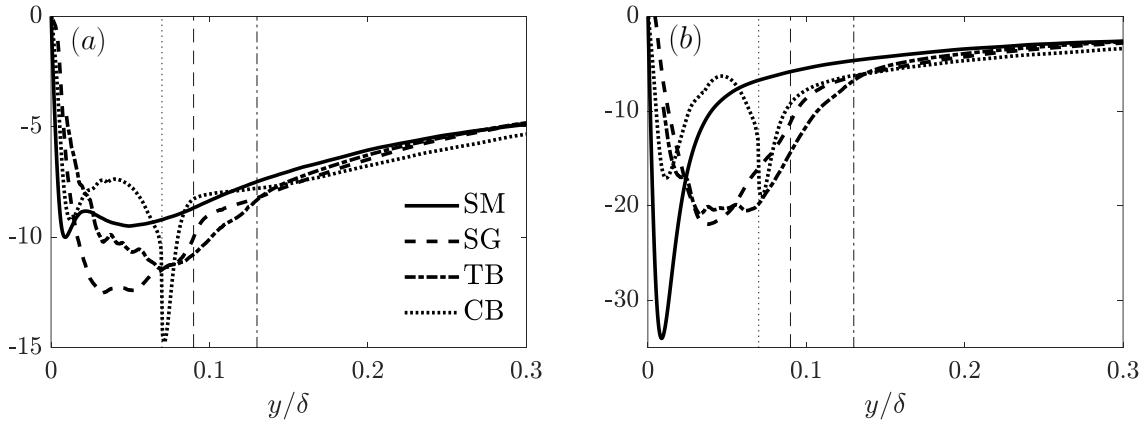

Figure 3.15: Profiles of $\langle \overline{V}_{r,z} \rangle$ (*a*), and $\langle \overline{\Omega}_z \rangle$ (*b*), normalized by u_τ and δ. The vertical lines are the corresponding crest locations.

stretching by positive $\partial\langle\overline{u}\rangle/\partial y$ and quickly break down due to non-linear interaction with other vortices. The result is a significantly shorter streamwise extent of the coherent motions (vortex D). In the averaged eddy conditioned at elevation of k_c shown in figure 3.13, the aforementioned vortical motion may manifest itself as an arch-shaped structure roughly oriented in the (x, z) plane.

Such a process is a result of a relatively flat top surface of a horizontally sizable roughness element; the local elevation of this surface into the flow (and the strong local ω_z in its vicinity as a result) leads to the aforementioned solid-body rotation of the vortex. For the TB roughness with mostly sharp protuberances, this process is probably less pronounced. It should be pointed out that the sketch represents ideal processes leading to the roll-over mechanism; in reality some of the structures may partially roll over the roughness elements, or may only have one-sided features. Those structures highlighted in figure 3.12 may be examples of instantaneous vortices that are in stage D.

In the following, evidence is provided to support the existence of such z-aligned vortices located in the vicinity of the top surface of a cube. Such a mechanism requires the existence of z-aligned vortex tubes in regions of strong $\overline{\omega_z}$ on cube surfaces. To this end, the eddy's axis-of-rotation around the cube is quantified, in an average sense, by two identifiers. First, $\boldsymbol{V}_r$, which is inferred

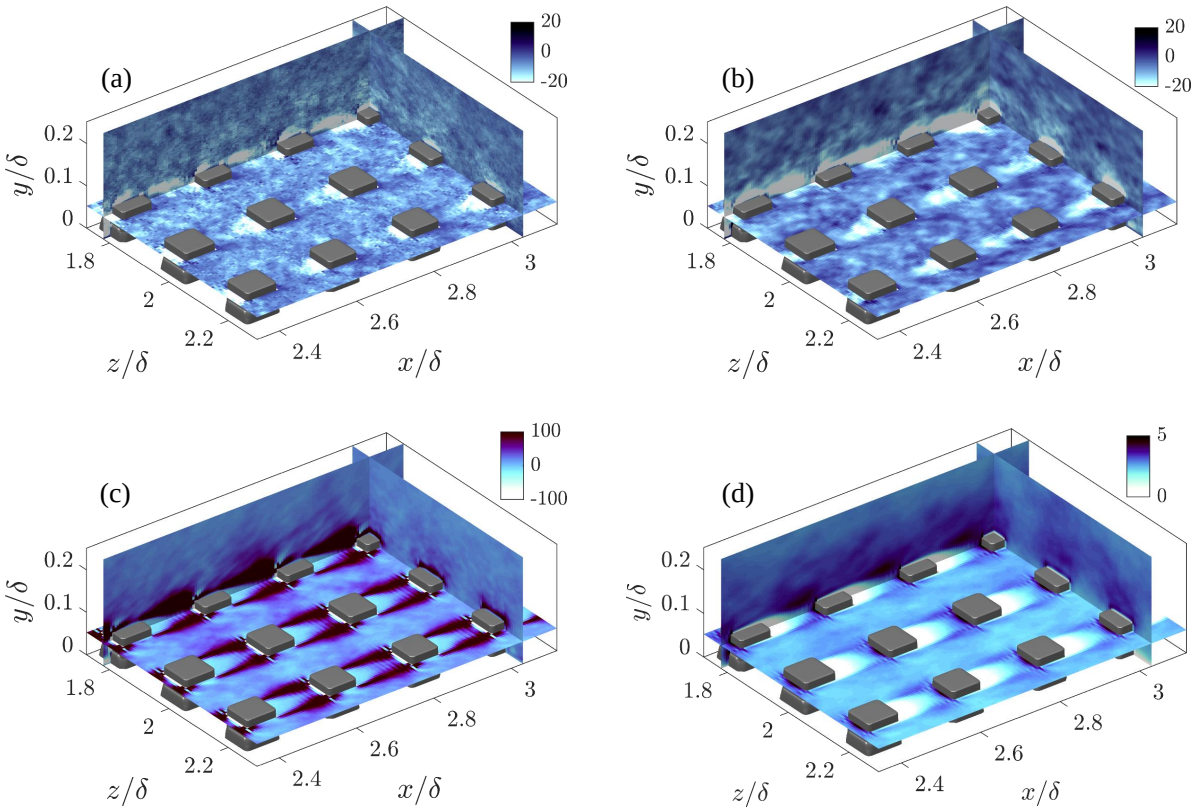

Figure 3.16: Contours of (*a*) $\overline{V}_{r,z}$, (*b*) $\overline{\Omega}_z$, (*c*) time-averaged shear production of TKE, $P_s = -\overline{u_i' u_j'}\partial\overline{u_i}/\partial x_j$, and (*d*) TKE. Case CB. Normalization is done using u_τ and δ. The horizontal planes are at $y = 0.75k_c$.

from the eddy-visualization method of Zhou et al. [72], and is introduced here as

$$\boldsymbol{V}_r(\boldsymbol{x},t) = -\boldsymbol{v}_r(\boldsymbol{x},t)\lambda_{ci}(\boldsymbol{x},t), \tag{3.6}$$

where $\boldsymbol{v}_r$, a unit vector, is the normal eigenvector of the velocity-gradient tensor corresponding to the real eigenvalue (the other two eigenvalues being complex conjugates by definition of swirling motion). And, second, $\boldsymbol{\Omega}$ ($= \lambda_{ci}\boldsymbol{\omega}/|\boldsymbol{\omega}|$), which is the three-dimensional extension of the method used in Anderson et al. [103, they used signed swirling strength in x_i-direction, $\lambda_{ci}\omega_i/|\omega_i|$ to account for the eddy's axis of rotation in that direction].

Both $\boldsymbol{V}_r$ and $\boldsymbol{\Omega}$ weigh the local axis-of-rotation of an eddy with its local swirling strength λ_{ci} to account for the effect of eddy strength in the statistics. Therefore, a high magnitude of the time-averaged value of their i^{th} component, $|\overline{V}_{r,i}|(\boldsymbol{x})$ or $|\overline{\Omega}_{r,i}|(\boldsymbol{x})$, indicates local strong swirling motions

around the x_i axis in an average sense. The wall-normal profiles of $\langle \overline{V}_{r,z} \rangle$ and $\langle \overline{\Omega}_z \rangle$ are shown in figure 3.15(a) and (b), respectively, and are compared among all cases. We have introduced the new identifier $\boldsymbol{V}_r$, since the $\boldsymbol{\Omega}$, based on the ω_z' field, can be quantitatively 'contaminated' by non-vortical structures, such as streaky motions, due to the strong $\partial u'/\partial y$ they generate. This is evident in the profile of SM in figure 3.15(b), where the large values of $|\langle \overline{\Omega}_z \rangle|$ near the wall (at $y^+ \approx 15$) is attributed to the dominance of streaky motions in this region. Although it is expected that due to the roughness effect, the spanwise rotation is more significant for rough walls than the smooth wall, comparison between smooth and rough walls profiles of $|\langle \overline{\Omega}_z \rangle|$ do not reflect such a trend. The $\boldsymbol{V}_r$ identifier is based on the vortex visualization method; therefore, non-vortical motions would have small contribution to it. In figure 3.15(a), one notices the magnitude of $|\langle \overline{V}_{r,z} \rangle|$ for rough walls matches that of smooth wall, consistent with the aforementioned trend. Using either of these identifiers, the following discussions would remain unchanged.

In figure 3.15(a), the high-magnitude peak of $\langle \overline{V}_{r,z} \rangle$ (with a negative sign) located at the crest level of CB roughness, which is greater than other locations for more than 40%, indicates significant strength of z-aligned, clockwise-rotating vortices at this elevation. In addition, the spatial distribution of $\overline{V}_{r,z}$ around CB roughness in figure 3.16(a) shows that z-aligned eddies with high swirling strengths are found in the regions immediately upstream of a cube element and near its top surface; such eddies are also prevalent in the wake region of a cube. Moreover, in figure 3.14(b), it is shown that regions of strong $\overline{\omega}_z$ of the negative signs, coincide with the region with strong $|\overline{V_{r,z}}|$ (figure 3.16a) near the top surface of a cube. These evidences, along with the results of conditional eddies discussed in Section 3.2.5, support the existence of the aforementioned solid-body rotation process of the head-down horse-shoe vortex head, which leads to a shortened x-extent of coherent motions.

Another important aspect of this process is that it is expected to yield significant TKE production at the top surface of a cube. At this location the spanwise-aligned head of vortex C and vortex D in figure 3.14(a) together with the two legs induce intense Q_4 motions This yields significant local shear production of TKE driven by the strong $\partial \overline{u}/\partial y$ values within the thin shear layer. The spatial

distribution of local shear production of TKE, $P_s = -\overline{u_i' u_j'} \partial \overline{u_i} / \partial x_j$ (summed over $i, j = 1, 2, 3$) is plotted in figure 3.16(c), showing high values in the vicinity of the upper surface of a cube element. This also results in regions of intensified turbulence kinetic energy above each roughness element, as depicted by figure 3.16(d).

3.3 Concluding remarks

Turbulence structures in fully-developed channel flows at $Re_\tau = 1000$ have been analyzed for flow over a smooth wall (SM), and flows over a realistic turbine-blade surface (TB), a sandgrain surface (SG), and a k-type cube (CB) surface. The results presented here appear to be consistent with the following qualitative description of turbulent boundary layers over rough surfaces. When compared to flow over a smooth surface, the bulk drag force over each rough surface considered here (table 2.1) is significantly larger. It is because the increase in form drag caused by the particular size, shape, and distribution of roughness elements exceeds the corresponding reduction in viscous drag on account of roughness-induced disruption of the viscous sublayer [13]. The magnitude of the increase in form drag depends upon the individual surface roughness topography and, in this study, is approximately twice as large for SG and CB roughness as it is for TB roughness. The second principal effect of surface roughness is to modify near wall coherent motions and, consequently, to modify turbulence processes in this region. The penetration extent of roughness effects is mostly in the roughness sublayer. However it can go beyond this region depending on the type of the roughness, due to the limited δ/k_c ratio. The significant modifications to near wall coherent motions, caused by different roughness geometries presented here, are: *i*) the smooth-wall quasi-streamwise vortices are retained over TB roughness within δ-scale undulations, whereas they are replaced by a pair of 'head-up, head down' horse-shoe vortices over SG and CB rough surfaces; *ii*) The longitudinal extent of near wall vortical structures over smooth wall is retained in the TB roughness, but it is shortened significantly for SG and CB rough surfaces, which is in part due to a solid-body rotation process of the head-down horse-shoe vortices on account of the strong shear layer above a roughness protuberance. This effect is inherited in vortical motions in the roughness

sublayer and beyond. Evidence supporting the existence of such process in case CB is provided by analyses of linear stochastic estimation and eddy-axis-of-rotation. The results suggest that the process concerns a considerable number of eddies at the roughness crest, and may have a substantial influence on turbulence intensities and shear production of turbulence kinetic energy. *iii*) The effect of shortened structures in flows over SG and CB is to reduce the energy level at low wavenumbers (energy containing eddies), while increasing energy level at higher wavenumbers, which are closer to the dissipative scales. In stationary turbulent flows, the enhanced dissipation requires enhanced production of turbulence energy (required by equilibrium condition), leading to increase in drag work, on account of surface roughness.

The strong dependence of the near-wall flow on surface texture is also revealed by profiles of $R_{u_i u_j,n}$, which exhibit surface periodicity, and velocity spectra which contrast the different cascades of energy from large-scale to small-scale motions for rough and smooth wall flows. Joint PDF profiles of $(u'_\alpha, \omega'_\alpha)$ show that roughness weakens low-speed streaks and results in roughly equal possibilities for all types of motions, yielding more isotropic flow in this region. Roughness also increases the inclination angles of large-scale structures near the surface. At $y = d$, conditional eddies obtained by linear stochastic estimation are very similar for flow over smooth walls and TB roughness: they are two bifurcated streamwise vortices. For flow over SG and CB roughness, they are a pair of horse-shoe structures, one on top of the other. The lower one is conjectured to be produced by shear-layer roll-up in the wake behind roughness elements, and the upper one is similar to the U-shape structure observed by Talapatra and Katz [18], which is produced by vortex stretching due to flow channeling.

In the outer boundary layer, Townsend's similarity appears to apply to the single-point statistics, the average inclination angles of energy-containing coherent motions, velocity spectra, helicity characteristics (joint PDF of u'_α, ω'_α) and the average shape of turbulent eddies. However streamwise two-point velocity correlations and associated length scales are surface-texture dependent in this region, probably due to the limited δ/k_c used herein. Streamwise length scales, obtained by profiles of $R_{u_i u_j,n}$ and conditional eddies, for SG and CB roughness are shorter than those over smooth

walls and TB roughness.

The results discussed here are for the values of turbulence Reynolds number and δ/k_c permitted by today's capabilities in direct numerical simulations. A more detailed understanding of the near wall physics and its connection to the outer-layer region for flows over rough walls at higher values of Re_τ and δ/k_c, remains an interesting challenge for the future. Other future work might include structural comparison with various roughness textures with matching k_s^+ (or the drag).

CHAPTER 4

DATA-DRIVEN PREDICTION OF THE EQUIVALENT SAND-GRAIN HEIGHT IN ROUGH-WALL TURBULENT FLOWS

4.1 Introduction

At sufficiently high Reynolds numbers all surfaces are hydrodynamically rough, as is almost always the case for flows past the surfaces of naval vehicles. Reviews of roughness effects on wall-bounded turbulent flows are provided by Raupach et al. [14] and Jiménez [13]. The most important effect of surface roughness in engineering applications is an increase in the hydrodynamic drag [36], which is due predominantly to the pressure drag generated by the small-scale recirculation regions associated with individual roughness protuberances.

For the foreseeable future, the most practical approach to making predictive flow calculations for many realistic applications is to use engineering one-point closures of turbulence, such as two-equation turbulence eddy-viscosity models to the Reynolds-averaged Navier-Stokes (RANS) equations. Existing rough-wall corrections to this type of closure typically model the increase in hydrodynamic drag on a single length scale—the equivalent sand-grain height [48] k_s—without physically resolving the surface or changing the governing equations. In the fully rough flow regime, where the wall friction depends on the roughness alone and is independent of the Reynolds number, k_s was observed to quantify the increase in hydrodynamic drag through the empirical relation with the roughness function, ΔU^+ (defined as the offset of the log-linear velocity profile of a rough-wall flow relative to that of a smooth-wall one):

$$\Delta U^+ = \frac{1}{\kappa} \ln k_s^+ - 3.5, \tag{4.1}$$

where $\kappa = 0.41$ is von Kármán's constant and + represents normalization in wall units.

A universal length scale (e.g. k_s in Nikuradse's relation, or ϵ in the Moody diagram [2]) that can predict accurately the surface drag coefficient is not known a priori and does not appear to be equivalent to any single geometrical length scale, such as an average or a root-mean-square (RMS)

of roughness height [36]. It is also well-established that k_s can depend on many geometrical parameters such as the effective slope [37, 5] and the skewness of the roughness height distribution [38]. Readers are referred to Flack & Schultz [38] and Bons [104] for extensive reviews on this topic. Empirical expressions for k_s based on a small number of geometrical roughness parameters include, among others:

$$k_s = c_1 k_{avg}\left(\alpha_{rms}^2 + c_2\alpha_{rms}\right), \quad k_s = c_1 k_{avg}\Lambda_s^{c2}, \quad \text{and} \quad k_s = c_1 k_{rms}\left(1 + S_k\right)^{c2}, \tag{4.2}$$

proposed by Bons et al. [105], van Rij et al. [106] and Flack & Schultz [38] respectively. Here k_{avg} is the average height, α is the local streamwise slope angle and $\Lambda_s = \left(S/S_f\right)\left(S_f/S_s\right)^{-1.6}$ (where S, S_f, S_s are, respectively, the platform area, the total frontal area, and the total windward wetted area of the roughness) while k_{rms} and S_k are the rms and skewness of the roughness height fluctuations, and c_1 and c_2 are constants.

The hydrodynamic lengthscale k_s appears to be correlated with different sets of geometrical parameters for each type of rough surface and no universal correlation currently exists for flow over surfaces of arbitrary roughness. For example, for synthetic roughness comprising closely packed pyramids [107] and random sinusoidal waves [37], it has been shown that k_s scales on the effective slope when the surface slope is gentle (i.e. within the 'waviness' regime), whereas the skewness and rms height, but *not* slope magnitude, become important when the slope is steeper (i.e. within the 'roughness' regime). The boundary between these two regimes has been shown to be surface dependent [5].

Some more recent studies of k_s correlations are summarized below. Thakkar et al. [108] carried out DNS of transitionally-rough turbulent flows for different irregular roughness topographies. They found that the roughness function is influenced by solidity, skewness, the streamwise correlation length scale and the rms of roughness height. Flack et al. [109] performed several experiments to systematically investigate the effects of the skewness and amplitude of roughness height on the skin friction. They found that the rms and skewness of roughness height fluctuations are important scaling parameters for prediction of roughness function; however, the surfaces with positive, negative and zero skewness values needed different correlations. Also, Chan et al. [110] simulated

turbulent pipe flows over sinusoidal roughness geometries and confirmed strong dependence of roughness function on the average height and streamwise effective slope.

In previous studies, the small number of roughness parameters used to devise k_s correlations tended to limit their application to a narrow range of surface roughnesses. Since it appears that many geometrical parameters, such as porosity, moments of roughness height (e.g. rms, skewness and kurtusis), effective slope, and surface inclination angle might affect k_s, it is useful to employ a data science approach suited to modeling large multi-variate/multi-output systems.

Specifically, we use Machine Learning (ML) to explore k_s-prediction approaches that depend on a large set of surface-topographical parameters, with the expectation that the resulting models may be applied accurately to a wider range of surfaces. Since the prediction of k_s from surface topography is essentially a labeled regression problem, supervised ML operations were performed using Deep Neural Networks (DNN) and Gaussian Process Regressions (GPR). Both methods are explained thoroughly in section 4.3. Readers are referred to the monograph by Rasmussen & Williams[111] and the review provided by LeCun et al. [112] for detailed descriptions of these methods.

An initial ensemble of 60 sets of data on k_s as a function of topographical parameters—45 direct numerical simulation (DNS) results and 15 experimental results—was considered. All experimental data sets are fully rough, and of the DNS data, 30 are considered fully-rough flows; all fully-rough cases were used for ML training and testing. To the best of our knowledge, this ensemble of roughness geometries is the most extensive used for developing a k_s-prediction method.

In this chapter, we first present simulation parameters and different roughness topographies and then discuss the post-processed DNS results used to calculate k_s for each surface. Finally, we describe the ML models, their predictions of k_s and their uncertainty.

4.2 Problem formulation

The methodology of this chapter is similar to that in chapter 2. Please refer to section 2.2 as for definition of different parameters and mathematical symbols.

4.2.1 Surface roughness

In figure 4.1, surface plots of the 45 roughness geometries used in these simulations are displayed; their statistical properties are given in table 4.1. Each case name in figure 4.1 and table 4.1 begins with the letter C or E, which denotes whether the data is computational or experimental, followed by an identifying index for that particular surface. For computational cases, this index is followed by: a characteristic length scale (as a percentage of δ) used for roughness synthesis; an identifier of whether the surface roughness is regular (reg) or random (rnd); and finally an identifier for one additional surface feature and its position in a series of surfaces with different sizes of that feature. These features were: the streamwise inclination angle I_x in surfaces C01 to C12; the porosity P_o in surfaces C13 to C24; and the streamwise effective slope E_x in surfaces C25 to C30. For the experimental data two indices were assigned to each surface. The first denotes the year in which the data were published and the second is the surface designation in that publication. Thus surfaces with index 16 are from Flack et al. [113], those with index 18 are from Barros et al. [114], and those with index 19 are from Flack et al. [109]. Note that these experimental data were obtained from fully-developed channel flows, where the drag was measured through the pressure drop along the channel. Thus their results are expected to be more accurate than those of boundary layer studies where the drag is usually inferred.

Surfaces C01 through C24 were created using ellipsoidal elements [54] of different size, aspect ratio and inclination. For *regular* roughness, each element had the same orientation and semi-axis lengths, $(\lambda_1, \lambda_2, \lambda_3) = (1.0, 0.7, 0.5)k_c$, where k_c is the peak-to-trough height (also called the crest height). For *random* roughness, the elements had random orientations and semi-axis lengths (with uniform distributions of the random variables). The average orientation and semi-axis lengths for *random* roughness were the same as the corresponding *regular* surface. Surfaces C25 through C30 comprised sinusoidal waves in the x direction, of the same magnitude but different wavelengths, to generate different values of effective slope E_x. The wavelengths were $3\delta/4$, $3\delta/8$ and $\delta/6$. Surfaces C31 and C37 comprised the random sand-grain roughness of Scotti, which were produced by randomly oriented ellipsoidal elements with fixed semi-axes of $(1.0, 0.7, 0.5)k_c$. Surfaces C32

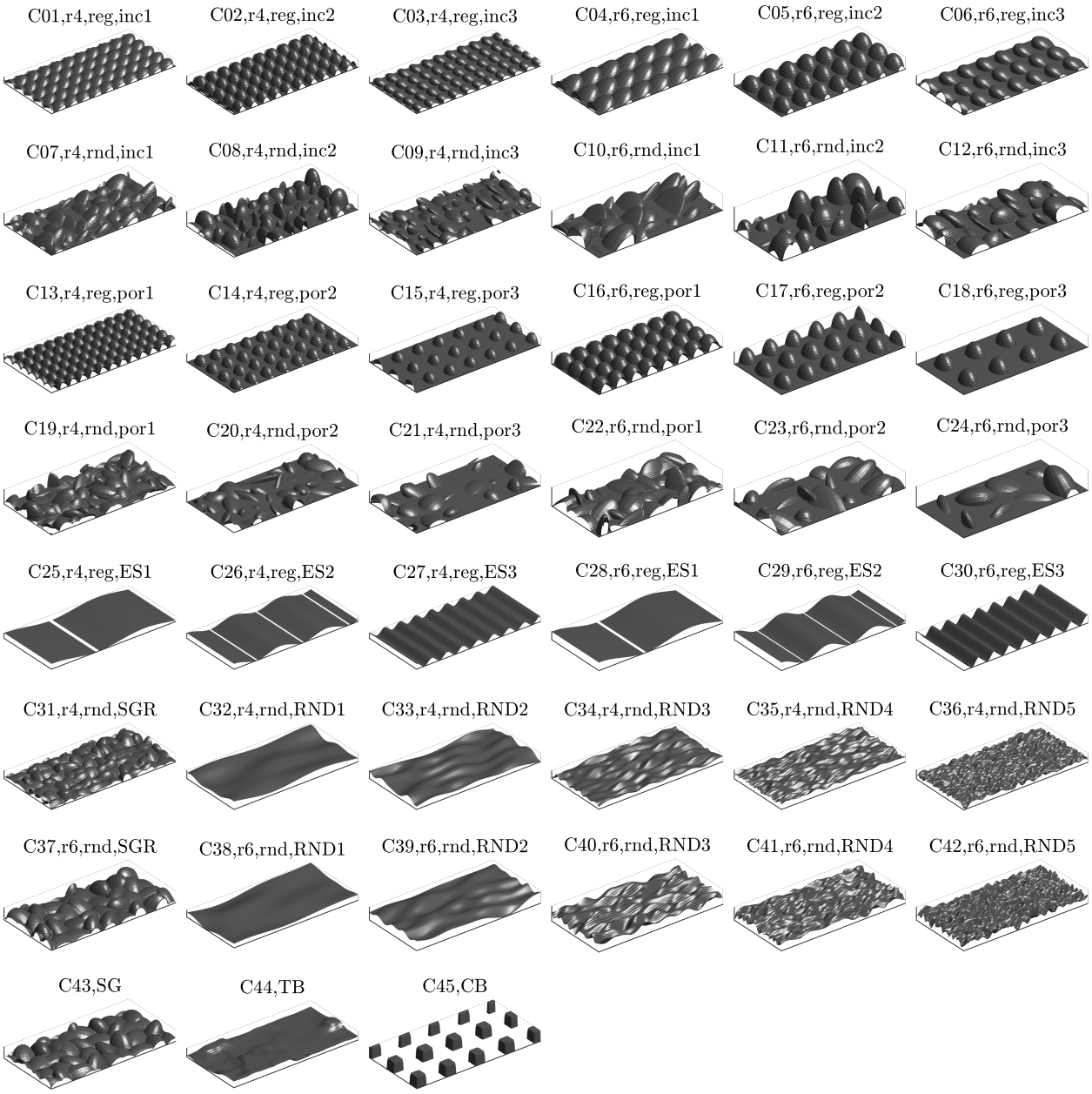

Figure 4.1: Roughness geometries — each plot is a section of size $\delta \times 0.5\delta$ in the x-z plane. Cases C43 to C45 are from simulations with regular domain sizes [5, 6].

Case name	k_{avg}	k_c	k_t	k_{rms}	R_a	I_x	I_z	P_o	E_x	E_z	S_k	K_u	k_S
C01,r4,reg,inc1	0.026	0.043	0.043	0.013	0.011	-0.801	-0.089	0.535	0.584	0.510	-0.544	2.177	
C02,r4,reg,inc2	0.030	0.059	0.059	0.021	0.019	0.012	0.032	0.609	1.029	0.562	-0.265	1.597	
C03,r4,reg,inc3	0.025	0.043	0.043	0.013	0.011	0.821	-0.078	0.537	0.600	0.485	-0.459	2.052	
C04,r6,reg,inc1	0.032	0.064	0.064	0.022	0.019	-0.978	0.016	0.597	0.595	0.590	-0.167	1.601	0.064
C05,r6,reg,inc2	0.038	0.088	0.088	0.033	0.030	0.025	0.064	0.654	0.916	0.643	0.109	1.436	0.124
C06,r6,reg,inc3	0.031	0.064	0.064	0.022	0.019	0.955	0.121	0.599	0.588	0.558	-0.087	1.590	0.059
C07,r4,rnd,inc1	0.025	0.086	0.084	0.022	0.019	-0.860	0.033	0.774	0.511	0.559	0.560	2.244	0.136
C08,r4,rnd,inc2	0.027	0.116	0.115	0.030	0.025	-0.007	0.048	0.819	0.861	0.604	0.870	2.627	0.322
C09,r4,rnd,inc3	0.025	0.083	0.081	0.021	0.018	0.829	0.002	0.753	0.517	0.482	0.514	2.292	0.131
C10,r6,rnd,inc1	0.026	0.125	0.120	0.030	0.025	-0.957	-0.019	0.835	0.498	0.578	0.967	2.874	0.269
C11,r6,rnd,inc2	0.033	0.172	0.169	0.044	0.037	0.076	0.138	0.842	0.758	0.543	1.150	3.176	0.536
C12,r6,rnd,inc3	0.032	0.127	0.121	0.032	0.027	0.923	0.032	0.784	0.508	0.471	0.758	2.642	0.272
C13,r4,reg,por1	0.038	0.059	0.059	0.018	0.015	0.024	0.067	0.498	1.043	0.523	-0.820	2.508	
C14,r4,reg,por2	0.018	0.059	0.059	0.022	0.020	0.021	0.038	0.776	0.613	0.456	0.708	1.840	0.141
C15,r4,reg,por3	0.010	0.059	0.059	0.019	0.014	0.022	0.063	0.877	0.334	0.253	1.646	4.094	0.157
C16,r6,reg,por1	0.051	0.089	0.089	0.030	0.026	0.041	0.149	0.529	1.137	0.534	-0.538	1.873	0.077
C17,r6,reg,por2	0.022	0.089	0.089	0.031	0.027	0.041	0.080	0.801	0.537	0.403	0.982	2.308	0.260
C18,r6,reg,por3	0.013	0.089	0.089	0.026	0.020	0.057	0.126	0.886	0.307	0.230	1.849	4.839	0.247
C19,r4,rnd,por1	0.027	0.112	0.108	0.021	0.017	0.025	-0.107	0.806	0.487	0.486	0.732	3.422	0.158
C20,r4,rnd,por2	0.013	0.095	0.087	0.017	0.014	0.032	-0.646	0.896	0.311	0.323	1.343	4.126	0.106
C21,r4,rnd,por3	0.009	0.098	0.094	0.016	0.012	0.321	-0.741	0.929	0.219	0.233	2.168	7.728	0.103
C22,r6,rnd,por1	0.035	0.139	0.139	0.029	0.024	-0.070	-0.245	0.791	0.456	0.499	0.591	2.830	0.277
C23,r6,rnd,por2	0.017	0.123	0.111	0.025	0.020	-0.672	-0.841	0.885	0.305	0.325	1.467	4.347	0.175
C24,r6,rnd,por3	0.014	0.152	0.145	0.027	0.019	0.189	-0.056	0.926	0.254	0.257	2.371	8.740	0.260
C25,r4,reg,ES1	0.020	0.040	0.040	0.014	0.013	0.046	0.006	0.510	0.106	0.009	-0.032	1.503	
C26,r4,reg,ES2	0.021	0.040	0.040	0.014	0.013	0.039	-0.001	0.510	0.212	0.020	-0.071	1.505	0.065
C27,r4,reg,ES3	0.023	0.040	0.040	0.014	0.012	0.006	-0.023	0.510	0.609	0.032	-0.214	1.544	
C28,r6,reg,ES1	0.030	0.059	0.059	0.021	0.019	0.044	0.018	0.504	0.158	0.015	-0.031	1.499	0.071
C29,r6,reg,ES2	0.031	0.059	0.059	0.021	0.019	0.028	-0.069	0.504	0.316	0.022	-0.071	1.503	0.112
C30,r6,reg,ES3	0.034	0.059	0.059	0.020	0.018	0.015	-0.069	0.505	0.917	0.048	-0.203	1.543	0.064
C31,r4,rnd,SGR	0.025	0.059	0.059	0.011	0.009	0.104	-0.039	0.648	0.370	0.398	0.378	2.784	0.049
C32,r4,rnd,RND1	0.040	0.075	0.072	0.013	0.010	0.117	0.108	0.479	0.068	0.169	-0.069	2.991	
C33,r4,rnd,RND2	0.041	0.088	0.084	0.013	0.011	0.109	0.078	0.553	0.117	0.308	0.004	2.763	
C34,r4,rnd,RND3	0.042	0.080	0.071	0.010	0.008	0.070	0.051	0.508	0.175	0.458	-0.002	3.031	
C35,r4,rnd,RND4	0.043	0.077	0.066	0.008	0.007	0.039	0.042	0.488	0.218	0.558	0.013	2.941	
C36,r4,rnd,RND5	0.045	0.084	0.067	0.009	0.007	0.035	0.037	0.535	0.378	0.841	0.075	3.018	
C37,r6,rnd,SGR	0.037	0.088	0.088	0.018	0.015	0.312	0.180	0.640	0.428	0.463	0.323	2.686	0.109
C38,r6,rnd,RND1	0.060	0.106	0.091	0.016	0.012	0.045	0.028	0.444	0.077	0.183	-0.220	3.258	
C39,r6,rnd,RND2	0.061	0.098	0.095	0.012	0.009	0.111	0.057	0.400	0.108	0.285	-0.020	3.267	
C40,r6,rnd,RND3	0.064	0.121	0.112	0.016	0.013	0.061	0.022	0.512	0.280	0.760	0.037	2.977	0.050
C41,r6,rnd,RND4	0.065	0.130	0.130	0.015	0.012	0.045	0.037	0.546	0.374	0.989	0.028	3.036	
C42,r6,rnd,RND5	0.068	0.118	0.116	0.013	0.010	0.037	0.025	0.503	0.547	1.204	0.052	2.933	
C43,SG	0.036	0.089	0.087	0.017	0.014	0.288	0.156	0.649	0.425	0.441	0.476	2.970	0.093
C44,TB	0.055	0.125	0.088	0.018	0.014	0.007	-0.006	0.569	0.097	0.081	0.200	3.493	0.024
C45,CB	0.010	0.070	0.070	0.023	0.016	0.420	0.508	0.878	0.249	0.247	2.101	5.569	0.150
C46,r4,rnd,por3,FS	0.009	0.098	0.094	0.016	0.012	0.321	-0.715	0.929	0.219	0.234	2.168	7.728	0.104
E01,16,2	0.138	0.261	0.254	0.020	0.016	-0.005	0.011	0.472	0.720	0.835	-0.711	3.843	0.052
E02,16,3	0.143	0.252	0.252	0.021	0.016	-0.021	0.010	0.432	0.740	0.868	-0.338	3.159	0.050
E03,16,7	0.133	0.365	0.254	0.019	0.014	-0.038	0.000	0.638	0.618	0.705	-1.169	5.292	0.058
E04,16,8	0.126	0.298	0.227	0.017	0.013	-0.034	0.009	0.579	0.587	0.682	-1.445	5.421	0.056
E05,16,9	0.112	0.308	0.167	0.018	0.014	-0.031	0.015	0.637	0.636	0.753	-0.738	3.714	0.043
E06,16,15	0.081	0.191	0.191	0.013	0.010	-0.027	0.003	0.578	0.621	0.713	-0.687	3.854	0.035
E07,18,1	0.121	0.241	0.227	0.026	0.021	-0.013	-0.183	0.500	0.181	0.188	0.107	2.941	0.053
E08,18,2	0.143	0.276	0.255	0.032	0.025	-0.019	0.194	0.483	0.162	0.164	0.093	2.967	0.034
E09,19,1	0.204	0.398	0.344	0.046	0.036	0.042	-0.096	0.487	0.227	0.230	-0.080	2.989	0.065
E10,19,2	0.389	0.763	0.689	0.088	0.070	0.046	0.002	0.492	0.447	0.452	-0.065	2.925	0.200
E11,19,3	0.477	0.730	0.679	0.088	0.070	-0.029	-0.245	0.348	0.434	0.432	-0.660	3.274	0.160
E12,19,4	0.459	0.751	0.710	0.089	0.071	-0.052	0.036	0.391	0.455	0.459	-0.351	3.041	0.180
E13,19,5	0.292	0.732	0.650	0.090	0.072	-0.058	-0.004	0.602	0.445	0.452	0.346	3.051	0.245
E14,19,6	0.202	0.711	0.604	0.087	0.069	0.004	-0.010	0.716	0.391	0.400	0.812	3.559	0.435
E15,19,7	0.522	0.967	0.894	0.114	0.092	-0.050	-0.235	0.462	0.557	0.562	-0.066	2.794	0.230

Table 4.1: Statistical parameters of roughness topography and the equivalent sand-grain height k_s for each roughness geometry. R_a, k_{avg}, k_c, k_t, k_{rms} and k_s values from DNS are normalized by the channel half height δ, while corresponding experimental values are given in mm. k_s is not listed for cases thought to be transitionally rough.

through C36 and C38 through C42 were generated as the low-order (the first 5, 10, 20, 30 and 50) modes of Fourier transforms of white noise in the streamwise and spanwise directions; they therefore describe random surfaces with large- to small-wavelength roughness. Cases C43, C44 and C45 are DNS results from full-span channel computations of flow over surfaces of: random sand-grain roughness; the roughness found on a turbine blade [57]; and arrays of cubes [from the study of 6] respectively. Case C46 is a full-span DNS of case C21, generated to validate the minimal-channel approach of the preceding cases. A baseline smooth-wall flow was also simulated using a full-span channel [57].

The geometric parameters reported for each surface in table 4.1 are: roughness peak-to-trough height (also termed crest height) k_c (i.e. distance between the highest and the lowest surface points); mean peak-to-trough height k_t (i.e. the average of peak-to-trough heights obtained from surface tiles of size $\delta \times \delta$, similar to Forooghi et al. [115]); mean roughness height k_{avg}; first-order moment of height fluctuations R_a; root-mean-square k_{rms}, skewness S_k and kurtosis K_u of the roughness height fluctuations; surface porosity P_o; effective slope in the x_i direction E_{x_i}; and inclination angle (in radians) in the x_i direction I_{x_i}, together with the hydrodynamic lengthscale k_s deduced from the mean velocity field using equation (4.1).

These geometrical parameters are defined as:

$$k_{avg} = \frac{1}{A_t} \int_{x,z} k dA, \tag{4.3}$$

$$R_a = \frac{1}{A_t} \int_{x,z} |k - k_{avg}| dA, \tag{4.4}$$

$$k_{rms} = \sqrt{\frac{1}{A_t} \int_{x,z} (k - k_{avg})^2 dA}, \tag{4.5}$$

$$S_k = \frac{1}{A_t} \int_{x,z} (k - k_{avg})^3 dA \Big/ k_{rms}^3, \tag{4.6}$$

$$K_u = \frac{1}{A_t} \int_{x,z} (k - k_{avg})^4 dA \Big/ k_{rms}^4, \tag{4.7}$$

$$E_x = \frac{1}{A_t}\int_{x,z}\left|\frac{\partial k}{\partial x}\right|dA, \tag{4.8}$$

$$E_z = \frac{1}{A_t}\int_{x,z}\left|\frac{\partial k}{\partial z}\right|dA, \tag{4.9}$$

$$P_o = \frac{1}{A_t k_c}\int_0^{k_c} A_f dy, \tag{4.10}$$

$$I_x = tan^{-1}\left\{\frac{1}{2}S_k\left(\frac{\partial k}{\partial x}\right)\right\}, \tag{4.11}$$

$$I_z = tan^{-1}\left\{\frac{1}{2}S_k\left(\frac{\partial k}{\partial z}\right)\right\}, \tag{4.12}$$

where $k(x,z)$ is the roughness height distribution and $A_f(y)$ and A_t are the fluid and total planar areas. $S_k(\partial k/\partial x_i)$ is the skewness of $\partial k/\partial x_i$ distribution. In table 4.1, k_{avg}, k_c, k_{rms} and k_s are then normalized by the first-order moment of height fluctuations R_a and were incorporated in the ML algorithms in this form. All surfaces considered were in the ranges $k_c/\delta \leq 0.17$ and $R_a/\delta \leq 0.04$.

4.2.2 Simulation parameters

Direct numerical simulation was used to calculate the velocity and pressure fields in turbulent open-channel flows over 45 different rough surfaces and one smooth one, at a constant frictional Reynolds number $\mathrm{Re}_\tau = u_\tau\delta/\nu = 1000$, where u_τ is the friction velocity and δ is the channel half-height. In these simulations, the domain sizes were $(L_x, L_y, L_z) = (3, 1, 1)\delta$. The origin of the y axis was the elevation of the lowest trough for each rough surface. The number of grid points was $(n_x, n_y, n_z) = (400, 300, 160)$. A uniform mesh was used in the x and z directions, yielding grid sizes of $\Delta x^+ = 7.5$ and $\Delta z^+ = 6.3$, where + denotes normalization in wall units. For all cases, the mesh was stretched in the y direction with a hyperbolic tangent function, with the third grid point from the origin at $y^+ < 1$. For the rough-wall cases, at the roughness crest, $\Delta y/k_c \leq 0.017$,

with this ratio taking its highest value for Case C11. The maximum grid size was $\Delta y^+_{\max} = 9.5$ at the channel center line, where the Kolmogorov length scale $\eta^+ \approx 6$. Moin & Mahesh [116] have proposed that one requirement for obtaining reliable first- and second-order flow statistics is that the grid resolution be fine enough to capture accurately most of the dissipation, while Moser & Moin [60] noted that most of the dissipation in curved channel flow occurs at scales greater than 15η (based on average dissipation). It follows that for DNS computations of these kinds of flow statistics in channel and boundary-layer flows, $\Delta x/\eta$ and $\Delta z/\eta$ are typically chosen between 7 to 15, and 4 to 8 respectively (see, for example, [117], [118] and [44]). The grid sizes in this study were chosen accordingly and were: $\Delta x/\eta < 7.5$, $\Delta y/\eta < 4.0$, and $\Delta z/\eta < 6.5$.

Periodic boundary conditions were imposed in the streamwise and spanwise directions, with no-slip and symmetry boundary conditions at the bottom and top boundaries respectively. After each simulation had reached statistical stationarity, data were collected for ensemble averaging over 10 large-eddy turn-over times (δ/u_τ). In these simulations, the time step $\tau^+ \leq 0.04$ and so was significantly smaller than the largest acceptable one of $\tau^+ \approx 0.2$ recommended by Choi & Moin [119] for DNS.

The surface Taylor micro-scales $\lambda_{T,x}$ and $\lambda_{T,z}$, in the x and z directions, were used to evaluate the adequacy of the grid resolution for resolving details of flow in the roughness sublayer, following Yuan & Piomelli [52]. These geometric micro-scales were obtained by fitting a parabola to the two-point autocorrelation of the surface height fluctuation in the respective direction. They represent the size of an equivalent 'roughness element' in the context of random multiscale roughness. The streamwise and spanwise values of λ_T, rescaled by u_τ/ν as λ^+_T, and the respective grid sizes are given in table 4.2 (part I). For each case, λ^+_{T,x_i} is of order 10 to 10^2, indicating that the average size of the roughness element is large in viscous units. On average, roughness elements were well resolved by the grid, with typically 4 to 12 grid points per λ_{T,x_i} microscale in each direction. For reference purposes, Yuan & Piomelli [5] reported a resolution of $\lambda_{T,x}/\Delta x \approx 4$ in their large-eddy simulations of channel flow over surfaces with sand-grain roughness. The cases in table 4.2 for which λ_T was not well resolved in at least one direction ($\lambda_{T,x}/\Delta x < 3$ or $\lambda_{T,z}/\Delta z < 3$) may also

not have been fully-rough flows (as discussed in the following section), and so were not included in the ensemble of flows for ML training and testing.

In rough-wall flows, the pressure drag is caused primarily by the local flow structures and separation in the vicinity of individual roughness protuberances, which are predominately near-wall phenomena. To carry out the 46 separate DNS simulations for determining k_s efficiently, with sufficient near-wall resolution, a small-span channel simulation approach was employed. The concept of minimal-span simulation was introduced by Jiménez et al. [120]. Chung et al. [121] and MacDonald et al. [122] carried out analyses of the performance of DNS over small spanwise domains for full and open channel flows on rough and smooth walls and showed that minimal-span simulations captured the essential near-wall dynamics and yielded accurate computations of wall friction, and of mean velocities and Reynolds stresses as far from the wall as $y \approx 0.3\delta$, when the following constraints were met:

$$L_x \geq \max\left(1000\delta_\nu, 3L_z, \lambda_{r,x}\right), \tag{4.13a}$$

$$L_y \geq k_c/0.15, \tag{4.13b}$$

$$L_z \geq \max\left(100\delta_\nu, k_c/0.4, \lambda_{r,z}\right), \tag{4.13c}$$

where $\delta_\nu = \nu/u_\tau$ and λ_{r,x_i} is the characteristic roughness wavelength in the x_i direction. Alternatively, the surface Taylor microscale may be used as the lengthscale in this constraint. Conditions (4.13*a,c*) were satisfied by choosing domain sizes L_x^+ and L_z^+ of 3000 and 1000 respectively, while condition (4.13*b*) was met for all cases except C11, which fell below the $L_y \geq k_c/0.15$ constraint by about 10%. C11 is a case with random geometry; protuberances beyond 0.15δ exist but are rare.

The criteria of (4.13) were developed originally for simulations of flow over surfaces with uniformly distributed roughness elements. In this study, the random roughness geometries used require an additional criterion on the sufficiency of the domain size: the area $L_x L_z$ should be large enough to achieve statistical convergence of surface parameters, such as k_{rms} and E_{x_i}, and of the flow parameter k_s. To check the adequacy of the chosen domain size, an additional simulation was carried out of Case C21, the surface comprising the largest dominant spatial wavelength (and

	Part I				Part II	
Case name	$\lambda_{T,x}^+$	$\lambda_{T,x}/\Delta x$	$\lambda_{T,z}^+$	$\lambda_{T,z}/\Delta z$	d/δ	$\widehat{k}_s^+$
C01,r4,reg,inc1	19.7	2.6	21.1	3.4	0.032	19.4
C02,r4,reg,inc2	20.4	2.7	33.1	5.3	0.046	49.7
C03,r4,reg,inc3	19.8	2.6	22.9	3.7	0.033	31.0
C04,r6,reg,inc1	27.7	3.7	28.4	4.5	0.038	64.4
C05,r6,reg,inc2	31.6	4.2	39.1	6.2	0.057	124.4
C06,r6,reg,inc3	29.9	4.0	30.0	4.8	0.045	58.9
C07,r4,rnd,inc1	33.8	4.5	26.7	4.3	0.036	136.2
C08,r4,rnd,inc2	26.1	3.5	32.7	5.2	0.052	322.3
C09,r4,rnd,inc3	35.5	4.7	30.1	4.8	0.039	131.1
C10,r6,rnd,inc1	38.2	5.1	29.7	4.8	0.042	268.9
C11,r6,rnd,inc2	38.1	5.1	47.0	7.5	0.070	536.4
C12,r6,rnd,inc3	47.9	6.4	40.2	6.4	0.053	271.7
C13,r4,reg,por1	17.8	2.4	32.7	5.2	0.047	41.4
C14,r4,reg,por2	27.5	3.7	34.2	5.5	0.032	140.6
C15,r4,reg,por3	31.5	4.2	39.4	6.3	0.028	157.1
C16,r6,reg,por1	25.6	3.4	46.1	7.4	0.066	76.7
C17,r6,reg,por2	40.1	5.3	47.8	7.6	0.044	259.8
C18,r6,reg,por3	44.4	5.9	54.8	8.8	0.039	246.5
C19,r4,rnd,por1	32.7	4.4	31.1	5.0	0.042	158.2
C20,r4,rnd,por2	35.6	4.7	31.3	5.0	0.026	105.7
C21,r4,rnd,por3	37.4	5.0	34.2	5.5	0.027	102.7
C22,r6,rnd,por1	44.6	5.9	35.3	5.6	0.053	276.8
C23,r6,rnd,por2	47.1	6.3	39.7	6.4	0.038	175.1
C24,r6,rnd,por3	47.1	6.3	44.4	7.1	0.045	260.3
C25,r4,reg,ES1	89.0	11.9	–	–	0.024	25.6
C26,r4,reg,ES2	66.5	8.9	–	–	0.026	65.3
C27,r4,reg,ES3	27.1	3.6	–	–	0.035	45.5
C28,r6,reg,ES1	90.6	12.1	–	–	0.033	71.2
C29,r6,reg,ES2	66.8	8.9	–	–	0.040	112.0
C30,r6,reg,ES3	27.2	3.6	–	–	0.054	64.0
C31,r4,rnd,SGR	27.8	3.7	25.0	4.0	0.032	48.7
C32,r4,rnd,RND1	131.2	17.5	54.1	8.7	0.041	8.4
C33,r4,rnd,RND2	96.3	12.8	42.1	6.7	0.043	17.6
C34,r4,rnd,RND3	56.4	7.5	22.4	3.6	0.045	22.5
C35,r4,rnd,RND4	39.5	5.3	15.8	2.5	0.046	18.3
C36,r4,rnd,RND5	25.1	3.3	11.4	1.8	0.051	23.4
C37,r6,rnd,SGR	36.5	4.9	31.9	5.1	0.046	108.8
C38,r6,rnd,RND1	88.5	11.8	72.6	11.6	0.060	12.0
C39,r6,rnd,RND2	93.8	12.5	35.7	5.7	0.062	17.1
C40,r6,rnd,RND3	57.0	7.6	22.8	3.6	0.070	50.4
C41,r6,rnd,RND4	40.5	5.4	15.6	2.5	0.073	48.7
C42,r6,rnd,RND5	24.5	3.3	11.3	1.8	0.076	43.8
C43,SG	35.2	6.0	33.5	5.7	0.044	93.0
C44,TB	132.1	10.4	168.5	13.2	0.058	24.1
C45,CB	25.7	4.5	25.5	4.4	0.039	149.9
C46,r4,rnd,por3,FS	37.6	5.0	34.6	5.5	0.027	104.2

Table 4.2: Part I: Streamwise and spanwise values of the surface Taylor micro-scale λ_T. Part II: Flow-related parameters obtained from DNS. The flow is assumed fully rough if $\widehat{k}_s^+ \gtrsim 50$, in which case k_s is equal to $\widehat{k}_s$.

consequently the most limited sampling of random geometrical components with this wavelength) and a long-tailed height-fluctuation pdf with a kurtosis of around 8. In this validation simulation, denoted Case C46, the domain sizes were doubled in x and z, by duplicating C21 in these directions. The double-averaged velocity profiles $U^+ = \langle\overline{u}\rangle^+(y^+)$ for Cases C21 and C46 are in a very good agreement over the log-linear region, as shown in figure 4.2. Each surface statistic differs by no more than 3%, with the greatest discrepancy found in I_z, while the equivalent sandgrain roughness height k_s is almost equal in the two cases. The chosen domain size was therefore considered sufficient for accuracy and convergence of statistics describing flow over the random roughness geometries of this study.

4.3 Results

4.3.1 Post-processed results

In figure 4.2, the streamwise double-averaged velocity profiles computed in these simulations are shown. The profiles in the logarithmic region are described for the smooth-wall case and the fully-rough rough-wall cases as

$$\left\langle\overline{u}\right\rangle^+ = \frac{1}{\kappa}\ln(y^+) + 5.0, \text{ and} \tag{4.14a}$$

$$\left\langle\overline{u}\right\rangle^+ = \frac{1}{\kappa}\ln\left(\frac{y-d}{k_s}\right) + 8.5 \tag{4.14b}$$

respectively, where d is the zero-plane displacement, obtained as the location of the centroid of the wall-normal profile of the averaged drag force [62]. The shift in the y coordinate by d accounts for the flow blockage by surface roughness elements, and the values of d are given in table 4.2 (part II).

To determine whether a particular flow was within the fully rough regime, equation (4.14b) was applied to the computed logarithmic velocity profile to yield a test value of k_s, denoted as $\widehat{k}_s$ in table 4.2 (part II). With $\widehat{k}_s$ determined for all cases, those with $\widehat{k}_s^+$ greater than a threshold value of 50 were deemed to be in the fully rough regime (30 surfaces), in which case k_s was set to equal $\widehat{k}_s$. Those below the threshold were possibly transitionally rough (15 surfaces) and so were

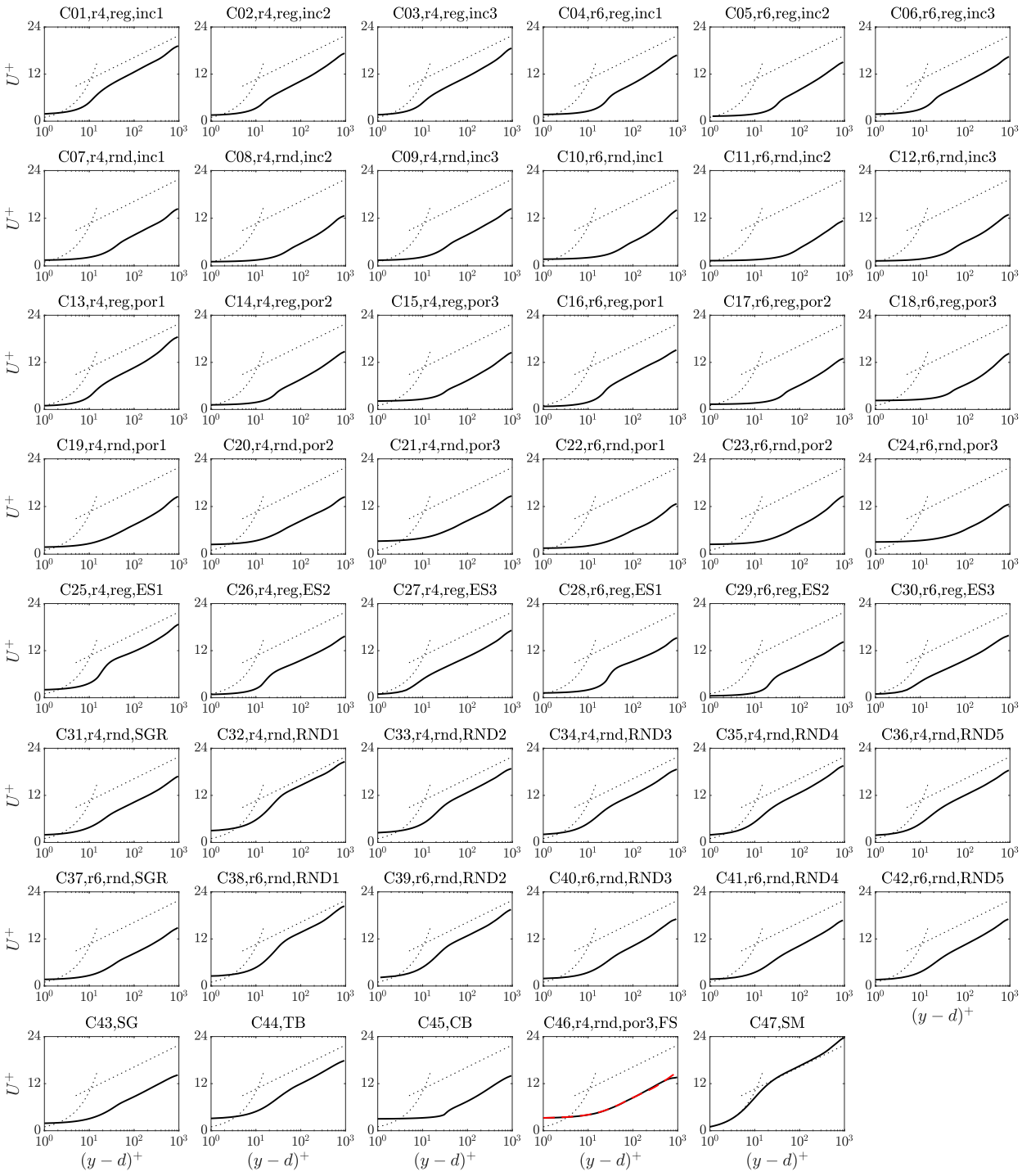

Figure 4.2: Profiles of streamwise double-averaged velocity plotted against a zero-plane-displacement shifted logarithmic y abscissa. The dashed lines are $u^+ = y^+$ and $u^+ = 2.5 \ln (y - d)^+ + 5.0$. The red dot-dash line in plot C46 is that of C21.

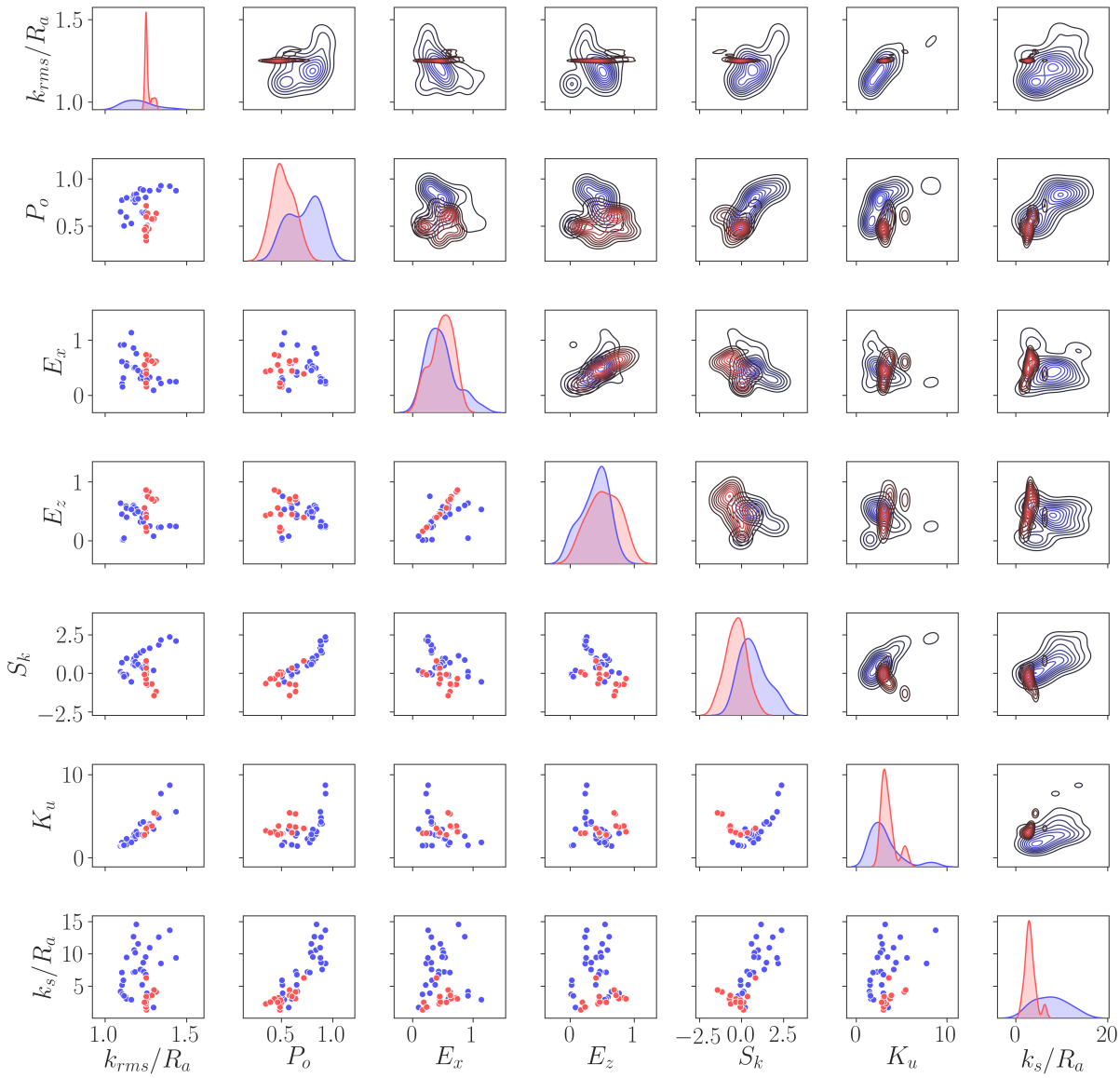

Figure 4.3: Pair plots of geometrical parameters and k_s, with k_s plots in the bottom row and the first column, DNS data (*blue*), experimental data (*red*).

not included in ML predictions in this study. The threshold value of k_s^+—the lower end of the fully rough regime—has been observed to vary significantly for different types of roughness and is typically between 20 and 80. For example, the threshold values for surfaces C43 and C44 are roughly 80 and 20 [5], and 50 for surface C45 [59].

The threshold value of k_s^+ which signifies the beginning of the fully rough regime was not determined more precisely because of the cost of carrying out, for each surface, simulations at successively higher values of k_s^+ until k_s/R_a became invariant with the Reynolds number. In the GPR prediction, potential uncertainties in k_s which might arise through treating all flows with $k_s^+ > 50$ as fully rough, and other sources of possible error, were compensated for by incorporating an assumed 10 % noise level in the learning stage of the prediction of k_s, as discussed in section 4.3.2. The values of $k_s^+ = 50$ as the threshold for fully rough flows and the assumed noise level were chosen as part of a trade-off to maximize the number of usable data, to avoid overfitting, while acknowledging possible uncertainties in the modeling data.

In figure 4.3, pair plots of the different topographic roughness parameters are shown as scatter plots (lower left), joint pdfs (upper right), and distribution pdfs (diagonal). Pair scatter plots for the true (DNS and experimental) value of k_s and other roughness parameters are along the bottom row of this figure. It can be seen that, for the roughness cases chosen, there is some correlation between kurtosis and rms roughness (column 1, row 6), kurtosis and skewness (column 5, row 6), and skewness and porosity (column 2, row 5). The relationship between others appears to be more random. From the graphs in the bottom row, it can be seen that k_s/R_a scales on porosity to some power, albeit with some scatter (column 2, row 7). It also appears that k_s/R_a might decrease with skewness for surfaces with $S_k < 0$ and increase with skewness in cases with $S_k > 0$ (column 5, row 7). Surfaces with positive skewness yielded higher values of k_s compared to those with negative skewness, consistent with the observation of Flack et al. [109]. Beyond these observations, there does not appear to be a clear linear correlation between k_s and any individual roughness parameter, which makes the search for a functional dependence of k_s on these parameters a problem well suited to ML. The measures of inclination, I_x and I_z, showed no clear correlation with other variables or

with k_s/Ra.

4.3.2 ML predictions of the equivalent sand-grain height

The ML techniques of DNN and GPR were employed to predict k_s from the data sets described in the previous section. The objectives of this exercise were to generate and collect data, and make qualitative comparisons between ML predictions and those from conventional correlations, rather than evaluating and comparing the performance of various ML procedures per se. DNN and GPR approaches were used because our experience was that they predicted k_s with high accuracy, notwithstanding their simplicity. Other approaches such as the Support Vector Machine (SVM) technique were considered initially, but their preliminary predictions were not as accurate as those found using DNN and GPR approaches.

The main characteristics of DNN and GPR methods are described below:

- The inputs for both techniques were 17 roughness geometrical parameters, 8 of which were the primary variables k_{rms}/R_a, I_x, $|I_z|$, P_o, E_x, E_z, S_k and K_u (defined in equations 4.3 to 4.12). The other 9 were products of the primary variables, which were added to improve the efficiency of each learning stage. They were $p_1 = E_x Ez$, $p_2 = E_x S_k$, $p_3 = E_x K_u$, $p_4 = E_z S_k$, $p_5 = E_z K_u$, $p_6 = S_k K_u$, $p_7 = E_x^2$, $p_8 = E_z^2$ and $p_9 = S_k^2$. These particular products were chosen because of their perceived importance for certain types of roughness.

- The database consisted of 45 different sets: 30 DNS of turbulent channel flows over different surfaces at $\mathrm{Re}_\tau = 1000$, and 15 experimental data sets at higher Reynolds numbers, with all data sets in the fully-rough turbulent-flow regime.

- The DNN architecture was a *Multi Layer Perceptron*, with three hidden layers (with 18, 7 and 7 neurons respectively). The activation functions at all nodes were of the *Rectified Linear Unit* kind, and kernel regularization was used to avoid overfitting. The network had 521 trainable weights in total. The preset parameters to the algorithm were optimized based on available data, through a *hyper-parameter tuning* process. Specifically, 270 configurations were first

generated with different lengths (representing the number of layers) and widths (representing the number of neurons). For each configuration, the DNN compiler was performed 1000 times with random selections of training (70% of total) and testing (30% of total) datasets to identify the best performance of the configuration. The configuration that yielded the best results was considered as the optimal one, the results of which are presented here. The cost of data fitting for one iteration (out of 1000) for each DNN configuration was about one second. In total, it took about 75 hours to obtain the optimal DNN network. This architecture was found to provide suitable accuracy in modeling without overfitting, for this particular multivariate labeled regression problem.

- The GPR procedure used *Rational Quadratic* kernels to represent k_s as a superposition of scaled Gaussian functions of the independent variables of the modeling problem. Similar to the DNN method, the training and testing data were chosen randomly, with respective ratios of 70% and 30% of the total data points. The preset parameters (e.g. kernel type, number of iterations, etc.) were also tuned with the available data by running the GPR compiler for about 8000 times. It took about 35 hours to obtain the optimal fit. The GPR method has the capability of incorporating uncertainty or noise in the determination of model parameters in the learning stages. Such noise might arise through: numerical and discretization errors; uncertainty in the form and model coefficients of equation (4.1); the applicability and fitting range of equation (4.1) (which was deduced from high Reynolds number experiments) to simulations at much lower Reynolds numbers; and the possibility that some of the training data may have been from simulations in which the flow was not quite fully rough. A noise level of 10% in k_s/R_a values was chosen as an upper estimate of the likely uncertainty from these sources. Noise levels of 5% and 15% were also tested, but little sensitivity of the k_s prediction was found to the assumed noise level within the tested range.

The values of k_s predicted from the surface topography parameters, henceforth called k_{sp}, are compared to the actual k_s values in figure 4.4, for the DNN and GPR methods respectively. Scatter

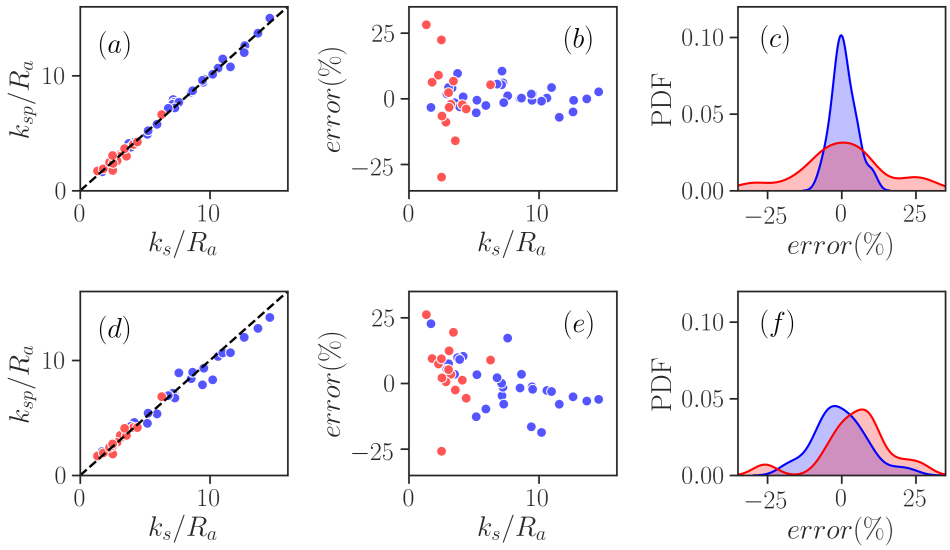

Figure 4.4: (a,d) Scatter plot of true k_s and predicted k_s, (b,e) scatter plot of true k_s and relative error, (c,f) pdfs of relative error for (a-c) DNN and (d-f) GPR predictions, with DNS data (*blue*), experimental data (*red*).

plots of k_{sp} and the true value of k_s in figures 4.4(a) and (d) reveal a tight clustering of data along the $y = x$ diagonal, with only a few outlying points. This very high degree of correlation between k_{sp} and k_s implies that both techniques have been applied with equal success to this prediction problem. The error range, figures 4.4(b) and (e), is less than ±30% (L_∞ norm) and the average error (L_1 norm) is less than 8%, for both techniques.

The consistency between both the k_s predictions and error bands for two quite different ML techniques suggests that they are both well-suited to this kind of problem, and possibly close to an optimum for this class of ML approach.

The error values as percentages, for the DNN and GPR methods, are given in table 4.3, together with the error in the empirical relation

$$k_s = 2.91 k_{rms}(2 + S_k)^{-0.284}, \tag{4.15}$$

proposed by Flack et al. [113], and

$$k_s = 1.07 k_t(1 - e^{-3.5Ex})(0.67S_k^2 + 0.93S_k + 1.3), \tag{4.16}$$

given by Forooghi et al. [115], as well as their respective recalibrated correlations:

$$k_s = 1.11 k_{rms}(2 + S_k)^{0.74}, \tag{4.17}$$

$$k_s = 0.04 k_t (1 - e^{-5.50 E_x})(S_k^2 + 2.57 S_k + 9.82). \tag{4.18}$$

when extended to all cases in the current database. It is interesting to note that the form of equation (4.15) was chosen for surfaces generated by grit blasting—closely-packed, random, three-dimensional roughnesses with a wide range of scales (E01-E06), while many of the simulated surfaces are two-dimensional, some are characterized by discrete elements of similar sizes, while others are sparse or wavy (characterized by low slopes). Equation (4.16), on the other hand, includes a slope parameter and was calibrated for numerically generated surfaces consisting elements of random sizes and a prescribed shape.

For most cases, the errors from the DNN and GPR methods were of the same order of magnitude and much smaller than the error in using equation (4.15) or (4.16). In the DNN and GPR predictions of simulation cases, the greatest errors (about 25%-30%) arose in cases E07 and E08. The surfaces associated with these cases are characterized by fractal features (with spectral slopes of -0.5 and -1.0, respectively [114]). The size of the errors for these cases might be attributed to the small number of surfaces with this feature used in the training set (as opposed to the many surfaces that are mostly characterized by single-scale elements). A close examination of the prediction errors for the DNS cases showed a subtle trend between relatively high errors and low roughness solidity (or low E_s and insignificant wake sheltering), in, for example, cases C28 and C44. Both these cases are characterized by large-wavelength, wavy features, suggesting an under-representation of sparse roughness in the dataset. Beyond this observation, no clear correlation was found between the error and other primary roughness parameters included herein or surface categorizations (2D/3D, random/regular).

The errors associated with using equation (4.15) are small for surfaces E01 through E06, which were used to calibrate this relation. The errors in using equations (4.15) and (4.16) over all surfaces

Case name	err_{DNN}	err_{GPR}	err_{B1}	err_{B2}	err_{B3}	err_{B4}
C04,r6,reg,inc1	4.0	4.1	-16.7	-40.9	8.6	-63.9
C05,r6,reg,inc2	0.7	10.3	-38.3	-49.5	2.0	-71.7
C06,r6,reg,inc3	4.2	7.5	-10.4	-33.6	24.5	-59.8
C07,r4,rnd,inc1	10.5	-4.7	-63.5	-63.6	10.0	-73.5
C08,r4,rnd,inc2	-0.6	-4.8	-80.1	-77.6	-4.1	-81.7
C09,r4,rnd,inc3	6.0	-1.5	-63.4	-64.2	8.3	-73.4
C10,r6,rnd,inc1	0.2	-2.7	-76.3	-72.5	11.8	-77.8
C11,r6,rnd,inc2	2.6	-6.1	-82.9	-78.9	4.1	-82.2
C12,r6,rnd,inc3	-1.0	-18.7	-74.7	-72.7	-2.3	-78.7
C14,r4,reg,por2	5.3	0.0	-66.2	-64.2	-8.7	-80.3
C15,r4,reg,por3	4.2	-3.1	-76.7	-66.5	29.0	-78.8
C16,r6,reg,por1	1.8	5.4	3.5	-41.7	21.5	-59.4
C17,r6,reg,por2	-0.6	-1.3	-74.5	-70.3	-10.9	-82.7
C18,r6,reg,por3	-5.1	-5.1	-79.1	-68.4	35.5	-78.8
C19,r4,rnd,por1	1.8	-2.3	-71.4	-69.4	44.9	-67.8
C20,r4,rnd,por2	1.1	17.2	-67.0	-56.6	82.1	-66.3
C21,r4,rnd,por3	0.0	-1.8	-69.6	-50.0	254.1	-46.2
C22,r6,rnd,por1	-7.1	-7.9	-77.0	-76.7	-10.6	-78.4
C23,r6,rnd,por2	0.2	3.4	-70.9	-60.4	80.8	-67.9
C24,r6,rnd,por3	-0.1	-6.7	-80.5	-66.3	136.7	-66.5
C26,r4,reg,ES2	-5.4	-12.7	-48.6	-61.6	-57.6	-83.8
C28,r6,reg,ES1	9.6	9.8	-29.2	-45.9	-51.9	-81.2
C29,r6,reg,ES2	-2.6	-9.8	-54.7	-66.2	-53.2	-83.2
C30,r6,reg,ES3	-1.5	3.4	-21.8	-45.7	8.1	-65.7
C31,r4,rnd,SGR	-0.6	3.3	-46.7	-50.7	65.1	-53.8
C37,r6,rnd,SGR	-1.5	-7.9	-61.3	-65.0	11.9	-68.6
C40,r6,rnd,RND3	-3.1	9.1	-23.6	-39.6	98.3	-30.8
C43,SG	5.5	2.1	-58.6	-60.1	46.3	-62.0
C44,TB	-3.3	22.7	77.6	51.9	31.5	-51.6
C45,CB	1.8	-16.5	-70.4	-52.0	79.3	-72.8
E01,16,2	-2.1	3.5	6.2	-47.5	370.2	63.0
E02,16,3	2.3	5.2	3.3	-33.7	429.4	79.5
E03,16,7	-2.3	1.2	-2.2	-69.1	368.1	38.6
E04,16,8	-3.9	-5.7	1.3	-78.8	412.4	27.6
E05,16,9	-3.3	12.4	10.9	-46.3	262.1	27.3
E06,16,15	-16.0	-2.5	-3.0	-51.1	405.4	79.9
E07,18,1	-29.8	-25.8	17.3	-4.0	208.3	11.2
E08,18,2	28.1	26.1	120.7	79.4	388.8	80.0
E09,19,1	6.2	9.4	69.2	25.9	312.5	56.9
E10,19,2	-8.9	0.6	5.8	-20.7	258.9	20.6
E11,19,3	8.9	7.4	47.4	-24.1	247.4	32.2
E12,19,4	-6.6	2.1	24.1	-21.0	258.4	32.2
E13,19,5	6.7	19.4	-16.6	-23.8	287.2	6.6
E14,19,6	5.3	8.9	-56.8	-52.5	177.2	-38.2
E15,19,7	22.3	9.4	19.8	-10.2	342.6	43.0
L_1	5.4	7.8	47.6	52.8	133.8	60.6
L_∞	29.8	26.1	120.7	79.4	429.4	83.8

Table 4.3: Errors in k_s prediction by DNN and GPR compared to errors of the empirical correlations: err_{B1} (equation 4.15), err_{B2} (equation 4.17), err_{B3} (equation 4.16) and err_{B4} (equation 4.18). The four largest errors (in magnitude) for each column are colored in red. The errors are percentages.

in the database are 120% and 430% respectively. However, when recalibrated against the full database, equations (4.17) and (4.18) have a significantly smaller error band with maximum values of 79% and 84%. The high error values of the empirical correlations, compared to DNN or GPR prediction, are attributed to the small number of geometrical variables used in their calibrations and the restricted range of the models' parameters.

4.3.3 Uncertainty estimation

In addition to predictions of equivalent sand-grain height, the GPR method provides confidence margins as functions of each input parameter. These margins can be useful for indicating the kinds of surfaces for which additional training data could improve confidence in predictions. This feature of the GPR approach makes it very attractive for studies of this kind, since DNS and experimental generation of data can be expensive.

The confidence intervals determined by the GPR technique are shown as functions of the normalized surface rms roughness height, effective slope, porosity and skewness in figure 4.5. Wider intervals indicate higher estimated values of predictive error, such as at roughness porosity of 0.68, and skewnesses of -1.5 and 2.0. Surfaces of roughness with similar values of porosity and skewness would then be priorities for additional simulations or experiments.

4.3.4 Sensitivity analysis

The dependence of DNN predictions of k_s on individual roughness parameters is explored by determining the change in the error norms when each of the primary surface parameters is removed from the data from which the DNN prediction was made. In table 4.4, the actual error for each surface, and the values of the L_1 and L_∞ norms of errors in the prediction of k_s over the 45 surfaces, are reported when the parameter(s) in the first row is (are) the excluded one(s). The errors of the base prediction (which includes all 8 primary parameters) are listed in the second column. In the following discussion, we focus on the L_1 norm for ease of comparison over all 45 cases.

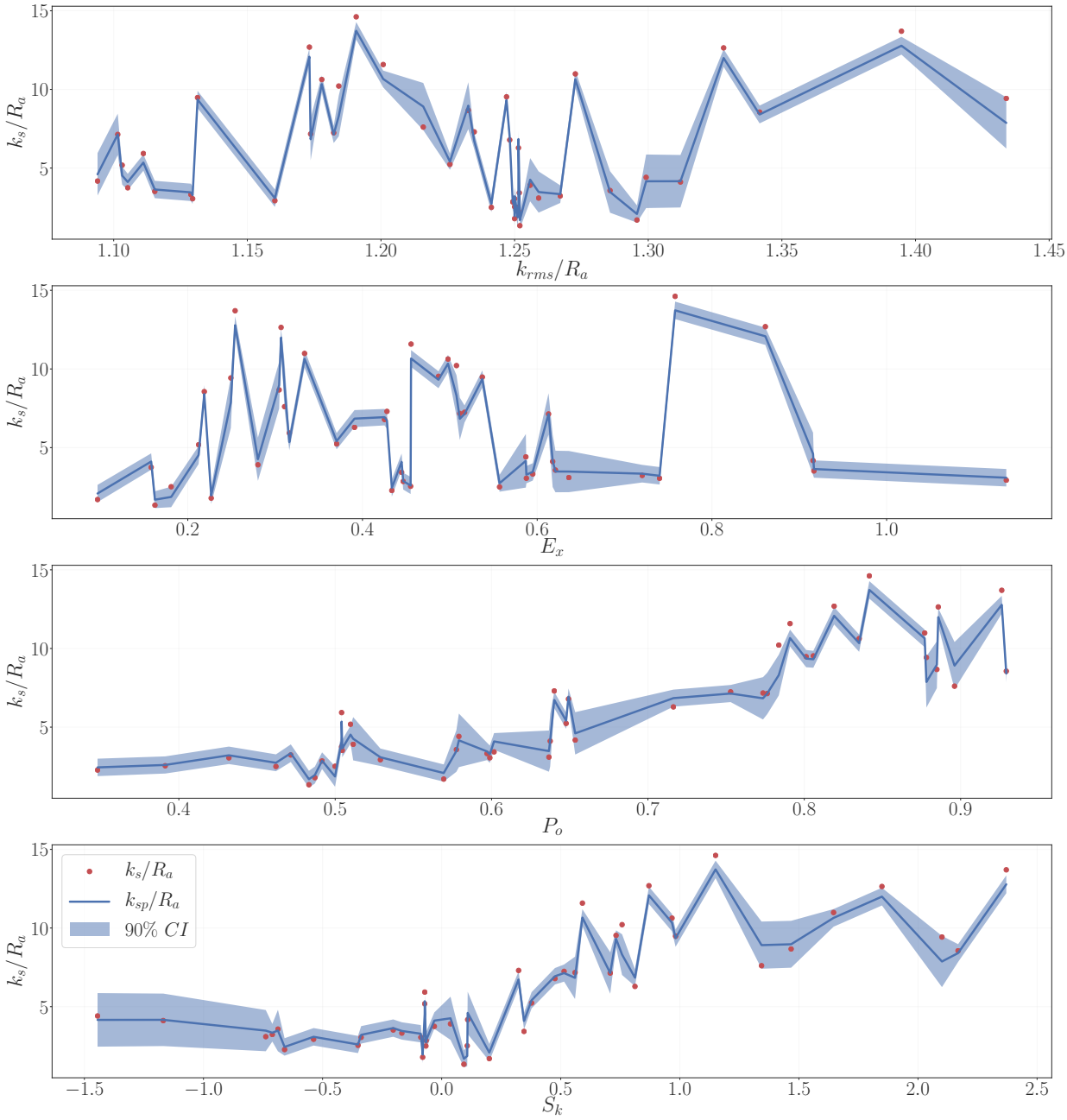

Figure 4.5: Confidence interval (CI) of predictions with the GPR method, with predicted values of k_s/R_a in *blue lines* (called k_{sp}) and true values of k_s/R_a in *red dots*. GPR predictions for both training and testing data sets are shown — k_s and k_{sp} are very close to each other for the training data points, while they deviate (less than 30% of error) for some test data points. Line jaggedness is associated with projection of a high-dimensional space to one-dimensional ones.

When the values of L_1 are considered, the relative importance of these surface parameters for predicting k_s is: E_x, I_x, $|I_z|$, E_z, P_o, k_{rms}/R_a, S_k, and of least importance, K_u. The L_1-norm error is small when all parameters are included (7.4%). Excluding any single one of these parameters increases the L_1-norm error up to around 9%. On the other hand, the exclusion of K_u from the input parameters does not worsen predictions of k_s significantly. Instead, this observation appears to be a consequence of correlation between K_u and other surface parameters like k_{rms}/R_a (see figure 4.3). When such correlations exist and one correlating parameter is excluded, the DNN process redistributes the weightings given to other correlated parameters, with little loss in predictive accuracy.

To reduce the correlation between the excluded parameters and the remaining ones, one may exclude groups of parameters that are thought to characterize the same type of surface feature. For this reason, a sensitivity analysis was carried out on the effect of groups of variables on prediction of k_s. The characteristics of surface slope, element inclination angle, porosity, and intensity of height fluctuations, are contained in pairs of (E_x, E_z), (I_x, I_z), (P_o, S_k) and (k_{rms}, K_u), respectively. Parameters within each pair have been shown to be correlated to some degree in figure 4.3. Table 4.4 shows how the accuracy of k_s prediction is affected, if any one of these pairs is excluded. According to the table, the prediction of k_s is sensitive to all four pairs, but with greater sensitivities to the surface porosity (described by P_o, S_k) and the surface slope (described by E_x and E_z). As expected, the elimination of both parameters of a pair worsens the prediction more than removing either single parameter (from around 7-9% errors to up to 14%).

According to the sensitivity analysis, all parameters considered are of some importance in the prediction of k_s. The effective x-slope E_x and roughness height skewness S_k have been suggested as especially significant in earlier studies [37, 38, 5]. The inclination angle in the streamwise direction I_x makes a significant contribution to the k_s prediction because, physically, I_x characterizes the average aerodynamic shape of the roughness elements. Surfaces with $I_x > 0$ are aerodynamically bluff bodies when compared with surfaces of the same size but with $I_x = 0$, and surfaces with $I_x < 0$ tend to be more streamlined and hence produce less drag.

	None	Ex	Ez	Ex, Ez	krms	Ku	krms, Ku	Sk	Po	Sk, Po	Ix	Iz	Ix, Iz
C04	2	-2	3	-1	-1	-2	15	-1	3	13	-12	0	-3
C05	5	-8	11	6	3	-22	-4	0	8	-4	-6	-2	-11
C06	0	10	-1	1	0	10	2	5	1	5	18	6	8
C07	1	3	-1	2	10	-23	0	1	-6	-1	13	1	9
C08	-15	-14	-1	-4	-19	-24	-19	-2	-23	-36	-4	-7	-9
C09	18	4	6	3	0	3	6	1	-2	6	5	11	8
C10	0	1	-16	1	-14	0	-1	-12	2	-13	15	0	11
C11	-12	-3	-3	-23	-2	-2	-5	-12	-1	-29	1	-2	-2
C12	0	-4	-4	0	-18	-3	-4	-1	-7	-2	-3	0	-2
C14	0	4	5	5	1	5	26	3	8	-6	3	6	0
C15	16	5	0	0	2	9	0	0	-11	-2	4	-5	4
C16	1	-2	-1	24	-2	-2	-3	3	-2	6	6	-1	14
C17	-4	8	17	17	1	4	8	15	13	-4	3	5	3
C18	-1	-6	-10	-11	-2	-3	-11	-3	-21	-17	-10	-25	-16
C19	-10	-15	-11	-12	-3	4	5	6	-4	-11	-1	-2	-11
C20	1	3	3	4	3	3	2	4	3	0	23	25	13
C21	9	2	1	3	1	1	2	-1	0	0	0	8	14
C22	-3	-3	-8	-9	-2	-6	-8	-3	-8	-9	-9	-20	-12
C23	0	-2	-1	0	0	-5	-17	-1	0	-1	2	-3	2
C24	0	-21	-1	-1	-1	1	0	0	0	4	0	-4	-7
C26	-6	-17	-12	-9	-8	-5	-19	-15	-13	-5	-13	-14	-10
C28	18	19	21	26	17	18	-3	16	16	32	21	14	20
C29	-9	-19	-8	-22	-6	-5	-13	-25	-11	-22	-18	-17	-19
C30	-4	6	11	25	-10	0	6	24	0	-8	2	6	5
C31	22	20	8	19	24	0	-2	18	-1	-14	9	-1	9
C37	-2	-8	-7	-3	10	-4	-5	-1	-5	-1	-9	-8	-12
C40	-3	-6	-27	-21	-6	-5	-7	0	-1	2	-10	-8	-18
C43	3	-4	-4	6	16	1	2	0	7	23	-15	-1	-12
C44	-6	15	1	17	13	1	4	20	-6	-12	-2	-16	-21
C45	1	2	1	-4	-6	5	-1	-11	1	1	5	2	9
E01	12	4	4	-9	2	-3	-11	5	11	-10	1	-3	-3
E02	-13	6	-6	-7	-2	12	1	-2	10	-9	13	7	-2
E03	15	-6	0	-5	4	-6	-4	3	7	-32	2	1	2
E04	0	-15	-9	-9	-2	-6	-6	-3	-5	2	-2	4	0
E05	5	17	5	17	4	9	9	7	5	28	8	5	13
E06	-5	-3	-6	-3	-10	-9	-10	-6	-7	-9	-10	-10	-5
E07	-21	-21	-24	-18	-16	-21	-18	-17	-23	-41	-25	-25	-24
E08	22	22	25	22	19	18	25	24	7	24	21	22	24
E09	5	-3	15	27	-1	22	26	21	-2	-21	-3	2	2
E10	-18	-19	-5	-8	-25	-4	-5	1	-14	38	-14	8	-2
E11	-1	-15	-23	-19	-7	16	12	-2	9	29	0	-5	0
E12	-9	-3	6	0	-10	2	-2	-15	-10	28	-15	-22	-4
E13	11	8	17	6	17	2	8	7	21	-15	14	25	15
E14	22	6	1	0	6	4	2	1	25	33	9	5	-5
E15	0	18	18	-4	11	9	15	11	19	32	19	23	16
L_1	7.4	8.9	8.2	9.7	7.6	7.1	7.9	7.3	8.0	14.2	8.8	8.6	9.1
L_∞	22	22	27	27	25	24	26	25	25	41	25	25	24

Table 4.4: Errors in k_s prediction by excluding one or two features. The base prediction includes all primary variables. The four largest errors (in magnitude) for each column are colored in red. The errors are percentages.

An important finding from this study is that the effective z-slope E_z is of similar importance to accurate k_s prediction as S_k or E_x. The exclusion of E_z adversely affects the prediction for a large number of rough surfaces. Physically, E_z describes whether the surface is close to a two-dimensional (2D) roughness with $E_z = 0$ (such as a transverse bar roughness) or a three-dimensional (3D) roughness with finite E_z. It is known that a k-type 2D roughness produces a higher drag than a 3D roughness with the same height due to the larger spanwise lengthscale that the 2D roughness imparts to the flow [123].

4.3.5 Comparison between ML algorithms and polynomial models

Explicit algebraic data representations, such as polynomial functions, can also be determined for the data sets of this study, using fitting or minimization procedures. In such methods, a set of basis functions is proposed for a model, the unknown coefficients of which are then optimized according to specified constraints. They are a generalization of the models of equation (4.2), which were based on experimental observations of the dependence of k_s on a small number of surface parameters. A 30-degree-freedom polynomial basis was proposed as a 'white-box' model for k_s, analogous to a low-order Taylor series expansion for k_s:

$$\begin{aligned} k_s/R_a = \alpha_0 &+ \alpha_1(k_{rms}/R_a)^{\alpha 2} + \alpha_3 I_x + \alpha_4|I_x|^{\alpha 5} + \alpha_6|I_z| + \alpha_7|I_z|^{\alpha 8} + \\ &\alpha_9 P_o^{\alpha 10} + \alpha_{11} E_x^{\alpha 12} + \alpha_{13} E_z^{\alpha 14} + \alpha_{15} S_k + \alpha_{16}|S_k|^{\alpha 17} + \\ &\alpha_{18}(K_u - 3) + \alpha_{19}|K_u - 3|^{\alpha 20} + \alpha_{21}(k_{rms}/R_a)^{\alpha 22} P_o^{\alpha 23} + \\ &\alpha_{24}(k_{rms}/R_a)^{\alpha 25} E_z^{\alpha 26} + \alpha_{27} P_o^{\alpha 28} E_z^{\alpha 29}, \end{aligned} \tag{4.19}$$

where a_i ($i = 0, 1, \cdots, 29$) are the model coefficients. To keep this model as simple as possible and to bring the effects of all contributing factors into account, we used terms as $\alpha_i \theta^{\alpha j}$ for a test variable θ that take only positive values (e.g. k_{rms}), and terms as $\alpha_i \theta + \alpha_j |\theta|^{\alpha k}$ for those variables that take both positive and negative values (e.g. S_k). For the latter, the power of θ in the first term is fixed (at one) instead of fitted, to eliminate the possibility of an imaginary number. Combinations of six parameters (E_x, E_z, P_o, S_k, k_{rms}/Ra and K_u), taken in pairs, were also included. Since, for

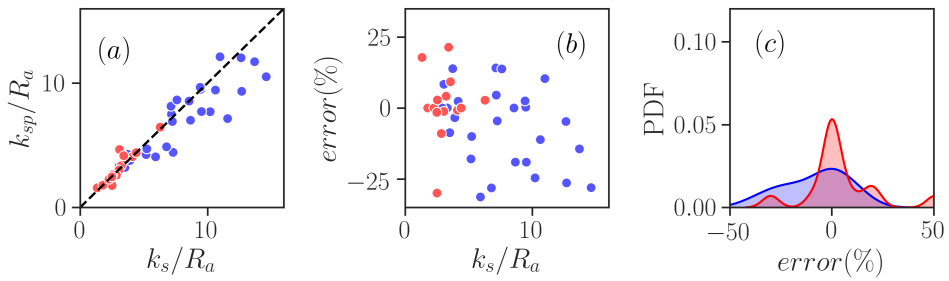

Figure 4.6: (a) Scatter plot of true k_s and predicted k_s (denoted as k_{sp}), (b) scatter plot of true k_s and relative error and (c) pdf of relative error distribution for prediction using polynomial function defined in equation (4.19), with DNS data (*blue*) and experimental data (*red*).

the present collection of surfaces, strong correlations were observed between individual variables within the three pairs of (E_x, E_z), (P_o, S_k) and (k_{rms}/Ra, K_u), shown in figure 4.3, only one variable from each pair was used for the combination terms in equation (4.19). Using the other variable from any of these pairs instead would not lead to a significant change in the prediction using equation (4.19).

The high-dimensional space of a_i is poorly suited to curve-fitting and minimization procedures which use stochastic gradient descent algorithms. However, it is well suited to robust minimization methods like the differential evolution algorithm [124], with which global minima can often be found efficiently in spaces of high dimension. In this case, it is used to determine the values of the coefficients a_i which minimize the L_1 norm.

In figure 4.6, the prediction quality of this white-box model with optimized coefficient values is shown. This method yields an average prediction error of 12% and a maximum one of 51% when using all 45 fully-rough data sets (to give the best possible prediction accuracy) for the model training.

The optimized values of a_i's are

α_0 = 5.312, α_1 = -1.172, α_2 = 4.264, α_3 = 0.050, α_4 = -1.283, α_5 = 8.393,
α_6 = -0.347, α_7 = -5.771, α_8 = 1.785, α_9 = 7.919, α_{10} = 4.058, α_{11} = -0.979,
α_{12} = 3.414, α_{13} = 6.380, α_{14} = 1.354, α_{15} = 1.023, α_{16} = 2.969, α_{17} = 1.273,
α_{18} = -0.946, α_{19} = -0.762, α_{20} = 0.056, α_{21} = 1.647, α_{22} = -8.176, α_{23} = 3.523,
α_{24} = -9.472, α_{25} = -5.656, α_{26} = 0.580, α_{27} = -5.425, α_{28} = 0.283, α_{29} = 7.177.

The predictive accuracy of this optimized explicit model equation is considerably lower than that of the DNN and GPR methods. One reason for this reduced accuracy is that low-order functions of geometrical parameters do not faithfully represent the dependence of k_s on surface parameters because each coefficient in the model is required to take the same value over the entire surface-parameter space. In ML approaches, such restrictions need not apply as they are not constrained to low-order polynomial functions but instead adopt a methodical search for the best representation of k_s as a function of the surface parameters. This search is carried out through 'feature selection' in the first layers of DNN and the properties of the basis functions adopted in GPR, each of which are designed to yield the same mean and standard deviation of k_s/R_a as in the original dataset [111].

4.4 Concluding remarks

The construction of a predictive model from a large ensemble of dataset for the equivalent sandgrain height k_s of a surface of arbitrary roughness, as a function of many different measures of surface topography, is a labeled regression problem that is well-suited to machine learning techniques. In this chapter, data from 45 different rough surfaces (in fully rough flows) were used to devise DNN and GPR predictions for k_s as functions of 8 different surface-roughness parameters.

Both models were able to predict k_s for the 45 surfaces with an average error below 10%, with the largest error for any one surface less than 30%. These predictions were significantly better than those of existing formulas, and of a 30 degree-of-freedom polynomial model fitted to the same data, where the greatest error for any surface was about 50%.

Sensitivity analyses revealed that inclusion of nearly all the surface roughness descriptive parameters was necessary to minimize the average prediction error, but that exclusion of either

measures of porosity or measures of the surface slope increased the maximum prediction error more significantly than omitting other parameters.

Machine learning techniques are well suited to this modeling problem because: *i*) it is complex insofar as different kinds of surface roughness yield different flow phenomena which are modeled most accurately in different ways, making the prospect of a general physical model very remote; and *ii*) the dependent surface-roughness variables upon which k_s is modeled are a large non-orthogonal set for which robust multivariable regression techniques are required. As machine learning methods, they take no account of physical modeling concepts or observed phenomena within roughness sublayers, such as recirculation regions, enhanced turbulence production in the wake of roughness elements, assumed scalings for drag *etc.*, each of which is applicable to flows over some rough surfaces but not others. Nor are they hindered by the lack of orthogonality of the surface roughness parameters as the dependent variables of k_s. The techniques used can be configured readily to mimic models with very many degrees of freedom and, when compared to polynomial models, their feature selection properties provide the equivalent of different values for polynomial coefficients in different regions of the surface-parameter space. In this application, both approaches of DNN and GPR yielded models with very similar predictive accuracy, even though the techniques themselves were very different. We therefore conclude that they yield high-fidelity predictions of the equivalent sand-grain roughness height for turbulent flows over a wide range of rough surfaces, as a significant improvement over other methods. Improved prediction might be achieved by enlarging the database to include rough-wall flows with surface parameters which correspond to the relatively low prediction confidence in the GPR method, and by including additional roughness parameters as inputs which might describe sparseness and two-dimensionality, such as the solidity, correlation lengthscales and other two-point surface statistics.

In addition to the k_s prediction described here, the DNS database and the ML techniques in general can also be used to uncover relations between roughness geometry and physics-related quantities, such as the flow pattern around roughness protuberances, flow separation locations, characteristics of the shear layers associated with the separation bubbles, the wake sheltering

volume, *etc*. Specifically, a ML network trained to correlate these flow characteristics (as outputs) to the roughness geometry (as inputs) may be an efficient tool for determining the sets of roughness geometrical features which are important for characterizing these effects. Knowledge of such a set of significant roughness parameters may also guide the construction of rough-surface databases that yield more efficient and more widely applicable predictions of k_s or other quantities.

4.5 Supplementary materials

The rough-wall flow database (including k_s, surface height map and surface parameters) and the trained DNN and GPR networks, called Prediction of the Roughness Equivalent Sandgrain Height (PRESH), can be accessed online in my GitHub repository at
https://github.com/MostafaAghaei/Prediction-of-the-roughness-equivalent-sandgrain-height.
With this package of data and programs, interested researchers can: i) use the ML networks described in this chapter to make predictions of k_s for surfaces of their own roughness topography; ii) download the code and train new DNN and GPR networks to predict k_s for a different set of surfaces of arbitrary topography; and iii) use the database of 45 rough-wall flows for other applications. It is recommended to use the ML configurations described in this chapter for surfaces with parameters inside the ranges specified in figure 4.3. Extrapolations (using inputs which are beyond the specified range) will lead to additional uncertainty.

CHAPTER 5

COMPRESSIBLE FLOWS OVER ROUGH WALLS

5.1 Introduction

The effects of wall roughness on physics, control, and modeling of compressible flows (subsonic, sonic, super- and hypersonic) are not well understood today. In high speed flow studies, roughness is typically an *isolated* (e.g. steps, joints, gaps, etc.), or a *distributed* (e.g. screw threads, surface finishing, and ablation) effect. The main effects of roughness on supersonic flight vehicles are primarily to increase the drag coefficient and secondarily to advance boundary-layer transition to turbulence (*early transition*), which increases the heat transfer coefficient. An understanding of these effects is important for flight control and thermal management (through thermal coatings), especially for reentry applications and reusable launch vehicles. Reda [125] and Schneider [32] have reviewed the effects of roughness on boundary layer transition, based on experimental wind-tunnel and in-flight test data of flows in supersonic and hypersonic conditions. Radeztsky et al. [126] analyzed the effects of roughness of a characteristic size of 1-μm (a typical surface finish) on transitions in swept-wing flows, and Latin et al. [127] investigated effects of roughness on supersonic boundary layers using rough surfaces with $k_s = O(1mm)$ ($100 < k_s^+ < 600$) and $Re_\tau \approx 40000$. Experimental studies of distributed roughness effects on compressible flows, boundary layer transition, and heat transfer include those of [128, 129, 130] and [131].

Most numerical studies have focused on isolated roughness [see e.g. 132] or ideal distributed roughness such as wavy walls [see e.g. 133], due to the simplicity in mesh generation and numerical procedures. However, complex distributed roughness is of primary importance and more relevant to flight vehicles, since in high-speed flows "even the most well-controlled surface will appear rough as the viscous scale becomes sufficiently small" [134]. Also, according to Schneider [32],"real vehicles often develop surface roughness in flight which is not present before launch." This flight-induced roughness may be discrete steps and gaps on surfaces from thermal expansion, or

distributed roughness induced by ablation or the impact of dust, water, or ice droplets. Studies of this kind demonstrate the need for a compressible solver that can handle complex distributed rough surfaces.

5.1.1 Literature review on immersed boundary (IB) methods

A thorough review on different IB methods is given in [135]. Irrespective of the compressibility effects, IB methods can be divided in different categories, the most important of which are:

1. Continuous forcing approach [penalty IB method of reference 136, among many others], where effects of solid boundaries are accounted for inserting an additional force term in the NS equations. This method is well suited for elastic boundaries, and rigid bodies [if a feedback forcing is provided, see e.g. 137]. Solid boundaries are captured diffusively in this approach, and the method requires a Lagrangian grid for deformable solid parts. The forcing term is a *simplified model* representing the boundaries [135]. In order to prevent stiffness of numerical solver for rigid boundaries, even by means of feedback forcing, a very low CFL number of $O(10^{-3} - 10^{-2})$ is required, which for 3-dimensional (3D) problems might be cumbersome [138].

2. Discretized forcing approach [138], where Dirichlet's BC is imposed by exerting a discretized force in the following format

$$\frac{u^{l+1} - u^{l}}{\Delta t} = \mathrm{RHS}^{l+1/2} + f^{l+1/2}$$

$$f^{l+1/2} = -\mathrm{RHS}^{l+1/2} + \frac{V_B^{l+1} - u^{l}}{\Delta t},$$

   where the RHS contains the convective, pressure and viscous terms. This method does not suffer from numerical stiffness, and can also be used for moving 3D solid surfaces.

3. Ghost cell IB method [see e.g. 139, among many others], where boundary conditions are imposed by means of ghost points (those points in the solid cells, which are in the vicinity

of the fluid domain). This method is well suited for stationary rigid bodies, and can capture solid boundaries sharply. The Dirichlet and Neumann BCs can be imposed exactly (without incorporation of any models); however, extending this method to moving boundaries needs special considerations. Treating 3D complex objects such as roughness, where cusp points, concave/convex curvatures and other types of singularities exist in the domain, is not straightforward in this method. Issues arise when there are multiple image points for a ghost cell, or there are none. Luo et al. [140] addressed some of these issues in 2-dimensional (2D) domains. Also interpolation schemes are dependent on the ghost point location in the solid domain, which demands at least 3 different types of interpolation for 2D domains. The situation is more complicated for 3D ones.

The following comprises a brief description of different studies on IB methods, with emphasis on the compressible flow regimes.

Ghias et al. [141] used ghost cell method to simulate 2D viscous subsonic compressible flows. They imposed Dirichlet's BC for u and T, the equation of state for P and extrapolation for ρ (see section 5.2 as for definition of different parameters). Their method accuracy was second order, locally and globally. Vitturi et al. [142] used a discretized forcing approach, based on a finite volume solver, to simulate 2D/3D viscous subsonic multiphase compressible flows. They imposed Dirichlet's BC for u and T, the equation of state for P and flux correction for ρ and E. Chaudhuri et al. [143] used combined ghost cell and direct forcing methods to simulate 2D inviscid, sub-supersonic compressible flows.They used the equation of state for P, and direct forcing for ρ, u and E equations. They kept the fifth order accuracy of WENO shock-capturing scheme by using two layers of ghost cells. Wang et al. [144] used continuous forcing (penalty IB method) to simulate fluid-structure interaction with 2D compressible (sub, super, and hyper sonic) multiphase flow. Yuan & Zhong [145] used ghost cell method to simulate 2D (sub- supersonic) compressible flows around moving bodies.

5.1.2 Literature review: physics of flows over roughness

Tyson & Sandham [133] analyzed supersonic channel flows over 2D sinusoidal roughness at Mach number (M) of $M = 0.3$, 1.5 and 3 to understand compressibility effects on mean and turbulence properties across the channel. They used body-fitted grids to perform the simulations and found that the values of velocity deficit decrease with increasing the Mach number. Their results suggest strong alternation of mean and turbulence statistics by the shock patterns associated with the wall roughness.

Ekoto et al. [146] experimentally investigated the effects of square and diamond roughness elements on the supersonic turbulent boundary layers. The objective of their study was to understand how roughness topography alters the *local strain-rate distortion*, d_{max}, which has a direct effect on turbulence production. Their results indicate that the surface with *d-type* square roughness generated weak bow shocks upstream of the cube elements, causing a small value of d_{max} (≈ -0.01), and the surface with diamond elements generated strong oblique shocks and expansion waves near the elements, causing a large variation in d_{max} (ranging from -0.3 to 0.4 across the elements). These values of d_{max} led to a canonical rough-wall boundary layer trend for the square roughness and regions with localized extra turbulence production for the diamond surface.

Studies of Latin et al. ([127], [147] and [148]) include a comprehensive investigation on supersonic turbulent boundary layers over rough walls. Five rough surfaces (including 2D bar, 3D cube, and three different sandgrain roughness) have been analyzed at $M = 2.9$. Effects of wall roughness on mean flow, turbulence, energy spectra and flow structures are studied to understand the physics of flow, to expand experimental database, and to evaluate algebraic numerical models for flows in this regime. Their results show strong linear dependence of turbulence statistics on the surface roughness, and also, strong dependence of turbulent structures length scales and inclination angles on the roughness topographies.

Muppidi & Mahesh [149] analyzed the role of ideal distributed roughness on transition to turbulence in supersonic boundary layers. They have found that counter-rotating vortices, generated by the roughness elements, break the overhead shear layer up, which leads to transition to turbulence

more quickly. A similar study was made by Bernardini et al. [132], who investigated the role of isolated cubical roughness on boundary layer transition. Their results suggest the interaction of hairpin structures, shed by the roughness element, with the shear layer expedites transition to turbulence, regardless of the Mach number.

5.1.3 Objectives

In this study we first introduce a level-set based immersed boundary method that can accurately capture the mean and turbulence fields. Then we analyze the flow physics in supersonic channel flows at $M = 1.5$ and bulk Reynolds number of 3000 over two 2-dimensional (2D) and two 3-dimensional (3D) sinusoidal surfaces. Different mean, turbulence and energy quantities are analyzed, and finally, the transport equations of turbulence kinetic energy (TKE) and normal Reynolds stress in the streamwise direction are examined.

5.2 Problem formulation

5.2.1 Governing equations

The non-dimensional form of compressible Navier-Stokes equation are

$$\frac{\partial \rho}{\partial t} + \frac{\partial}{\partial x_i}(\rho u_i) = 0, \tag{5.1a}$$

$$\frac{\partial \rho u_i}{\partial t} + \frac{\partial}{\partial x_j}\left(\rho u_i u_j + p\delta_{ij} - \frac{1}{\mathrm{Re}}\tau_{ij}\right) = f_1\delta_{i1}, \tag{5.1b}$$

$$\frac{\partial E}{\partial t} + \frac{\partial}{\partial x_i}\left[u_i(E+p) - \frac{1}{\mathrm{Re}}u_j\tau_{ij} + \frac{1}{(\gamma-1)\mathrm{PrRe}M^2}q_i\right] = f_1 u_1, \tag{5.1c}$$

where x_1, x_2, x_3 (or x, y, z) are coordinates in the streamwise, wall-normal and spanwise directions, with corresponding velocities of u_1, u_2 and u_3 (or u, v and w). Density, pressure, temperature and dynamic viscosity are denoted by ρ, p, T and μ, respectively. $E = p/(\gamma-1) + \rho u_i u_i/2$ is the total energy, $\tau_{ij} = \mu\left(\frac{\partial u_i}{\partial x_j} + \frac{\partial u_j}{\partial x_i} - \frac{2}{3}\frac{\partial u_k}{\partial x_k}\delta_{ij}\right)$ is the viscous stress tensor, and $q_i = -\mu\frac{\partial T}{\partial x_i}$ is the thermal heat flux. f_1 is a body force that drives the flow in the streamwise direction, analogous to the pressure

gradient. The reference Reynolds, Mach and Prandtl numbers are, respectively, $\mathrm{Re} \equiv \rho_r U_r L_r/\mu_r$, $M \equiv U_r/\sqrt{\gamma R T_r}$, and $\mathrm{Pr} \equiv \mu_r C_p/\kappa$, where subscript r stands for reference values. The gas constant R and the specific heats C_p and C_v are assumed to be constant throughout the domain (calorically perfect gas). They are related by $R = C_p - C_v$, and the ratio of specific heats $\gamma \equiv C_p/C_v$ is assumed to be 1.4. The heat conductivity coefficient is denoted by κ.

The set of equations in (5.1) is closed through the equation of state, which for a perfect gas is

$$p = \frac{\rho T}{\gamma M^2}. \tag{5.2}$$

Equations (5.1) and (5.2) are solved using a finite-difference method in a conservative format and a generalized coordinate system. A fifth-order monotonicity-preserving (MP) shock-capturing scheme and a sixth order compact scheme are utilized for calculating the inviscid and viscous fluxes respectively. The solver uses local Lax-Friedriches (LLF) flux-splitting method and employs an explicit third-order Runge-Kutta scheme for time advancement. Readers are referred to Li & Jaberi [150] for extensive details and explanations about the compressible solver.

5.2.2 Details of the present IB method

We used a combination of level-set and volume-of-fluid (VOF) methods. The level-set field is obtained by solving

$$\psi_\tau = \mathrm{sign}(\psi)(1 - |\boldsymbol{\nabla}\psi|), \tag{5.3}$$

where τ is a fictitious time controlling the width of the interface. This approach is suitable for stationary interfaces and assures that ψ is sign-distanced in the vicinity of $\psi = 0$ level [151, 152]. The initial level-set field is defined as

$$\psi_0 = \begin{cases} 1 & \text{for fluid cells,} \\ 0 & \text{for interface cells,} \\ -1 & \text{for solid cells.} \end{cases} \tag{5.4}$$

It is sufficient to march in (fictitious) time until $\tau = O(\epsilon)$, ϵ being the (relative) width of the interface, to have a smooth and converged solution for ψ. Then the VOF field, ϕ, is defined as

$$\phi \equiv (1 + \psi)/2, \tag{5.5}$$

and $\phi = 0$, $0 < \phi < 1$, and $\phi = 1$, respectively, correspond to solid, interface and fluid cells. The normal direction at the interface is calculated using

$$\widehat{\boldsymbol{n}} = \boldsymbol{\nabla}\psi = \boldsymbol{\nabla}\phi/|\boldsymbol{\nabla}\phi|, \tag{5.6}$$

positive into the fluid.

To impose the desired boundary condition for a test variable θ, we simply correct its value at the boundaries before each time step. It reads as

$$\theta \rightarrow \phi\theta + (1 - \phi)\theta_b, \tag{5.7}$$

for Dirichlet's BC, and

$$\frac{\partial\theta}{\partial n} = \boldsymbol{\nabla}\theta \cdot \widehat{\boldsymbol{n}} = \left.\frac{\partial\theta}{\partial n}\right|_b \tag{5.8}$$

for Neumann's BC. Implementation of Dirichlet's BC is straightforward. Readers are referred to appendix B for details of implementing Neumann's BC. The subscript b in equations (5.7) and (5.8) denotes the boundary values.

Both corrections in equations (5.7) and (5.8) use first-order interpolations to impose the boundary conditions. As a consequence, the solver accuracy would locally reduce to first-order in the vicinity of roughness. It is worth-noting that this is a familiar problem for IB methods, even for those based on the ghost-cell and feed-back forcing approaches, as they mostly use first-order interpolations to correct for the boundary conditions.

5.2.3 Surface roughnesses and simulation parameters

Fully developed, periodic compressible channel flows are simulated using four roughness topographies. The channels are roughened only at one surface (bottom wall) and the other surface

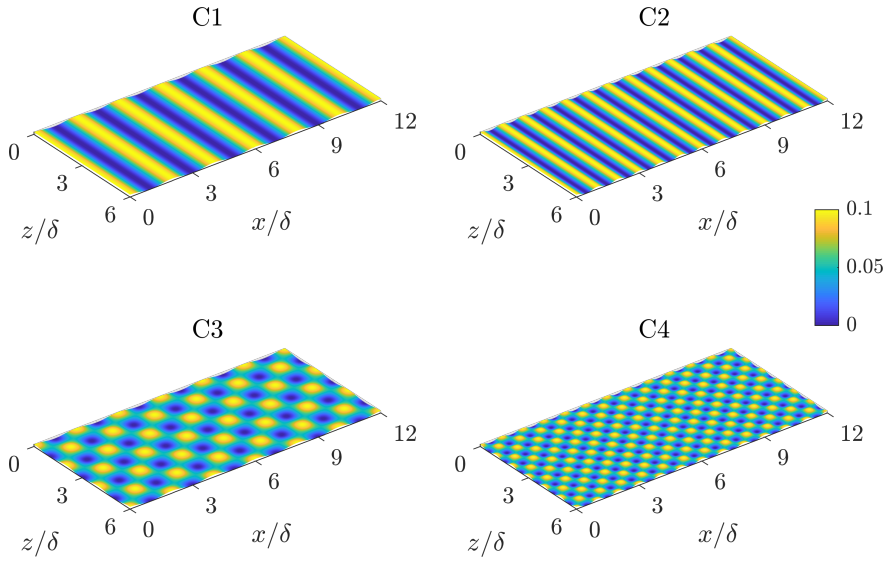

Figure 5.1: Surface roughnesses.

is smooth. A reference smooth-wall channel is also simulated for validation and comparison purposes. The channels dimensions in streamwise, wall-normal and spanwise directions are, respectively, $L_x = 12\delta$, $L_y = 2\delta$ and $L_z = 6\delta$, where δ is the channel half-height and equals to 1.

Figure 5.1 shows four roughness topographies used for the present simulations. All cases share the same crest height, $k_c = 0.1\delta$. The trough location is set at $y = 0$. Case C1 and C2 are 2-dimensional (2D) sinusoidal surfaces with streamwise wave-lengths of $\lambda_x = 2\delta$ and $\lambda_x = \delta$, respectively. The roughness heights, $k(x, z)$, for these surfaces are obtained by

$$k(x, z) = 0.05\big[1 + \cos(2\pi x/\lambda_x)\big]. \tag{5.9}$$

Case C3 and C4 are 3-dimensional (3D) sinusoidal surfaces with streamwise and spanwise wave-lengths of $(\lambda_x, \lambda_z) = (2\delta, 2\delta)$ for C3, and $(\lambda_x, \lambda_z) = (\delta, \delta)$ for C4. The roughness heights for them are obtained by

$$k(x, z) = 0.05\big[1 + \cos(2\pi x/\lambda_x)\cos(2\pi z/\lambda_z)\big]. \tag{5.10}$$

Case	k_c	k_{avg}	k_{rms}	R_a	E_x	E_z	S_k	K_u
C1	0.1	0.05	0.035	0.032	0.100	0.000	0.0	1.50
C2	0.1	0.05	0.035	0.032	0.200	0.000	0.0	1.50
C3	0.1	0.05	0.025	0.020	0.064	0.064	0.0	2.25
C4	0.1	0.05	0.025	0.020	0.127	0.127	0.0	2.25

Table 5.1: Statistical parameters of roughness topography. $k_{avg} = \frac{1}{A_t}\int_{x,z} k\,dA$ is the average height, $k_{rms} = \sqrt{\frac{1}{A_t}\int_{x,z}(k-k_{avg})^2 dA}$ is the root-mean-square (RMS) of roughness height fluctuation, $R_a = \frac{1}{A_t}\int_{x,z}|k-k_{avg}|dA$ is the first-order moment of height fluctuations, $E_{x_i} = \frac{1}{A_t}\int_{x,z}\left|\frac{\partial k}{\partial x_i}\right| dA$ is the effective slope in the x_i direction, $S_k = \frac{1}{A_t}\int_{x,z}(k-k_{avg})^3 dA \Big/ k_{rms}^3$ is the height skewness, and $K_u = \frac{1}{A_t}\int_{x,z}(k-k_{avg})^4 dA \Big/ k_{rms}^4$ is the height kurtosis; where $k(x,z)$ is the roughness height distribution and $A_f(y)$ and A_t are the fluid and total planar areas. Values of k_c, k_{avg}, k_{rms} and R_a are normalized by δ.

Table 5.1 summarizes some statistical properties of the surfaces and their definitions. These statistics are different moments of surface height, surface effective slopes and porosity.

For a test variable θ, the time, Favre and spatial averaging operators are shown respectively by $\overline{\theta}$, $\widetilde{\theta} = \overline{\rho\theta}/\overline{\rho}$ and $\langle\theta\rangle$ (sums over homogeneous directions x and z), with corresponding fluctuation component of θ', θ'' and θ'''. Therefore

$$\begin{aligned}\theta &= \overline{\theta} + \theta' \\ &= \widetilde{\theta} + \theta'' \\ &= \langle\theta\rangle + \theta'''.\end{aligned} \tag{5.11}$$

Periodic BCs are used in the streamwise and spanwise directions. A no-slip iso-thermal wall BC is imposed at both top and bottom walls, assuming $\boldsymbol{u}_w = \mathbf{0}$ and $T_w = 1.0$ (w denotes the wall values). There is no need to impose a BC for density, and equation (5.1a) can be solved using one-sided differentiation to update the density values at the boundaries. This approach is similar to other wall-bounded compressible flow studies [see e.g. 7, 133]. The pressure at the boundaries is calculated through the equation of state.

The reference density and velocity are those of bulk values, defined as $\rho_r = \frac{1}{2\delta}\int_0^{2\delta}\langle\overline{\rho}\rangle dy$ and $U_r = \frac{1}{2\delta}\int_0^{2\delta}\langle\overline{u}\rangle dy$. Both of these parameters are constrained to be equal to 1, and the time-

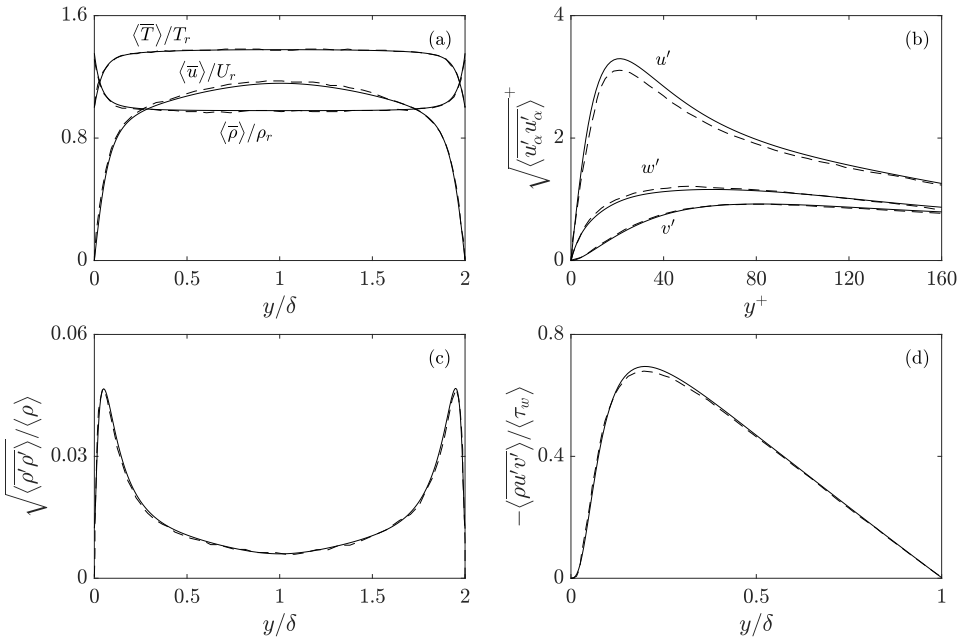

Figure 5.2: Profiles of mean and turbulence variables for the smooth-wall flow at Re = 3000 and $M = 1.5$. Present simulation (*solid lines*), [7] (*dash line*). $\tau_w = \frac{1}{\mathrm{Re}}\frac{d\overline{u}}{dy}\big|_w$.

dependent body force f_1 in NS equation (5.1) is determined so as to impose these constraints at each time step. The reference length and temperature scales are δ and $T_r = T_w$, respectively. The simulations are conducted at Re = 3000 and $M = 1.5$, assuming Pr = 0.7 and $\mu = T^{0.7}$ (note both μ and T are already non-dimensionalized).

The respective grid sizes in the x, y and z directions are $n_x = 800$, $n_y = 200$ and $n_z = 400$. For the present channel size and Reynolds number of the simulations, the grid corresponds to Δx^+, Δy^+_{max} and Δz^+ less than 3.0, which is fine enough for DNS. Also the first 3 grid points in the wall-normal direction are in the $y^+ < 1.0$ region. The simulations are sufficiently run in time to reach the stationary turbulence and thereafter the statistics are averaged over approximately 20 large eddy turn over time.

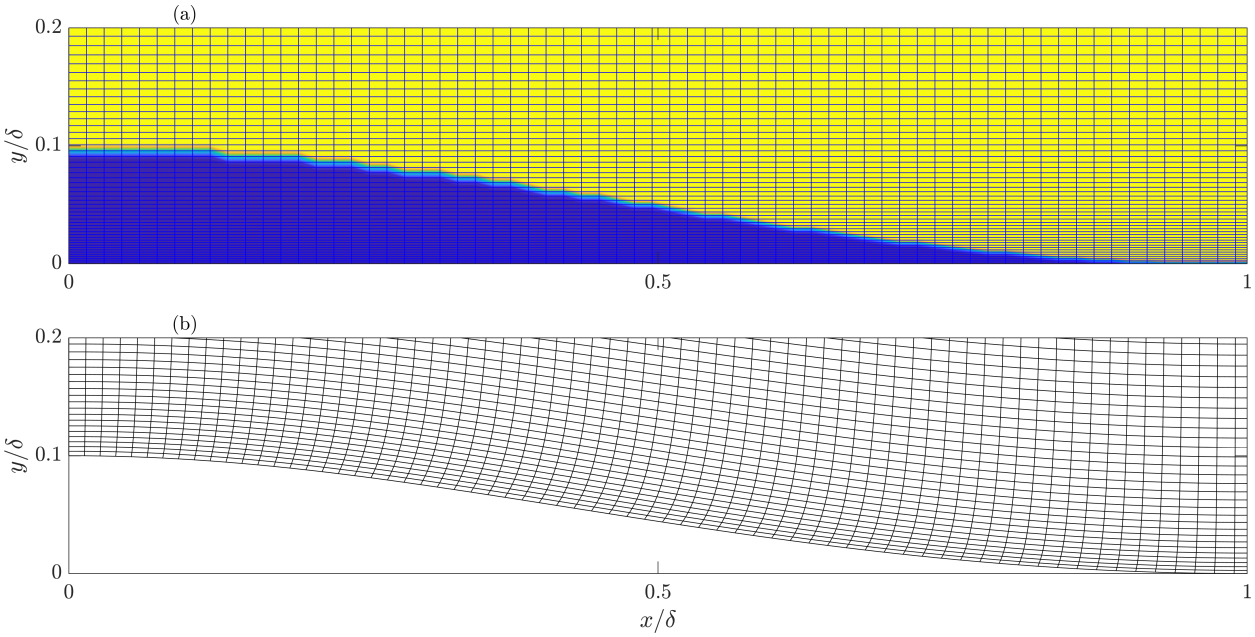

Figure 5.3: Contour of level set ϕ for the IB method (a), mesh grid for the conformal setup (b). Case C1.

5.2.4 Validation of the numerical method and the proposed IB method

The numerical method is validated by simulating supersonic turbulent channel flow over a smooth wall at $M = 1.5$ and Re = 3000. The same setup was also employed by Coleman et al. [7], which is used here as the benchmark study.

Figure 5.2 compares mean and turbulence properties of the present simulation with those of Coleman et al. [7]. As the figure shows, the two simulations are in a good agreement for all depicted variables. This verifies that our numerical solver is implemented correctly.

To validate the proposed IB method, we have simulated case C1 in two ways: one uses the IB method and the other solves the conventional NS equations on a conformal body-fitted mesh setup. The contour of level set for the IB method and the mesh of the conformal setup are shown in figure 5.3.

Figure 5.4 shows profiles of different mean and turbulence variables, including mean velocity, temperature and density as well as Reynolds stresses and variance of temperature. All these plots indicate a very good match between the simulation with IB method and the simulation with the

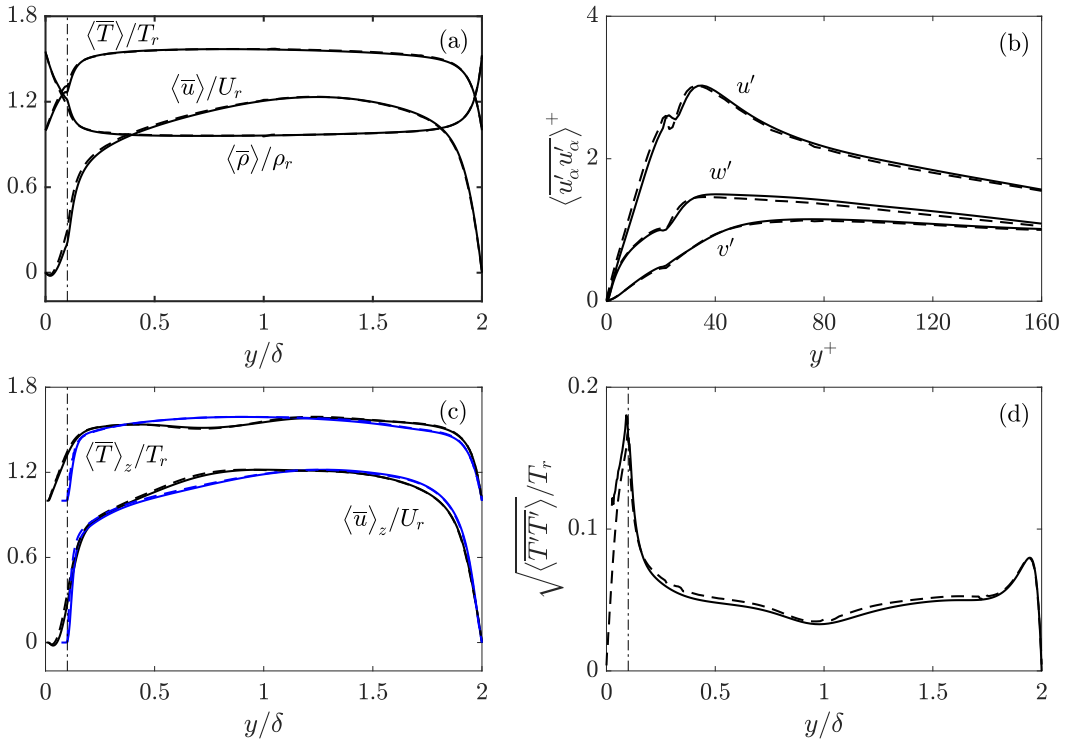

Figure 5.4: Plots of the mean and turbulence variables for case C1, simulated by using the IB method (solid lines) and the conformal mesh setup (dash lines). Profiles of double-averaged velocity, temperature and density (a), RMS of velocity components in plus units (roughness side, b), time and spanwise average of velocity and temperature at the roughness crest and valley locations (c), and RMS of temperature (d). The vertical dot-dash lines show $y = k_c$.

body-fitted mesh. Therefore, we conclude the proposed IB method has the accuracy needed for a valid DNS analysis.

5.3 Results

Contours of the instantaneous streamwise velocity field are plotted in figure 5.5 for all cases. Strong modifications of the near wall turbulence, especially in the roughness side, are noticeable from the figures. The main difference between the present geometries, however, is the shock patterns generated by 2D and 3D roughnesses, which are visible in contours of $\boldsymbol{\nabla \cdot u}$, shown in figure 5.6. As this figure shows, 2D surfaces (cases C1 and C2) impart strong shock patterns that

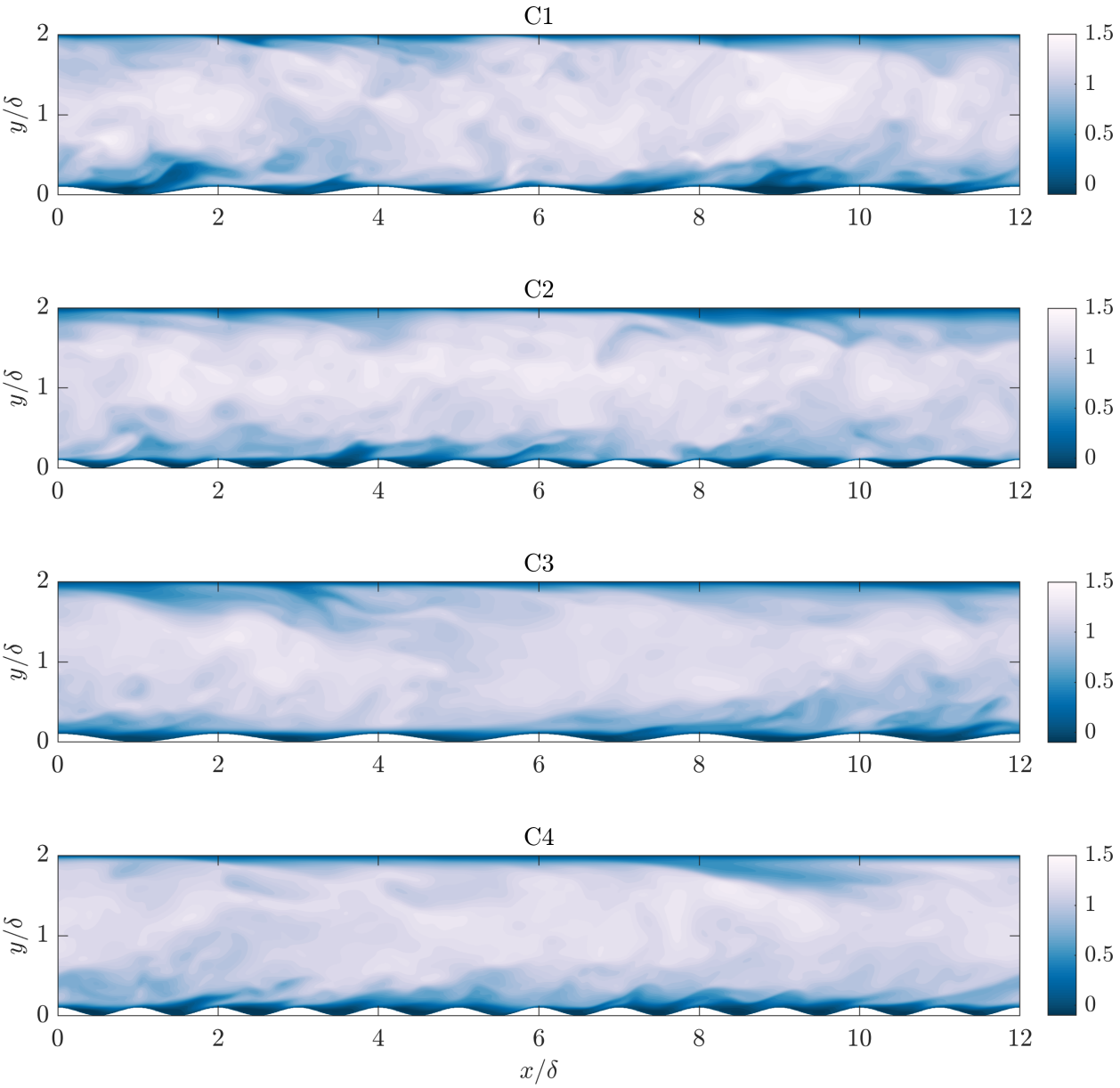

Figure 5.5: Contours of instantaneous u.

go all the way up to the upper surface and reflect from this wall to the domain. These shock patterns exhibit the same wavelength of the roughness geometries, and can influence the flow properties in the whole channel. This is obvious in the contours of instantaneous temperature fields in figure 5.7, where temperature periodically changes in the compression and expansion regions associated with roughness geometries in C1 and C2. For 3D cases all the embedded shock patterns are broken and, consequently, replaced by the small-scale shocklets, which are distributed over the whole domain with a very slight dependence on the roughness wavelengths.

5.3.1 Mean and turbulence variables

Figure 5.8 compares profiles of the mean and turbulence quantities between different test cases. The mean streamwise velocity (figure 5.8a) and density (not shown) show a similar trend for all cases, which, other than the near wall regions, are weakly dependent on the roughness geometry across the channel height. The temperature profiles (figure 5.8c), on the other hand, depend on the roughness topographies, and are higher for 2D cases (C1 and C2) compared to the 3D ones (C3 and C4). As explained in section (5.2.1), the constraints of $U_r = 1$ and $\rho_r = 1$ were imposed on the velocity and density fields, respectively. These constraints subsequently prevent major differences in velocity and density profiles between different roughness cases and that is why they are almost indifferent to the roughness geometries. However, such a constraint does not exist for the temperature fields, and since strong shock patterns in 2D cases involve more entropy in the domain than the 3D cases, the irreversible heat generation is higher for these cases and therefore the temperature is higher for them than for the 3D surfaces.

The values of frictional velocities in the smooth and rough sides as well as the frictional Reynolds number Re_τ and drag coefficient C_f are tabulated in table 5.2. Both of Re_τ and C_f show similar trends to the temperature profiles: *i)* they are higher for 2D cases than 3D ones, *ii)* they decrease with decreasing roughness wavelength in 2D surfaces, and *iii)* they increase with decreasing roughness wavelengths in 3D surfaces. The associated shock patterns are believed to also be responsible for these trends as explained above. We add that the flow blockage due to

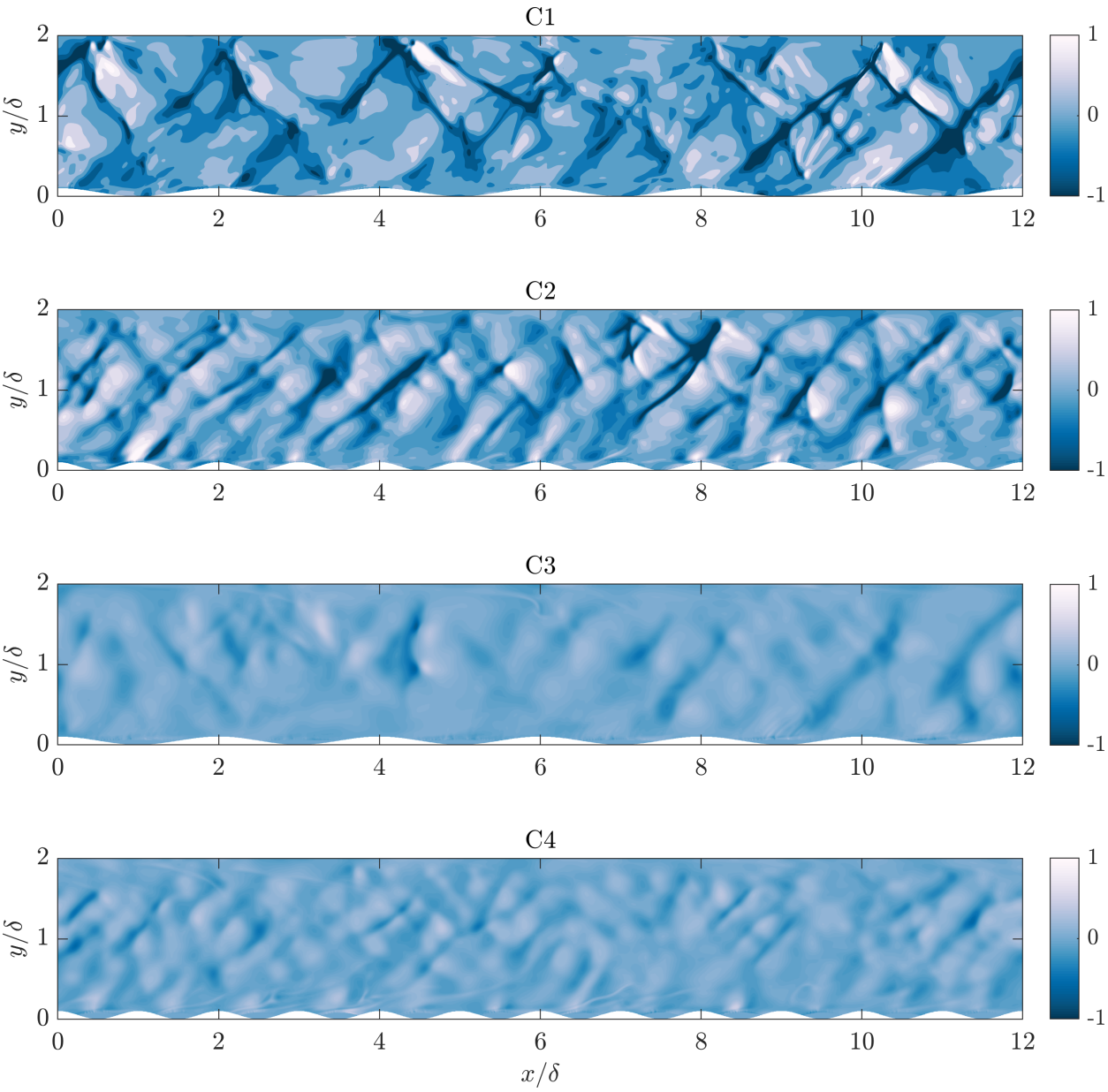

Figure 5.6: Contours of instantaneous $\boldsymbol{\nabla \cdot u}$.

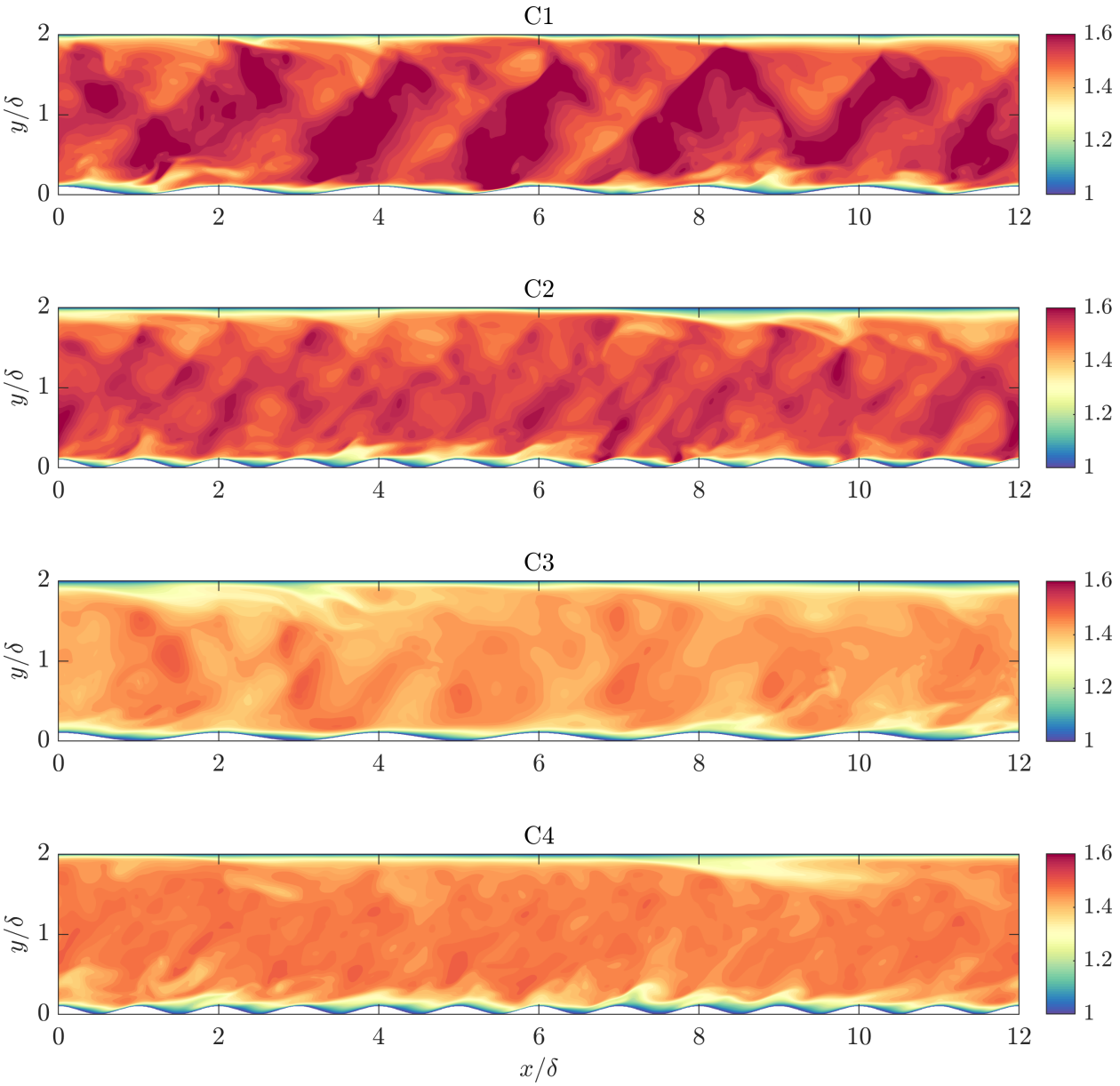

Figure 5.7: Contours of instantaneous T.

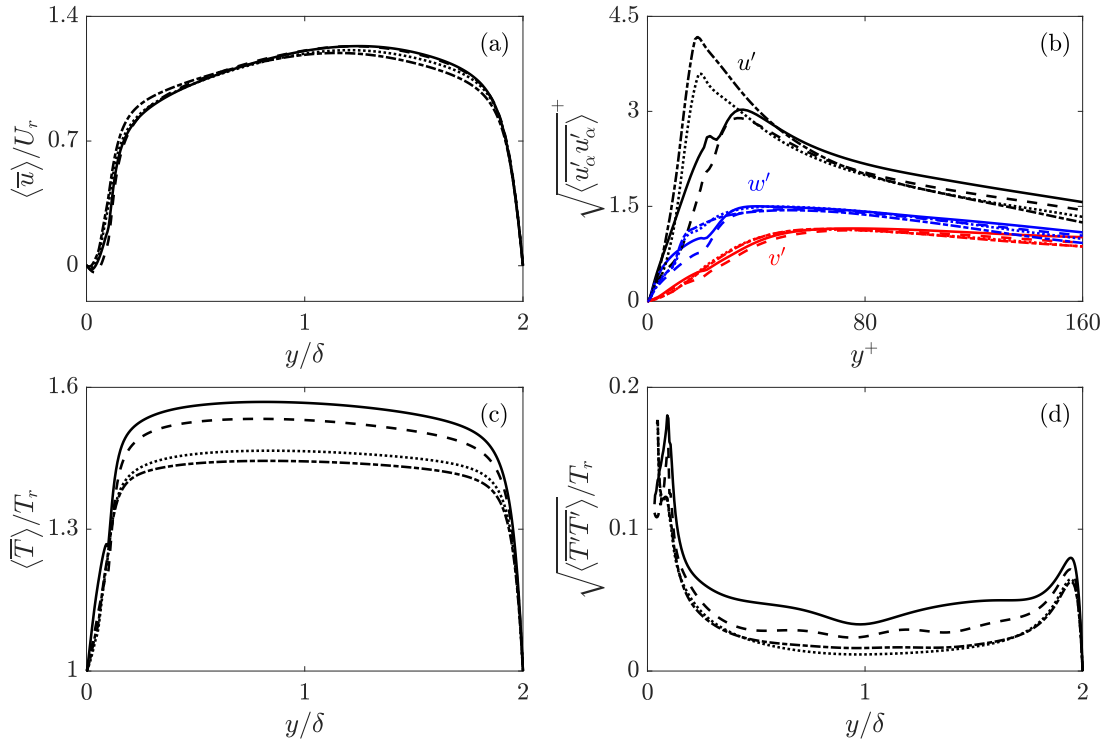

Figure 5.8: Plots of the mean and turbulence variables for all cases. Profiles of the double-averaged streamwise velocity (a), components of Reynolds stresses in plus units (roughness side, b), double-averaged of temperature (c), and RMS of temperature (d). C1 (solid lines), C2 (dash lines), C3 (dot-dash lines) and C4 (dotted lines).

Case	$u_{\tau,s}/U_r$	$u_{\tau,r}/U_r$	$u_{\tau,avg}/U_r$	Re_τ	$C_f \times 10^3$
C1	0.0652	0.0721	0.0687	206	9.4
C2	0.0660	0.0675	0.0668	200	8.9
C3	0.0650	0.0577	0.0615	184	7.6
C4	0.0657	0.0620	0.0639	191	8.2

Table 5.2: Post processing data. $u_{\tau,s} = \sqrt{\tau_{w,s}/\rho_r}$ and $u_{\tau,r} = \sqrt{\tau_{w,r}/\rho_r}$, where $\tau_{w,s} = -\mu_w \frac{d<\overline{u}>}{dy}\big|_{y=2\delta}$ and $\tau_{w,r} = -\int_0^{k_c} \langle \overline{F}_{1,ibm} \rangle_T dy$. Here $F_{i,ibm} = \rho \frac{\Delta u_i}{\Delta t}$ is the corresponding body force due to IBM (Δu_i is the velocity difference of u_i after and before the IBM correction step). $\langle \cdot \rangle_T$ is a simple planar averaging operator that includes all the solid and fluid cells. $\mathrm{Re}_\tau = \rho_r u_{\tau,avg} \delta/\mu_w$, $C_f = 2(u_{\tau,avg}/U_r)^2$ and $u^2_{\tau,avg} = \left(u^2_{\tau,s} + u^2_{\tau,r}\right)/2$.

roughness does not change significantly by decreasing roughness wavelength for 2D surfaces (as the roughness elements are already spanned in the entire width of the channel), while it increases for the present 3D surfaces. This can further explain the trends of *(ii)* and *(iii)*, considering that the hydraulic drag is proportional to the flow blockage due to surface roughness.

The RMS of velocity components are plotted in figure (5.8 b) in viscous units, where they are normalized by $u_{\tau,r}$ (see table 5.2 for definition) and $\delta_{\nu,r} = \mu_w/(\rho_r u_{\tau,r})$. The plots show that roughness effects are confined to the roughness sublayer region and outside this region the profiles almost collapse for all velocity components. The v and w components also exhibit almost the same trend for regions inside the roughness sublayers. However, the u components for 3D cases show higher profiles than their 2D counterparts for $y \leq k_c$. This is because they can impart larger coherent motions (of the orders greater than λ_x) in the streamwise direction than the 2D surfaces in $y \leq k_c$, due to their being three dimensional.

The RMS of temperature, figure (5.8d), depends strongly on the roughness geometry in the outer layer. For 2D cases, the irregularly shaped regions in the figure are associated with the shock patterns in the domain, and occur in the locations where the shock waves coincide and form the nodes of the shock diamonds (the nodes that are away from walls). These shock diamonds are also visible in figure 5.7 (C1 and C2). For 3D cases the shock diamonds are deteriorated by the roughnesses, therefore no obvious bumpy region occurs in their profiles of the RMS of temperature.

5.3.2 Budgets of the Reynolds stresses

The transport equation for different components of the Reynolds stress tensor reads as [153]

$$\begin{aligned}\frac{\partial}{\partial t}(\overline{\rho u_i'' u_j''}) = C_{ij} + \mathcal{P}_{ij} + \mathcal{D}^M_{ij} + \mathcal{D}^T_{ij} + \\ \mathcal{D}^P_{ij} + \Pi_{ij} + \epsilon_{ij} + \mathcal{M}_{ij},\end{aligned} \tag{5.12}$$

where $i, j = \{1, 2, 3\}$ and C, $\mathcal{P}$, $\mathcal{D}^M$, $\mathcal{D}^T$, $\mathcal{D}^P$, Π, ϵ and $\mathcal{M}$, are, respectively, mean convection, production, molecular diffusion, turbulent diffusion, pressure diffusion, pressure-strain, dissipation,

and turbulent mass flux terms, and are defined as

$$
\begin{aligned}
C_{ij} &= -\frac{\partial}{\partial x_k}(\overline{\rho u_i'' u_j''}\widetilde{u}_k) \\
\mathcal{P}_{ij} &= -\overline{\rho u_i'' u_k''}\frac{\partial \widetilde{u}_j}{\partial x_k} - \overline{\rho u_j'' u_k''}\frac{\partial \widetilde{u}_i}{\partial x_k} \\
\mathcal{D}_{ij}^{M} &= \frac{\partial}{\partial x_k}(\overline{u_i''\tau_{kj}} + \overline{u_j''\tau_{ki}}) \\
\mathcal{D}_{ij}^{T} &= -\frac{\partial}{\partial x_k}(\overline{\rho u_i'' u_j'' u_k''}) \\
\mathcal{D}_{ij}^{P} &= -\frac{\partial}{\partial x_k}(\overline{p' u_i''}\delta_{jk} + \overline{p' u_j''}\delta_{ik}) \\
\Pi_{ij} &= \overline{p'\left(\frac{\partial u_i''}{\partial x_j} + \frac{\partial u_j''}{\partial x_i}\right)} \\
\epsilon_{ij} &= -\overline{\tau_{ki}\frac{\partial u_j''}{\partial x_k}} - \overline{\tau_{kj}\frac{\partial u_i''}{\partial x_k}} \\
\mathcal{M}_{ij} &= \overline{u_i''}\left(\frac{\partial \overline{\tau}_{kj}}{\partial x_k} - \frac{\partial \overline{p}}{\partial x_j}\right) + \overline{u_j''}\left(\frac{\partial \overline{\tau}_{ki}}{\partial x_k} - \frac{\partial \overline{p}}{\partial x_i}\right).
\end{aligned}
\tag{5.13}
$$

The budgest are calculated for all non-zero components of the Reynolds stress tensor, B_{11}, B_{22}, B_{33} and B_{12} as well as for TKE. However, only the results of TKE and B_{11} are shown here for brevity (figures 5.9 and 5.10). The figures are normalized by the reference units for comparison purposes. In the figures, σ is the residual of the budgets, and is less than 1% in all cases. This not only verifies that budgets are calculated correctly, but also, confirms that the numerical dissipation (as a result of the solver's flux-splitting procedure and the IB method), is small, which is essential for an accurate DNS analysis.

The budget terms are strongly modified by the roughness elements in all figures. The production terms in TKE and B_{11} budgets, are higher for 2D cases than the 3D ones. Beyond the strong shear values in the wakes of the 2D elements which enhances the shear production [57], there are two other reasons for this. First, for 2D surfaces, all streamwise turbulence structures are broken by the roughness elements which span the width of the channel, the effects of which can grow to the boundary layer thickness even in the incompressible flows [17]. This results in smaller length scales of turbulence structures and enhanced pressure drag. In 3D surfaces, the streamwise structures

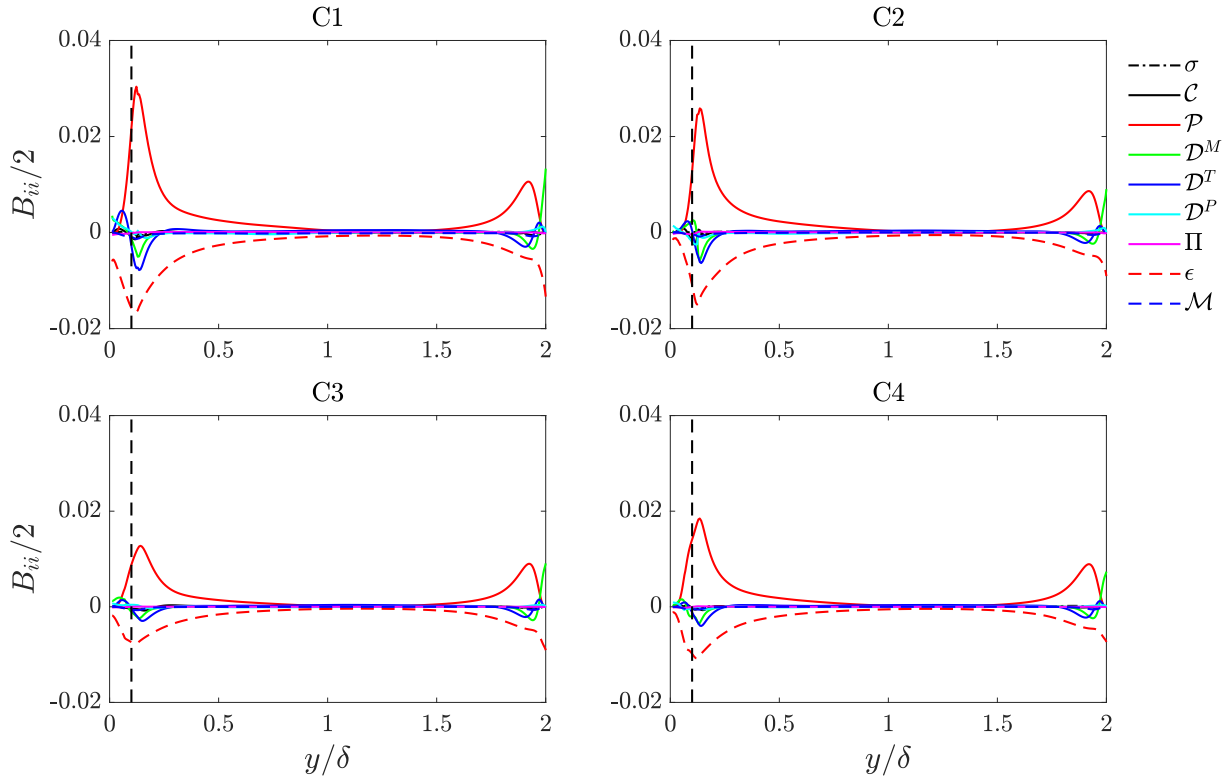

Figure 5.9: Budgets of TKE. All terms are normalized by U_r and δ, and are double-averaged in time and the x-z plane.

wrap around the roughness elements [99] and therefore reduced vortex breakdown and, as a result, turbulence production occurs for these cases. The second reason of enhanced turbulence production for 2D surfaces is the mutual interaction of shock waves. The contours of $\overline{\mathcal{P}}_{11}$ are depicted in figure 5.11 to explain this effect. As the figure shows, for 2D surfaces, the regions where 2 oblique shock waves impinge together have enhanced turbulence production, whether it is in the rough or smooth wall side.

This is an important phenomenon and represents a fundamental difference between supersonic and subsonic turbulent flows over rough walls – for subsonic flows most of the roughness effects are confined to near wall regions and the outer layer is expected to be independent of the wall condition, also known as Townsend [69] outer layer similarity hypothesis. This has been verified in numerous studies in the field [77, 13, 6]. But for the supersonic cases here, as is obvious in figure

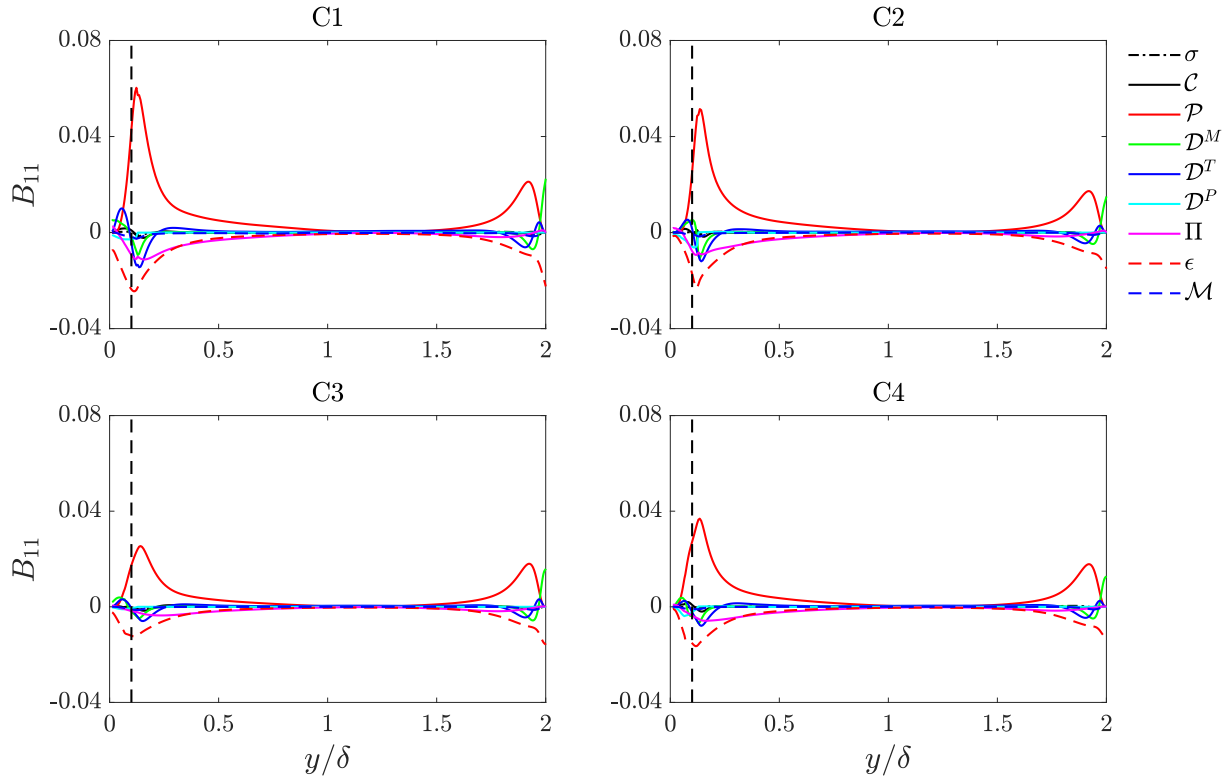

Figure 5.10: Budgets of B11. All terms are normalized by U_r and δ, and are double-averaged in time and the x-z plane.

5.11, the effects of wall roughness, via the generated oblique shocks, propagate across the channel and modify turbulence production in the upper wall region. The same process occurs on the rough wall side, where the reflected shocks, from the smooth side, impinge together near the roughness crest and enhance the turbulence production in these regions. Even for the 3D roughnesses, it is conjectured that turbulence processes, on both sides, depend on the shocklets generated by breaking down the shock patterns, which, by themselves depend on the roughness topographies. This clearly shows that Townsend's outer layer similarity hypothesis does not apply to such supersonic channel flows. Such processes may be of potential use in flow and turbulence control, where one can control the turbulence processes on one side of the channel by altering the wall roughness on the other side.

Similar to $\mathcal{P}$, other turbulence processes are also affected by wall roughness and the associated shock patterns, which are also evident in figures 5.9 and 5.10. In particular, the pressure-strain

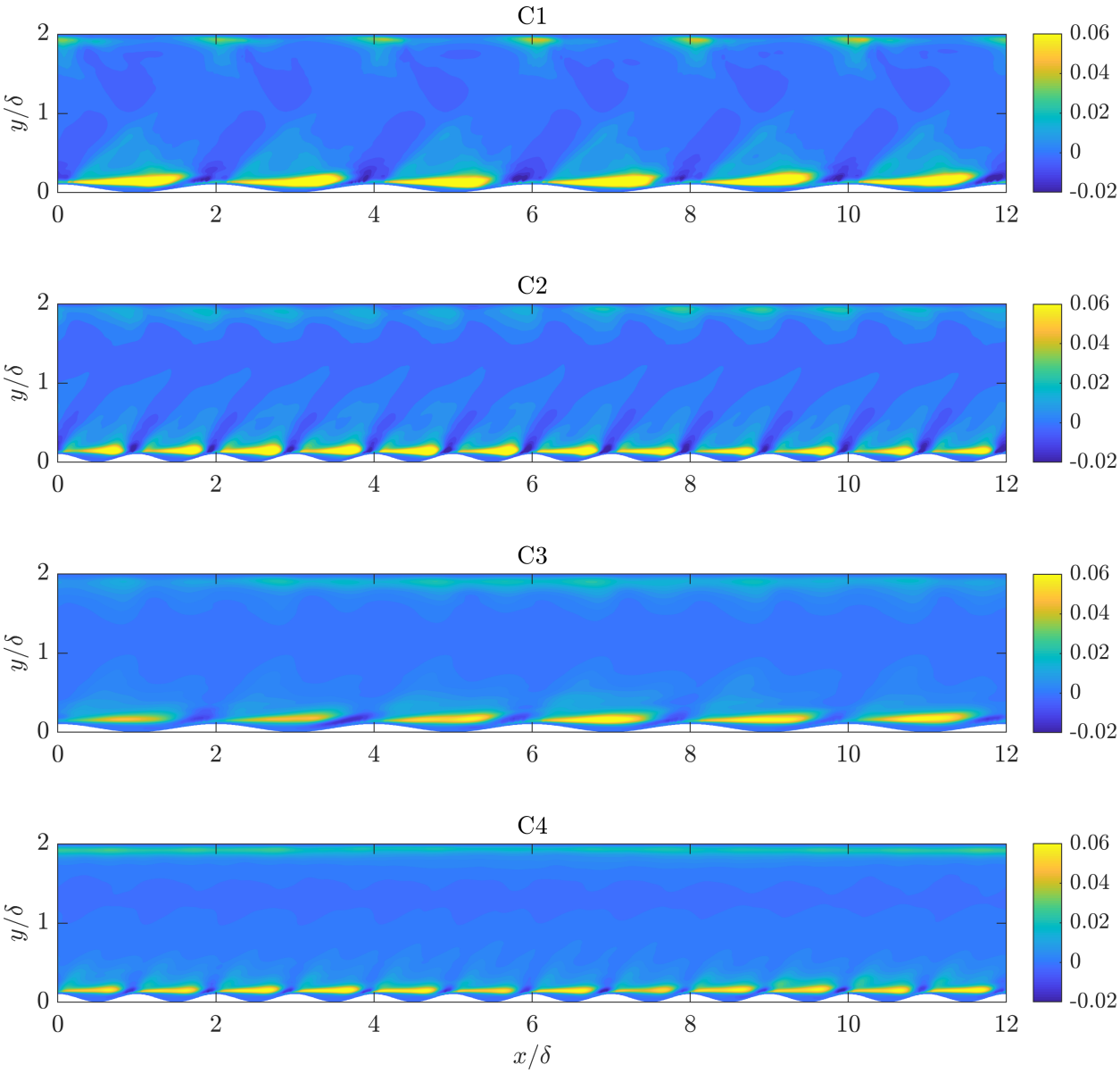

Figure 5.11: Contours of $\overline{\mathcal{P}}_{11}$. It is normalized by U_r and δ.

term Π in B_{11}, reaches its maximum magnitude near the roughness crest location, which indicates an excess turbulence production in this region for vv and ww budgets, as the negative of this term acts as a prominent source term in the B_{22} and B_{33} budgets.

5.4 Concluding remarks

In this study we proposed an immersed boundary method to simulate supersonic turbulent flows over rough walls. To this end, we used a level-set method, and the velocity and temperature fields were corrected to impose Dirichlet and Neumann boundary conditions at the interface cells. The density and pressure were calculated using the continuity and state equations. The method was validated by comparing the DNS results of a sinusoidal wavy wall, which has been simulated using both the IB method and a body-fitted mesh. The simulations results show excellent agreement between mean and turbulence quantities computed with both methods, which confirms the suitability of the IB method for accurate DNS simulations.

In the next step, we have simulated supersonic flows at $M = 1.5$, over four roughness topographies, two of which were 2D sinusoidal surfaces and two were 3D sinusoidal surfaces. The surfaces shared the same roughness height, but they differed in the surface wavelengths. Our results indicate strong modifications of turbulence field as well as the mean and RMS of the temperature fields by the roughness geometries. Specifically, 2D surfaces generate strong oblique shock patterns throughout the channel, which predominantly act to modify the turbulence production term, $\mathcal{P}$. Contour plots of $\overline{\mathcal{P}}$ show that roughness enhances $\mathcal{P}$ not only on the roughness side, but also on the inner-layer of the other wall of the channel. This channel-flow effect is not consistent with the well-known Townsend's outer-boundary-layer similarity hypothesis for incompressible turbulent flows over smooth and rough walls.

Our results show that the 3D rough walls break down the embedded shock patterns and generate randomly oriented weak shocklets. These shocklets impart less entropy into the flow field than the strong shock waves in the 2D cases. This causes less irreversible heat generation for 3D surfaces and cooler temperature fields in these cases.

APPENDICES

APPENDIX A

INTRINSIC AREA FILTERING

A.1 Introduction

Different fields of fluid mechanics such as multi phase flow, flow in porous media, meteorological flows, flow over canopies and roughness, which have some sort of spatial and geometrical anomalies, involve area averaging. To study each of these flow types, one needs to implement area averaging to the governing equations and write the average of derivatives based on derivatives of the average. To study homogeneous multi phase flow and flow over roughness, Howes & Whitaker [40] and Raupach & Shaw [39], respectively, offered a solution to commute averaging and derivation operators, and their efforts were extended by Cushman [154], Giménez-Curto et al. [155] and Nikora et al. [41] for non-homogeneous fields. The source of difficulties in the previous studies is the commuting problem which has a general and concise solution, when the appropriate mathematical tools are used to describe spatial-dependent flow physics.

Because area-averaging is inherently area-filtering, space-filtered ensemble-averaged Navier Stokes (FANS) equations are reintroduced. The double-averaged Naveir-Stokes (DANS) equations can be easily obtained from the FANS equations assuming the averaging area is large enough that the roughness could be assumed homogeneous $\left(\frac{\partial A_r}{\partial x} = \frac{\partial A_r}{\partial z} = 0 \right.$, where A_r is the planar area occupied by the roughness$\Big)$.

A.2 Problem formulation

A.2.1 Intrinsic area filtering

Intrinsic area filtering of a test function ϕ is defined by

$$\big\langle \phi \big\rangle(\boldsymbol{x}) \equiv \frac{1}{A} \iint_{D(O_a,B)} \phi(x', z')\, dA'. \tag{A.1}$$

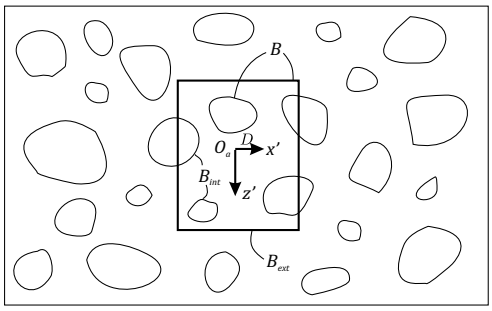

Figure A.1: Schematic of the geometry, auxiliary CS and definitions.

Figure A.1 shows the schematic of the problem, D is the fluid occupied domain and A is its area; $\boldsymbol{x} = (x, y, z, t)$ determines a particle position in space and time (in a right-handed coordinate system) and filtering is performed in the x-z plane. The goal is the calculation of $\left\langle \frac{\partial \phi}{\partial x_i} \right\rangle$ as a function of $\frac{\partial <\phi>}{\partial x_i}$ (to commute averaging and derivation operators); to do so, one needs to define an auxiliary coordinate system to calculate the value of integral. There are two fundamentally different approaches to defining this coordinate system (CS). The first approach, used in previous studies, is to fix the primary domain and displace the filtering area (see figure A.2a); in this case, we have

$$O_a \coloneqq (x, z), \quad B = B\big(x'(y,t), z'(y,t)\big), \tag{A.2a,b}$$

where O_a is the auxiliary CS origin and B determines the boundaries of the filtered domain, D, in this system. In roughness and porous media studies B is the solid-fluid boundary and in multiphase flow B can be the boundary between different phases; therefore, as far as B is concerned, *second phase* and *roughness* will be used interchangeably henceforth.

Although $\left\langle \frac{\partial \phi}{\partial x_i} \right\rangle\Big|_{\boldsymbol{x}}$ is calculable using the first viewpoint, it requires deliberate discussions and advanced mathematical methods. The *time* coordinate also needs special treatment.

As will be shown, there is a general and straightforward method to calculate $\left\langle \frac{\partial \phi}{\partial x_i} \right\rangle$. We must change our view of the problem and use the second approach $i.e.$ to fix the filtering area and displace

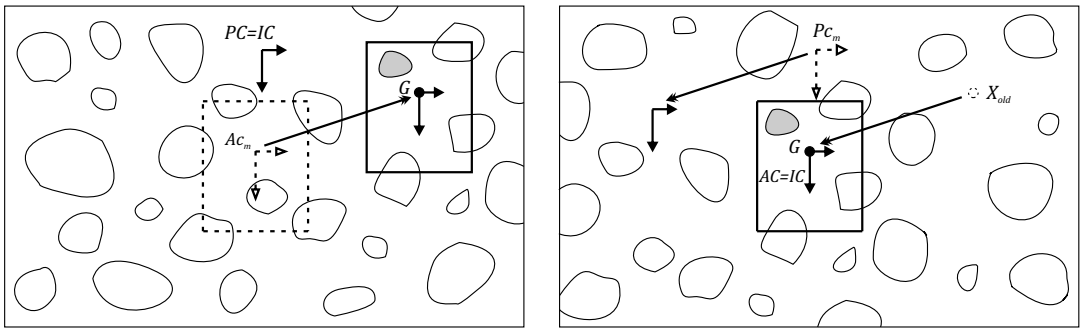

Figure A.2: Schematic of two fundamental viewpoints: (a) auxiliary CS moves, primary CS fixed. (b) auxiliary CS fixed, primary CS moves. In both figures subscript m stands for 'moving', IC stands for 'inertial CS'; and G serves as O_a in auxiliary CS and $\boldsymbol{x}$ in primary CS, in the meantime.

the primary domain (figure A.2b). In this case, we have

$$O_a \coloneqq (0,0), \quad B = B\big(x'(x,y,z,t), z'(x,y,z,t)\big). \tag{A.3a,b}$$

By doing so, and assuming that ϕ has compact support and B is smooth enough (as is the case for any physical process), all conditions of Leibniz's integral rule are satisfied and $\left\langle \frac{\partial \phi}{\partial x_i} \right\rangle\Big|_{\boldsymbol{x}}$ is calculable using this rule as

$$\begin{aligned}
\left\langle \frac{\partial \phi}{\partial x_i} \right\rangle &= \frac{1}{A} \iint_D \frac{\partial \phi}{\partial x_i}\, dA' \\
&= \frac{1}{A}\left(\frac{\partial \iint_D \phi\, dA'}{\partial x_i} - \oint_B \phi\, \boldsymbol{v}_i \cdot \hat{\boldsymbol{n}}\, dl \right) \\
&= \frac{1}{A} \frac{\partial A\langle \phi \rangle}{\partial x_i} - \frac{1}{A} \oint_B \phi\, \boldsymbol{v}_i \cdot \hat{\boldsymbol{n}}\, dl,
\end{aligned} \tag{A.4}$$

where $\boldsymbol{v}_i$ is rate of dilatation of fluid boundary in i^{th} direction (including t). We can separate the boundary into two parts: the interior, B_{int}, and the exterior, B_{ext}. To study regular geometries, one can fix the external boundary ($\boldsymbol{v}_i\big|_{B_{ext}} = 0$) and the equation will be

$$\left\langle \frac{\partial \phi}{\partial x_i} \right\rangle = \frac{1}{A} \frac{\partial A\langle \phi \rangle}{\partial x_i} - \frac{1}{A} \oint_{B_{int}} \phi\, \boldsymbol{v}_i \cdot \hat{\boldsymbol{n}}\, dl. \tag{A.5}$$

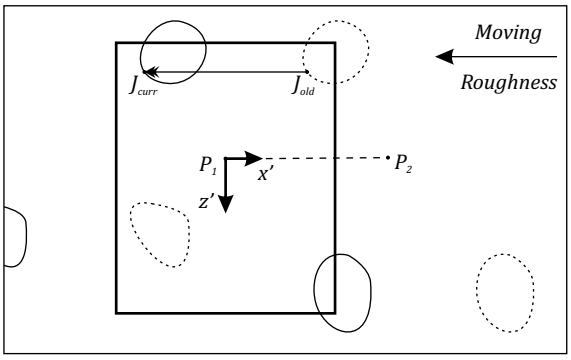

Figure A.3: Representation of *x-dir* velocity, going from P_1 to P_2, in *x-dir* with Δx unit long in primary CS, will result in change of abscissa of a point in auxiliary CS, J, of $\Delta x' = -\Delta x$.

$\hat{\boldsymbol{n}}$ is unit normal vector, positive out of the fluid; and the integral should be traversed counter clockwise on B_{int} according to the theorem.

A.2.2 Calculation of $\boldsymbol{v}_i$

time: $\boldsymbol{v}_t$ is the velocity of the boundary at x-z plane

$$\boldsymbol{v}_t = \left(\frac{\partial x'}{\partial t}, \frac{\partial z'}{\partial t}\right) = \boldsymbol{v}_b\big|_{x-z\ plane}. \tag{A.6}$$

x-dir: considering figure A.3, and assuming we are at point P_1 and want to calculate $\left\langle \frac{\partial \phi}{\partial x} \right\rangle$ at point P_2, we should displace the primary plane in $(-\boldsymbol{i})$ direction with length of $\Delta x = x_{P_2} - x_{P_1}$. In the meantime, the value of x' at an arbitrary point on the boundary, J, would change by $\Delta x' = -(x_{P_2} - x_{P_1}) = -\Delta x$ in the auxiliary coordinate system. One can easily see that

$$\boldsymbol{v}_x = \left(\frac{\partial x'}{\partial x}, \frac{\partial z'}{\partial x}\right) = -\boldsymbol{i}. \tag{A.7}$$

z-dir: we can similarly deduce that $\boldsymbol{v}_z = -\boldsymbol{k}$.

y-dir: $\boldsymbol{v}_y$ can be represented in various forms according to the types of coordinate system. Here, we calculated both $\boldsymbol{v}_y$ and the *y-dir* integral term of (A.5) in Cartesian and cylindrical coordinate systems.

Cartesian CS: in this system $\boldsymbol{v}_y = \left(\frac{\partial x'}{\partial y}, \frac{\partial z'}{\partial y}\right)$, and according to the convention for $\hat{\boldsymbol{n}}$ and the direction

of traversing the curvature, in a right-handed coordinate system, we have $\hat{\boldsymbol{n}}\ dl = (dz', -dx')$. Therefore

$$\oint_{B_{int}} \phi\ \boldsymbol{v}_y \cdot \hat{\boldsymbol{n}}\ dl = \oint_{B_{int}} \phi\ \frac{\partial x'}{\partial y}\ dz' - \oint_{B_{int}} \phi\ \frac{\partial z'}{\partial y}\ dx'. \tag{A.8}$$

Cylindrical CS: in this system, a point on the boundary of manifold can be represented by $\boldsymbol{x}|_b = \boldsymbol{r} = r\hat{\boldsymbol{r}}$; and $\hat{\boldsymbol{n}}\ dl = -\hat{\boldsymbol{r}}\ rd\theta + \hat{\boldsymbol{\theta}}\ dr$, thus

$$\boldsymbol{v}_y = \frac{\partial(r\hat{\boldsymbol{r}})}{\partial y} = \left(\frac{\partial r}{\partial y}\hat{\boldsymbol{r}} + r\frac{\partial \hat{\boldsymbol{r}}}{\partial y}\right) = \left(\frac{\partial r}{\partial y}\hat{\boldsymbol{r}} + r\frac{\partial \theta}{\partial y}\hat{\boldsymbol{\theta}}\right), \tag{A.9}$$

$$\oint_{B_{int}} \phi\ \boldsymbol{v}_y \cdot \hat{\boldsymbol{n}}\ dl = \oint_{B_{int}} \phi\ r\ \frac{\partial \theta}{\partial y}\ dr - \oint_{B_{int}} \phi\ r\ \frac{\partial r}{\partial y}\ d\theta. \tag{A.10}$$

A.2.3 General form of continuity and FANS equations

Implementing Area-Filtering to the Reynolds-Averaged continuity equation, one obtains the continuity equation in the following form

$$\frac{\partial \langle \overline{U}_j \rangle}{\partial x_j} = -\frac{\langle \overline{U}_j \rangle}{A}\frac{\partial A}{\partial x_j} + \frac{1}{A}\oint_{B_{int}} \overline{U}_j\ \boldsymbol{v}_j \cdot \hat{\boldsymbol{n}}\ dl. \tag{A.11}$$

Starting with RANS equations, one can obtain the general form of FANS equations as follows

$$
\begin{aligned}
\frac{\partial\langle\overline{U}_i\rangle}{\partial t}+\frac{\partial\langle\overline{U}_i\rangle\langle\overline{U}_j\rangle}{\partial x_j} = & -\frac{1}{\rho}\frac{\partial\langle\overline{P}\rangle}{\partial x_i}+\nu\frac{\partial^2\langle\overline{U}_i\rangle}{\partial x_j\partial x_j}+\langle g_i\rangle \\
& -\frac{\partial\langle\overline{u_i'u_j'}\rangle}{\partial x_j}-\frac{\partial R_{ij}}{\partial x_j} \\
& \left.\begin{aligned}
& -\frac{\langle\overline{U}_i\rangle}{A}\frac{\partial A}{\partial t}-\frac{\langle\overline{P}\rangle}{A\rho}\frac{\partial A}{\partial x_i} \\
& +\left(-\langle\overline{U}_i\rangle\langle\overline{U}_j\rangle-\langle\overline{u_i'u_j'}\rangle-R_{ij}+\nu\frac{\partial\langle\overline{U}_i\rangle}{\partial x_j}\right)\frac{1}{A}\frac{\partial A}{\partial x_j} \\
& +\nu\frac{\partial\langle\overline{U}_i\rangle}{\partial x_j}\frac{1}{A}\frac{\partial A}{\partial x_j}+\nu\langle\overline{U}_i\rangle\frac{1}{A}\frac{\partial^2 A}{\partial x_j\partial x_j}
\end{aligned}\right\}\zeta_i \\
& \left.\begin{aligned}
& -\frac{\nu}{A}\oint_{B_{int}}\frac{\partial\overline{U}_i}{\partial x_j}\boldsymbol{v}_j\cdot\hat{\boldsymbol{n}}\,dl+\frac{1}{A\rho}\oint_{B_{int}}\overline{P}\,\boldsymbol{v}_i\cdot\hat{\boldsymbol{n}}\,dl \\
& +\frac{1}{A}\oint_{B_{int}}\overline{U}_i\,\boldsymbol{v}_t\cdot\hat{\boldsymbol{n}}\,dl+\frac{1}{A}\oint_{B_{int}}\overline{U}_i\overline{U}_j\,\boldsymbol{v}_j\cdot\hat{\boldsymbol{n}}\,dl \\
& -\frac{\nu}{A}\frac{\partial(\oint_{B_{int}}\overline{U}_i\,\boldsymbol{v}_j\cdot\hat{\boldsymbol{n}}\,dl)}{\partial x_j}+\frac{1}{A}\oint_{B_{int}}\overline{u_i'u_j'}\,\boldsymbol{v}_j\cdot\hat{\boldsymbol{n}}\,dl
\end{aligned}\right\}\Im_i,
\end{aligned}
\tag{A.12}
$$

where $R_{ij}\equiv\langle\overline{U}_i\overline{U}_j\rangle-\langle\overline{U}_i\rangle\langle\overline{U}_j\rangle$ is the dispersive stress term.

Equation (A.12) is the most general form of the Ensemble-Averaged, Area-Filtered Incompressible Navier Stokes equations which can be implemented to study a wide range of fluids physics including, but not restricted to: immiscible multi-phase multi-components fluids (by writing the equation for each phase and regarding integral terms as coupling agents between phases), meteorological, atmospheric and species flows (in which flow field is affected by species field), flow in porous media, and flow over canopies or rough surfaces. The equations can be used to study mixtures of these flows as well (*e.g.* multiphase flow over rough surfaces). In this sense, the procedure presented here unifies all aforementioned studies. We will elaborate on flow over roughness in subsequent sections.

All terms in the first line of (A.12) are closed, but the second line contains well known Reynolds and dispersive stresses, which are to be modeled.

The important, but unstudied terms in (A.12) are ζ_i and $\Im_i$. Similar terms exist in mass conservation equation (see A.11) as well. ζ_i represents the effect of area distribution, in all

directions, on the flow field. This term is a conservation of momentum (or mass in A.11) due to area change .The term 'conservation' was chosen because ζ is due to area change and not due to an explicit external force. If the area distribution is known, which is the case in study of flow over most rough surfaces, ζ_i is closed and it does not need any more modifications. If the area distribution is unknown (such as in multi phase flows), then the determination of ζ_i will depend upon the modeling of area gradients. In the study of fluid physics that have some sort of interaction with solid materials, like flow over roughness and canopies or flow in porous media, ζ_i is an explicit effect of the geometry of the solid on flow dynamics, and it introduces fluid area distribution, or interchangeably, solid area distribution, as a primary means by which the solid affects the fluid dynamics.

$\Im_i$ in (A.12) is the balance of momentum (or mass in A.11) due to interaction with other phases, or solid parts. This term represents different processes in which one phase interacts with others, among which the pressure and viscous drag terms (first line in $\Im_i$) are the best known ones. The term $-\nu\frac{\partial(\oint_{B_{int}} \overline{U}_i \, \boldsymbol{v}_j \cdot \hat{\boldsymbol{n}} \, dl)}{\partial x_j}$ is a viscous effect due to the gradient of the bulk expansion-contraction of the boundaries.

A.2.4 FANS equations for fully-developed channel flows

For fully-developed channel flows over rough walls, one notices $\langle \overline{v} \rangle_s = \langle \overline{w} \rangle_s = 0$ and $\frac{\partial \langle \overline{u} \rangle_s}{\partial x} = \frac{\partial \langle \overline{u} \rangle_s}{\partial z} = 0$. Assuming homogeneous roughness $\left(\frac{\partial A_r}{\partial x} = \frac{\partial A_r}{\partial z} = 0\right)$, then the streamwise FANS equation reduces to

$$-\frac{d\langle \overline{P} \rangle_s}{dx} - \frac{\partial \langle \overline{u'v'} \rangle_s}{\partial y} - \frac{\partial \langle \overline{\tilde{u}\tilde{v}} \rangle_s}{\partial y} + \nu \frac{\partial^2 \langle \overline{u} \rangle_s}{\partial y^2} + f_v + f_p = 0, \tag{A.13}$$

where,

$$\begin{aligned} f_v &= -\frac{\nu}{A_t} \oint_{B_{int}} \frac{\partial \overline{U}_1}{\partial x_j} \boldsymbol{v}_j \cdot \hat{\boldsymbol{n}} \, dl \\ f_p &= \frac{1}{A_t} \oint_{B_{int}} \overline{P} \, \boldsymbol{v}_1 \cdot \hat{\boldsymbol{n}} \, dl, \end{aligned} \tag{A.14}$$

are the form viscous and pressure drag terms, respectively. Equation A.13 is the streamwise DANS equation for fully-developed channel flows over homogeneous rough walls.

APPENDIX B

CORRECTION OF NEUMANN BOUNDARY CONDITION USING LEVEL-SET METHOD

Direct forcing approaches are devised for Dirichlet's boundary condition, and they posed some issues with implementation of Neumann's boundary condition, which are mostly because the source term in right-hand-side of NS equations cannot be defined simply to satisfy Neumann's BC in this method. This problem can be treated by using a level-set function and introducing another correction step in the solver, which corrects the boundary values to account for fluxes at the boundary, such that

$$\frac{\partial P}{\partial n} = \nabla P \cdot \frac{\nabla \phi}{|\nabla \phi|} = -q$$

where P is a general field parameter, n is the normal direction (positive into fluid), ϕ is the level-set function (0 in the solid, 1 in the fluid), and q is the flux of P at the boundary.

Numerically, one needs to use one-sided discretization (use data from fluid cells only) for ∇P, in order to cut the connection of solid and fluid zones, this can be achieved simply by using the direction of $\nabla \phi$. For example, in a 2D flow, in the locations where $\phi_x < 0,\ \phi_y > 0$, the correction

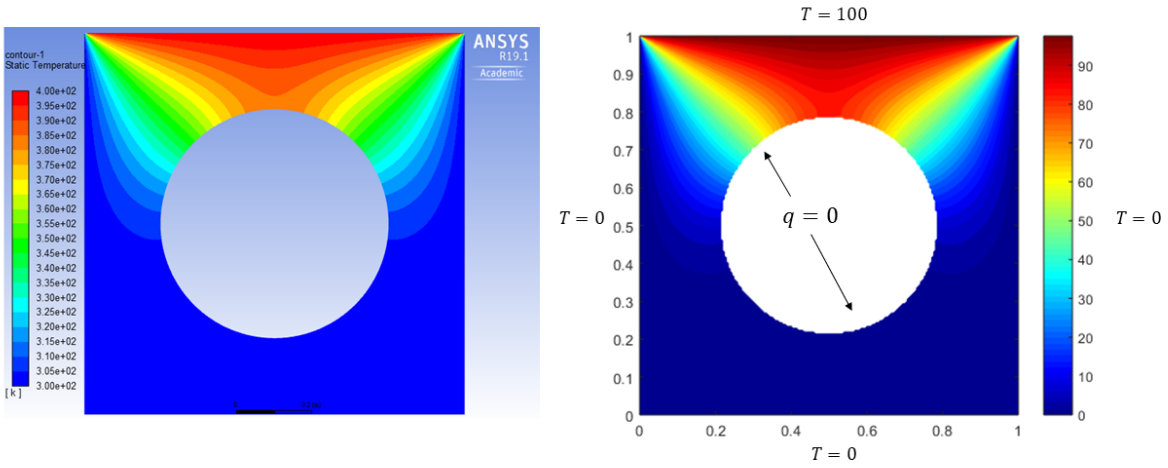

Figure B.1: 2D heat equation solution, using body-conformal mesh *(left)*, and Cartesian mesh (IB method with Neumann BC correction, *right*).

step will reduce to

$$P_{ij} = \frac{-(\phi_{i+1,j} - \phi_{i-1,j})P_{i-1,j} + \alpha^2(\phi_{i,j+1} - \phi_{i,j-1})P_{i,j+1}}{-(\phi_{i+1,j} - \phi_{i-1,j}) + \alpha^2(\phi_{i,j+1} - \phi_{i,j-1})} \tag{B.1}$$

where $\alpha = \frac{\Delta x}{\Delta y}$. Please note use of backward discretization for P_x, and forward discretization for P_y.

Figure B.1 compares the solution of a heat equation $\Delta T = 0$ (with Dritchet's BC for the external boundaries and Neumann's BC for the internal boundary) obtained by this method, with the solution of the same problem obtained by a body-conformal mesh in Fluent software. As one notices, Neumann's BC is satisfied properly using the IB method.

The discretization used in equation B.1 is first-order accurate. Extending this approach to high-order (one-sided) differentiation schemes is straightforward.

BIBLIOGRAPHY

BIBLIOGRAPHY

[1] L. Rempel. Rotor blade leading edge erosion - real life experiences. *Wind Systems Magazine*, pages 22–24, 2012.

[2] L.F. Moody. Friction factors for pipe flow. *ASME Trans.*, 66:671 – 684, 1944.

[3] M. P. Schultz and K. A. Flack. Reynolds-number scaling of turbulent channel flow. *Phys. Fluids*, 25:025104–1–13, 2013.

[4] S. G. Saddoughi and S. V. Veeravalli. Local isotropy in turbulent boundary layers at high Reynolds numbers. *J. Fluid Mech.*, 268:333–372, 1994.

[5] J. Yuan and U. Piomelli. Estimation and prediction of the roughness function on realistic surfaces. *J. Turbul.*, 15:350–365, 2014.

[6] M. Aghaei Jouybari, G. J. Brereton, and J. Yuan. Turbulence structures over realistic and synthetic wall roughness in open channel flow at $\mathrm{Re}_\tau = 1000$. *J. Turbul.*, 20:723–749, December 2019.

[7] G. N. Coleman, J. Kim, and R. D. Moser. A numerical study of turbulent supersonic isothermal-wall channel flow. *J. Fluid Mech.*, 305:159–183, 1995.

[8] G. S. Williams and A. Hazen. *Hydraulic tables; the elements of gagings and the friction of water flowing in pipes, aqueducts, sewers, etc. as determined by the Hazen and Williams formula and the flow of water over sharp-edged and irregular weirs, and the quantity discharged, as determined by Bazin's formula and experimental investigations upon large models*. J. Wiley & sons, New York, 1909.

[9] F. Farshad, H. Rieke, and J. Garber. New developments in surface roughness measurements, characterization, and modeling fluid flow in pipe. *J. Pet. Sci. Eng.*, 29(2):139 – 150, 2001.

[10] F. Canovaro, E. Paris, and L. Solari. Effects of macro-scale bed roughness geometry on flow resistance. *Water Resour. Res.*, 43(10), 2007.

[11] K. S. Cunningham and A. I. Gotlieb. The role of shear stress in the pathogenesis of atherosclerosis. *Lab. Investig.*, 85:9–23, 2005.

[12] F. M. White. *Fluid Mechanics*. McGraw-Hill, New York, 7th ed edition, 2010.

[13] J. Jiménez. Turbulent flows over rough walls. *Annu. Rev. Fluid Mech.*, 36:173–196, 2004.

[14] M. R. Raupach, R. A. Antonia, and S. Rajagopalan. Rough-wall boundary layers. *Appl. Mech. Rev.*, 44:1–25, 1991.

[15] S. K. Robinson. Coherent motions in the turbulent boundary layer. *Annu. Rev. Fluid Mech.*, 23:601–639, 1991.

[16] O. Coceal, A. Dobre, T. G. Thomas, and S. E. Belcher. Structure of turbulent flow over regular arrays of cubical roughness. *J. Fluid Mech.*, 589:375–409, 2007.

[17] R. J. Volino, M. P. Schultz, and K. A. Flack. Turbulence structure in boundary layers over periodic two- and three-dimensional roughness. *J. Fluid Mech.*, 676:172–190, 2011.

[18] S. Talapatra and J. Katz. Coherent structures in the inner part of a rough-wall channel flow resolved using holographic piv. *J. Fluid Mech.*, 711:161–170, 2012.

[19] L. Chan, M. MacDonald, D. Chung, N. Hutchins, and A. Ooi. Secondary motion in turbulent pipe flow with three-dimensional roughness. *J. Fluid Mech.*, 854:5–33, 2018.

[20] M. R. Raupach and A. S. Thom. Turbulence in and above plant canopies. *Annu. Rev. Fluid Mech.*, 13:97–129, 1981.

[21] A. Christen, E. van Gorsel, and R. Vogt. Coherent structures in urban roughness sublayer turbulence. *Int. J. Climatol.*, 27:1955–1968, 2007.

[22] S. C. Kassinos, W. C. Reynolds, and M. M. Rogers. One-point turbulence structure tensors. *J. Fluid Mech.*, 428:213–248, 2001.

[23] J. Yuan, G. J. Brereton, G. Iaccarino, A. A. Mishra, and M. Vartdal. Single-point structure tensors in rough-wall turbulent channel flow. In *Proceedings of the 2018 Summer Program*, 2018.

[24] C. Klipp. Wind direction dependence of atmospheric boundary layer turbulence parameters in the urban roughness sublayer. *J. Appl. Meteorol. Climatol.*, 46:2086–2097, 2007.

[25] Schumann U. and Schmidt H. Heat transfer by thermals in the convective boundary layer. *Advances in Turbulence 2*, 1989.

[26] A. Serafimovich, C. Thomas, and T. Foken. Vertical and horizontal transport of energy and matter by coherent motions in a tall spruce canopy. *Bound.-Lay. Meteorol.*, 140(3):429–448, 2011.

[27] Y.Z. Zhang, C. Sun, Y. Bao, and Q. Zhou. How surface roughness reduces heat transport for small roughness heights in turbulent Rayleigh–Bénard convection. *J. Fluid Mech.*, 836:R2, 2018.

[28] J. Yuan and U. Piomelli. Numerical simulation of a spatially developing accelerating boundary layer over roughness. *J. Fluid Mech.*, 780:192–214, 2015.

[29] P.R. Spalart. Numerical study of sink-flow boundary layers. *J. Fluid Mech.*, 172:307–328, 1986.

[30] R. Narasimha and K. R. Sreenivasan. Relaminarization in highly accelerated turbulent boundary layers. *J. Fluid Mech.*, 61:417–447, 1973.

[31] H. W. Coleman, R. J. Moffat, and W. M. Kays. The accelerated fully rough turbulent boundary layer. *J. Fluid Mech.*, 82:507–528, 1977.

[32] S. P. Schneider. Effects of roughness on hypersonic boundary-layer transition. *J. Spacecr. Rockets*, 45:193–209, 2008.

[33] B.D. Kocher, C.S. Combs, P.A. Kreth, J.D. Schmisseur, and S.J. Peltier. *Investigation of the Effects of Distributed Surface Roughness on Supersonic Flows*. 2017.

[34] P. A. Durbin. Near-wall turbulence closure modeling without damping functions. *Theor. Comput. Fluid Dyn.*, 3:1–13, 1991.

[35] J. Nikuradse. Strömungsgesetze in rauhen rohren. *VDI-Forsch.*, 1933.

[36] K. A. Flack. Moving beyond Moody. *J. Fluid Mech.*, 842:1–4, 2018.

[37] E. Napoli, V. Armenio, and M. De Marchis. The effect of the slope of irregularly distributed roughness elements on turbulent wall-bounded flows. *J. Fluid Mech.*, 613:385–394, 2008.

[38] K. A. Flack and M. P. Schultz. Review of hydraulic roughness scales in the fully rough regime. *J. Fluids Eng.*, 132:041203–1—10, 2010.

[39] M. R. Raupach and R. H. Shaw. Averaging procedures for flow within vegetation canopies. *Bound.-Lay. Meteorol.*, 22:79–90, 1982.

[40] F. A. Howes and S. Whitaker. The spatial averaging theorem revisited. *Chem. Eng. Sci.*, 40:1387–1392, 1985.

[41] V. Nikora, I. McEwan, S. McLean, S. Coleman, D. Pokrajac, and R. Walters. Double-averaging concept for rough-bed open-channel and overland flows: theoretical background. *J. Hydr. Eng.*, 133:873–883, 2007.

[42] J. Finnigan. Turbulence in plant canopies. *Annu. Rev. Fluid Mech.*, 32:519–571, 2000.

[43] E. Mignot, E. Barthelemy, and D. Hurther. Double-averaging analysis and local flow characterization of near-bed turbulence in gravel-bed channel flows. *J. Fluid Mech.*, 618:279–303, 2009.

[44] J. Yuan and U. Piomelli. Roughness effects on the Reynolds stress budgets in near-wall turbulence. *J. Fluid Mech.*, 760:R1, 2014.

[45] A. Busse and T. O. Jelly. Influence of surface anisotropy on turbulent flow over irregular roughness. *Flow Turbul. Combust.*, pages 331–354, 2020.

[46] M. G. Giometto, A. Christen, C. Meneveau, J. Fang, M. Krafczyk, and M. B. Parlange. Spatial characteristics of roughness sublayer mean flow and turbulence over a realistic urban surface. *Bound.-Lay. Meteorol.*, pages 1–28, 2016.

[47] K. Suga, T. J. Craft, and H. Iacovides. An analytical wall-function for turbulent flows and heat transfer over rough walls. *Int. J. Heat Fluid Fl.*, 27:852–866, 2006.

[48] J. Nikuradse. Laws of flow in rough pipes. *NACA Technical Memorandum 1292*, 1933.

[49] C.H. Lee. Rough boundary treatment method for the shear-stress transport k - ω model. *Eng. Appl. Comput. Fluid Mech.*, 12:261–269, 2018.

[50] M. Samiee, A. Akhavan-Safaei, and M. Zayernouri. A fractional subgrid-scale model for turbulent flows: Theoretical formulation and a priori study. *Phys. Fluids*, 32(5):055102, 2020.

[51] J. George, A. De Simone, G. Iaccarino, and J. Jimenez. Modeling roughness effects in turbulent boundary layers by elliptic relaxation. In *Proc. Summer Program, Center for Turbulence Research*, pages 119–128, 2010.

[52] J. Yuan and U. Piomelli. Numerical simulations of sink-flow boundary layers over rough surfaces. *Phys. Fluids*, 26:015113–1—015113–28, 2014.

[53] A. Keating. *Large-eddy simulation of heat transfer in turbulent channel flow and in the turbulent flow downstream of a backward-facing step*. PhD thesis, University of Queensland, 2004.

[54] A. Scotti. Direct numerical simulation of turbulent channel flows with boundary roughened with virtual sandpaper. *Phys. Fluids*, 18:031701–1—4, 2006.

[55] S. Leonardi, P. Orlandi, and R. A. Antonia. Properties of d- and k-type roughness in a turbulent channel flow. *Phys. Fluids*, 19(12):125101, 2007.

[56] E. Napoli, V. Armenio, and V. De Marchis. The effect of the slope of irregularly distributed roughness elements on turbulent wall-bounded flows. *J. Fluid Mech.*, 613:385–394, 2008.

[57] J. Yuan and M. Aghaei Jouybari. Topographical effects of roughness on turbulence statistics in roughness sublayer. *Phys. Rev. Fluids*, 3:114603–19, 2018.

[58] A. Majumdar and B. Bhushan. Role of fractal geometry in roughness characterization and contact mechanics of surfaces. *J. Tribol.*, 112(2):205–216, 1990.

[59] P. R. Bandyopadhyay. Rough-wall turbulent boundary layers in the transition regime. *J. Fluid Mech.*, 180:231–266, 1987.

[60] R. D. Moser and P. Moin. The effects of curvature in wall-bounded turbulent flows. *J. Fluid Mech.*, 175:479–510, 1987.

[61] D. Pokrajac, L. J. Campbell, V. Nikora, C. Manes, and I. McEwan. Quadrant analysis of persistent spatial velocity perturbations over square-bar roughness. *Exp. Fluids*, 42:413–423, 2007.

[62] P. S. Jackson. On the displacement height in the logarithmic velocity profile. *J. Fluid Mech.*, 111:15–25, 1981.

[63] R. Mejia-Alvarez and K. T. Christensen. Low-order representations of irregular surface roughness and their impact on a turbulent boundary layer. *Phys. Fluids*, 22:015106–1–20, 2010.

[64] J. M. Barros and K. T. Christensen. Observations of turbulent secondary flows in a rough-wall boundary layer. *J. Fluid Mech.*, 748:R1, 2014.

[65] C. Vanderwel and B. Ganapathisubramani. Effects of spanwise spacing on large-scale secondary flows in rough-wall turbulent boundary layers. *J. Fluid Mech.*, 774:R2, 2015.

[66] J. Yang and W. Anderson. Numerical study of turbulent channel flow over surfaces with variable spanwise heterogeneities: Topographically-driven secondary flows affect outer-layer similarity of turbulent length scales. *Flow Turb. Combust.*, 100:1–17, 2018.

[67] W. Munters, C. Meneveau, and J. Meyers. Shifted periodic boundary conditions for simulations of wall-bounded turbulent flows. *Phys. Fluids*, 28:025112, 2016.

[68] N. N. Mansour, J. Kim, and P. Moin. Reynolds-stress and dissipation-rate budgets in a turbulent channel flow. *J. Fluid Mech.*, 194:15–44, 1988.

[69] A. A. Townsend. *The structure of turbulent shear flow*. Cambridge University Press, 1976.

[70] R. J. Adrian. On the role of conditional averages in turbulence theory. *Turbul. Liquids*, pages 323–332, 1975.

[71] J. Jeong, F. Hussain, W. Schoppa, and J. Kim. Coherent structures near the wall in a turbulent channel flow. *J. Fluid Mech.*, 332:185–214, 1997.

[72] J. Zhou, R. J. Adrian, S. Balachandar, and T. M. Kendall. Mechanisms for generating coherent packets of hairpin vortices in channel flow. *J. Fluid Mech.*, 387:353–396, 1999.

[73] A. Lozano-Durán and J. Jiménez. Time-resolved evolution of coherent structures in turbulent channels: characterization of eddies and cascades. *J. Fluid Mech.*, 759:432–471, 2014.

[74] X. Wu, P. Moin, J. M. Wallace, J. Skarda, A. Lozano-Duran, and J.-P. Hickey. Transitional–turbulent spots and turbulent–turbulent spots in boundary layers. *Proc. Natl. Acad. Sci. USA*, pages E5292–E5299, 2017.

[75] S. Tardu. *Transport and Coherent Structures in Wall Turbulence*. Wiley & Sons, Inc., 2014.

[76] Y. Wu and K.T. Christensen. Spatial structure of a turbulent boundary layer with irregular surface roughness. *J. Fluid Mech.*, 655:380–418, 2010.

[77] P.-Å. Krogstad and R. A. Antonia. Surface roughness effects in turbulent boundary layers. *Exp. Fluids*, 27:450–460, 1999.

[78] P. Passalacqua, F. Porté-Agel, E. Foufoula-Georgiou, and C. Paola. Application of dynamic subgrid-scale concepts from large-eddy simulation to modeling landscape evolution. *Water Resour. Res.*, 42:W06D11–1–11, 2006.

[79] P. Orlandi, S. Leonardi, and R. A. Antonia. Turbulent channel flow with either transverse or longitudinal roughness elements on one wall. *J. Fluid Mech.*, 561:279–305, 2006.

[80] P. Forooghi, A. Stroh, P. Schlatter, and B. Frohnapfel. Direct numerical simulation of flow over dissimilar, randomly distributed roughness elements: A systematic study on the effect of surface morphology on turbulence. *Phys. Rev. Fluids*, 3:044605, 2018.

[81] J. M. Barros, M. P. Schultz, and K. A. Flack. Measurements of skin-friction of systematically generated surface roughness. *Int. J. Heat Fluid Flow*, 72:1 – 7, 2018.

[82] A. Busse, M. Lützner, and N. D. Sandham. Direct numerical simulation of turbulent flow over a rough surface based on a surface scan. *Comput. Fluids*, 116:129–147, 2015.

[83] S. Leonardi, P. Orlandi, L. Djenidi, and R. A. Antonia. Structure of turbulent channel flow with square bars on one wall. *Int. J. Heat Fluid Flow*, 25:384–32, 2004.

[84] P.-Å. Krogstad and R. A. Antonia. Structure of turbulent boundary layers on smooth and rough walls. *J. Fluid Mech.*, 277:1–21, 1994.

[85] K. T. Christensen and Y. Wu. Characteristics of vortex organization in the outer layer of wall turbulence. In *Proc. Fourth Int. Symp. on Turbulence and Shear Flow Phenomena*, volume 3, pages 1025–1030, Williamsburg, Virginia, 2005.

[86] J. Sabot, I. Saleh, and G. Comte-Bellot. Effects of roughness on the intermittent maintenance of Reynolds shear stress in pipe flow. *Phys. Fluids*, 20:S150–S155, 1977.

[87] C. D. Tomkins and R. J. Adrian. Spanwise structure and scale growth in turbulent boundary layers. *J. Fluid Mech.*, 490:37–74, 2003.

[88] J. C. del Álamo, J. Jiménez, P. Zandonade, and R. D. Moser. Scaling of the energy spectra of turbulent channels. *J. Fluid Mech.*, 500:135 – 144, 2004.

[89] S. Hoyas and J. Jiménez. Reynolds number effects on the Reynolds-stress budgets in turbulent channels. *Phys. Fluids*, 20:101511–1–9, 2008.

[90] P.-Å Krogstad and V. Efros. About turbulence statistics in the outer part of a boundary layer developing over two- dimensional surface roughness. *Phys. Fluids*, 24:075112–1—15, 2012.

[91] A. N. Kolmogorov. The local structure of turbulence in incompressible viscous fluid for very large Reynolds number. *Dokl. Akad. Nauk. SSSR*, 30:299–303, 1941.

[92] B. Ganapathisubramani, N. Hutchins, W. T. Hambleton, E. K. Longmire, and I. Marusic. Investigation of large-scale coherence in a turbulent boundary layer using two-point correlations. *J. Fluid Mech.*, 524:57–80, 2005.

[93] J. Jiménez, S. Hoyas, M. P. Simens, and Y. Mizuno. Turbulent boundary layers and channels at moderate Reynolds numbers. *J. Fluid Mech.*, 657:335–360, 2010.

[94] S. B. Pope. *Turbulent Flows*. Cambridge Univ. Press, Cambridge, U.K., 2000.

[95] R. D. Moser, J. Kim, and N. N. Mansour. Direct numerical simulation of turbulent channel flow up to $Re_\tau = 590$. *Phys. Fluids*, 11(4):943–945, 1999.

[96] K. Bhaganagar, J. Kim, and G. Coleman. Effect of roughness on wall-bounded turbulence. *Flow Turbul. Combust.*, 72:463–492, 2004.

[97] S. C. Kassinos. *A structure-based model for the rapid distortion of homogeneous turbulence*. PhD thesis, Stanford University, 1995.

[98] R. J. Adrian. Hairpin vortex organization in wall turbulence. *Phys. Fluids*, 19:041301, 2007.

[99] J. Hong, J. Katz, and M. P. Schultz. Near-wall turbulence statistics and flow structures over three-dimensional roughness in a turbulent channel flow. *J. Fluid Mech.*, 667:1–37, 2011.

[100] R. J. Adrian. *Stochastic Estimation of the Structure of Turbulent Fields*, pages 145–195. Springer Vienna, Vienna, 1996.

[101] M. Manhart. Vortex shedding from a hemisphere in a turbulent boundary layer. *Theor. Comput. Fluid Dyn.*, 12:1–28, 1998.

[102] W. Schoppa and F. Hussain. Coherent structure generation in near-wall turbulence. *J. Fluid Mech.*, 453:57–108, 2002.

[103] W. Anderson, J. M. Barros, K. T. Christensen, and A. Awasthi. Numerical and experimental study of mechanisms responsible for turbulent secondary flows in boundary layer flows over spanwise heterogeneous roughness. *J. Fluid Mech.*, 768:316–347, 2015.

[104] J. P. Bons. St and c_f augmentation for real turbine roughness with elevated freestream turbulence. *J. Turbomach.*, 124:632–644, 2002.

[105] J. P. Bons, R. P. Taylor, S. T. McClain, and R. B. Rivir. The many faces of turbine surface roughness. *J. Turbomach.*, 123:739–748, 2001.

[106] J. A. van Rij, B. J. Belnap, and P. M. Ligrani. Analysis and experiments on three-dimensional, irregular surface roughness. *J. Fluids Eng.*, 124:671–677, 2002.

[107] M.P. Schultz and K.A. Flack. Turbulent boundary layers on a systematically varied rough wall. *Phys. Fluids*, 21:015104–1—9, 2009.

[108] M. Thakkar, A. Busse, and N. D. Sandham. Surface correlations of hydrodynamic drag for transitionally rough engineering surfaces. *J. Turbul.*, 18:138–169, 2017.

[109] K. A. Flack, M. P. Schultz, and J. M. Barros. Skin friction measurements of systematically-varied roughness: Probing the role of roughness amplitude and skewness. *Flow Turbul. Combust.*, pages 1–13, 2019.

[110] L. Chan, M. MacDonald, D. Chung, N. Hutchins, and A. Ooi. A systematic investigation of roughness height and wavelength in turbulent pipe flow in the transitionally rough regime. *J. Fluid Mech.*, 771:743–777, 2015.

[111] C.E. Rasmussen and C.K.I. Williams. *Gaussian processes for Machine Learning*. MIT Press, Cambridge, MA, 2006.

[112] Y. LeCun, Y. Bengio, and G. Hinton. Deep learning. *Nature*, 521(7553):436, 2015.

[113] K. A. Flack, M. P. Schultz, J. M. Barros, and Y. C. Kim. Skin-friction behavior in the transitionally-rough regime. *Int. J. Heat Fluid Flow*, 61:21–30, 2016.

[114] J. M. Barros, M. P. Schultz, and K. A. Flack. Measurements of skin-friction of systematically generated surface roughness. *Int. J. Heat Fluid Flow*, 72:1–7, 2018.

[115] P. Forooghi, A. Stroh, F. Magagnato, S. Jakirlic, and B. Frohnapfel. Toward a universal roughness correlation. *J. Fluids Eng.*, 139:121201–1–12, 2017.

[116] P. Moin and K. Mahesh. Direct numerical simulation: a tool in turbulence research. *Annu. Rev. Fluid Mech.*, 30:539–578, 1998.

[117] J. Kim, P. Moin, and R. D. Moser. Turbulence statistics in fully developed channel flow at low Reynolds number. *J. Fluid Mech.*, 177:133–166, 1987.

[118] P. R. Spalart. Direct simulation of a turbulent boundary layer up to $R_\theta = 1410$. *J. Fluid Mech.*, 187:61–98, 1988.

[119] H. Choi and P. Moin. Effects of the computational time step on numerical solutions of turbulent flow. *J. Comput. Phys.*, 113:1–4, 1994.

[120] J. Jimenez and P. Moin. The minimal flow unit in near-wall turbulence. *J. Fluid Mech.*, 225:213–240, 1991.

[121] D. Chung, L. Chan, M. MacDonald, N. Hutchins, and A. Ooi. A fast direct numerical simulation method for characterising hydraulic roughness. *J. Fluid Mech.*, 773:418–431, 2015.

[122] M. MacDonald, D. Chung, N. Hutchins, L. Chan, A. Ooi, and R. García-Mayoral. The minimal-span channel for rough-wall turbulent flows. *J. Fluid Mech.*, 816:5–42, 2017.

[123] R. J. Volino, M. P. Schultz, and K. A. Flack. Turbulence structure in a boundary layer with two-dimensional roughness. *J. Fluid Mech.*, 635:75–101, 2009.

[124] R. Storn and K. Price. Differential evolution – a simple and efficient heuristic for global optimization over continuous spaces. *J. Glob. Optim.*, 11(4):341–359, 1997.

[125] D. C. Reda. Review and synthesis of roughness-dominated transition correlations for reentry applications. *J. Spacecr. Rockets*, 39:161–167, 2002.

[126] R. H. Radeztsky, M. S. Reibert, and W. S. Saric. Effect of isolated micron-sized roughness on transition in swept-wing flows. *AIAA Journal*, 37:1370 – 1377, 1999.

[127] R. M. Latin. *The Influence of Surface Roughness on Supersonic High Reynolds Number Turbulent Boundary Layer Flow*. PhD thesis, School of Engineering of the Air Force Institute of Technology Air University, 1998.

[128] A. L. Braslow and E. C. Knox. Simplified method for determination of critical height of distributed roughness particles for boundary-layer transition at Mach numbers from 0 to 5. Technical report, National Advisory Committee for Aeronautics, 1958.

[129] E. Reshotko and A. Tumin. Role of transient growth in roughness-induced transition. *AIAA Journal*, 42:766 – 770, 2004.

[130] Y. Ji, K. Yuan, and J. N. Chung. Numerical simulation of wall roughness on gaseous flow and heat transfer in a microchannel. *Int. J. Heat Mass Transf.*, 49(7):1329 – 1339, 2006.

[131] D. C. Reda, M. C. Wilder, D. W. Bogdanoff, and D. K. Prabhu. Transition experiments on blunt bodies with distributed roughness in hypersonic free flight. *J. Spacecr. Rockets*, 45:210 – 215, 2008.

[132] M. Bernardini, S. Pirozzoli, and Orlandi. P. Compressibility effects on roughness-induced boundary layer transition. *Int. J. Heat Fluid Flow*, 35:45 – 51, 2012.

[133] C.J. Tyson and N.D. Sandham. Numerical simulation of fully-developed compressible flows over wavy surfaces. *Int. J. Heat Fluid Flow*, 41:2 – 15, 2013.

[134] I. Marusic, B. J. McKeon, P. A. Monkewitz, H. M. Nagib, A. J. Smits, and K. R. Sreenivasan. Wall-bounded turbulent flows at high Reynolds numbers: Recent advances and key issues. *Phys. Fluids*, 22(6):065103, 2010.

[135] R. Mittal and G. Iaccarino. Immersed boundary methods. *Annu. Rev. Fluid Mech.*, 37:239–261, 2005.

[136] Y. Kim and C. S. Peskin. Penalty immersed boundary method for an elastic boundary with mass. *Phys. Fluids*, 19:053103, 2007.

[137] D. Goldstein, R. Handler, and L. Sirovich. Modeling a no-slip flow boundary with an external force field. *J. Comput. Phys.*, 105:354–366, 1993.

[138] E. A. Fadlun, R. Verzicco, P. Orlandi, and J. Mohd-Yusof. Combined immersed-boundary finite-difference methods for three-dimensional complex flow simulations. *J. Comput. Phys.*, 161:35–60, 2000.

[139] Y. H. Tseng and J. H. Ferziger. A ghost-cell immersed boundary method for flow in complex geometry. *J. Comput. Phys.*, 192:593 – 623, 2003.

[140] K. Luo, C. Mao, Z. Zhuang, J. Fan, and N.E.L Haugen. A ghost-cell immersed boundary method for the simulations of heat transfer in compressible flows under different boundary conditions part-ii: Complex geometries. *Int. J. Heat Mass Tran.*, 104:98 – 111, 2017.

[141] R. Ghias, R. Mittal, and H. Dong. A sharp interface immersed boundary method for compressible viscous flows. *J. Comput. Phys.*, 225:528 – 553, 2007.

[142] M. de' Michieli Vitturi, T. Esposti Ongaro, A. Neri, M. V. Salvetti, and F. Beux. An immersed boundary method for compressible multiphase flows: application to the dynamics of pyroclastic density currents. *Comput. Geosci.*, 11:183–198, 2007.

[143] A. Chaudhuri, A. Hadjadj, and A. Chinnayya. On the use of immersed boundary methods for shock/obstacle interactions. *J. Comput. Phys.*, 230(5):1731 – 1748, 2011.

[144] L. Wang, G.M.D. Currao, F. Han, Neely. A. J., J. Young, and F.B. Tian. An immersed boundary method for fluid-structure interaction with compressible multiphase flows. *J. Comput. Phys.*, 346:131 – 151, 2017.

[145] R. Yuan and C. Zhong. An immersed-boundary method for compressible viscous flows and its application in the gas-kinetic BGK scheme. *Appl. Math. Model.*, 55:417 – 446, 2018.

[146] I. W. Ekoto, R. D. W. Bowersox, T. Beutner, and L. P. Goss. Supersonic boundary layers with periodic surface roughness. *AIAA Journal*, 46:486 – 497, 2008.

[147] R. M. Latin and R. D. W. Bowersox. Flow properties of a supersonic turbulent boundary layer with wall roughness. *AIAA Journal*, 38:1804 – 1821, 2000.

[148] R. M. Latin and R. D. W. Bowersox. Temporal turbulent flow structure for supersonic rough-wall boundary layers. *AIAA Journal*, 40:832 – 841, 2002.

[149] S. Muppidi and K. Mahesh. Direct numerical simulations of roughness-induced transition in supersonic boundary layers. *J. Fluid Mech.*, 693:28–56, 2012.

[150] Z. Li and F. A. Jaberi. A high-order finite difference method for numerical simulations of supersonic turbulent flows. *Int. J. Numer. Meth. Fl.*, 68(6):740–766, 2012.

[151] M. Sussman, P. Smereka, and S. Osher. A level set approach for computing solutions to incompressible two-phase flow. *J. Comput. Phys.*, 114(1):146 – 159, 1994.

[152] F. Gibou, R. Fedkiw, and S. Osher. A review of level-set methods and some recent applications. *J. Comput. Phys.*, 353:82 – 109, 2018.

[153] M.A. Vyas, D.A. Yoder, and D.V. Gaitonde. Reynolds-stress budgets in an impinging shock-wave/boundary-layer interaction. *AIAA Journal*, 57(11):4698–4714, 2019.

[154] J. H. Cushman. Multiphase transport equations: I- general equation for macroscopic statistical, local, space-time homogeneity. *Transp. Theory Stat. Phys.*, 12:1:35–71, 1983.

[155] L. Giménez-Curto and A. Corniero Lera. Oscillating turbulent flow over very rough surfaces. *J. Geophys. Res.*, 101:20,745–20,758, 1996.